

Model Analysis of the Hydrologic Response to Climate Change in the Upper Deschutes
Basin, Oregon

by

Michael Scott Waibel

A thesis submitted in partial fulfillment of the
requirements for the degree of

Master of Science
in
Geology: Geohydrology

Thesis Committee:
Christina L. Hulbe, chair
Marshall W. Gannett
Heejun Chang
Kenneth M. Cruikshank

Portland State University
©2011

ABSTRACT

Considerable interest lies in understanding the hydrologic response to climate change in the upper Deschutes Basin, particularly as it relates to groundwater fed streams. Much of the precipitation occurring in the recharge zone falls as snow. Consequently, the timing of runoff and recharge depend on accumulation and melting of the snowpack. Numerical modeling can provide insights into evolving hydrologic system response for resource management consideration.

A daily mass and energy balance model known as the Deep Percolation Model (DPM) was developed for the basin in the 1990s. This model uses spatially distributed data and is driven with daily climate data to calculate both daily and monthly mass and energy balance for the major components of the hydrologic budget across the basin. Previously historical daily climate data from weather stations in the basin was used to drive the model. Now we use the University of Washington Climate Impact Group's 1/16th degree daily downscaled climate data to drive the DPM for forecasting until the end of the 21st century. The downscaled climate data is comprised from the mean of eight GCM simulations well suited to the Pacific Northwest. Furthermore, there are low emission and high emission scenarios associated with each ensemble member leading to two distinct means.

For the entire basin progressing into the 21st century, output from the DPM using both emission scenarios as a forcing show changes in the timing of runoff and

recharge as well as significant reductions in snowpack. Although the DPM calculated amounts of recharge and runoff varies between the emission scenario of the ensemble under consideration, all model output shows loss of the spring snowmelt runoff / recharge peak as time progresses.

The response of the groundwater system to changing in the time and amount of recharge varies spatially. Short flow paths in the upper part of the basin are potentially more sensitive to the change in seasonality. However, geologic controls on the system cause this signal to attenuate as it propagates into the lower portions of the basin. This scale-dependent variation to the response of the groundwater system to changes in seasonality and magnitude of recharge is explored by applying DPM calculated recharge to an existing regional groundwater flow model.

ACKNOWLEDGEMENTS

I would like to thank my thesis advisor, Dr. Christina Hulbe, for guiding me through this endeavor. You are the best! I cannot find adequate words to express my gratitude for your time, energy, and knowledge. I would also like to thank the other members of my committee: Marshall Gannett, Heejun Chang, and Ken Cruikshank. A special thank you to Marshall for your time, patience, and wealth of knowledge concerning the hydrology of the upper Deschutes Basin, this thesis would not have been possible without you. Thank you to Heejun for providing the downscaled GCM data used in this project and for your expertise. Thank you to Ken Cruikshank for answering many questions and providing guidance. Also, a special thank you goes to Ken Lite for showing me some of the more important geologic and hydrologic features of the upper Deschutes Basin.

There have been many people at the USGS Oregon Water Science Center and PSU who have provided me with help and assistance. Foremost among these, I would like to thank Leonard Orzol, whose programming abilities saved the day on more than one occasion. Also, I owe a debt of gratitude to Nancy Eriksson at PSU for helping me navigate the sea of red tape.

I would like to thank my family, especially my mother, for providing me with love and support. Additionally, I would like to thank Erin Temple for being my sounding board and for her patience and understanding throughout this project.

Finally, I would like to thank Leslie Stillwater and the Bureau of Reclamation for making this work possible through a Science and Technology Grant.

TABLE OF CONTENTS

ABSTRACT	i
ACKNOWLEDGEMENTS	iii
LIST OF TABLES	viii
LIST OF FIGURES	x
INTRODUCTION	1
The Problem	2
DESCRIPTION OF THE STUDY AREA	5
Geography	5
Geologic Setting	7
Tectonic Structures	9
Hydrogeologic Units	10
MODEL DESCRIPTIONS	14
Climate System Model Output	14
Bias Correction and Spatial Disaggregation Downscaling	16
Deep Percolation Model	19
Overview	19
Deschutes Basin DPM	22
Model boundaries and domain	22
Spatially Distributed Data	24

Daily Weather Data	27
Regional Groundwater Model	28
Spatial discretization and boundary conditions	29
METHODS	30
Historical Daily Climate Data	30
Deep Percolation Model Updating and Validation.....	34
Downscaled General Circulation Model Climate Data	40
Procedure	42
RESULTS	45
Downscaled GCM Temperature and Precipitation as Interpolated by the DPM	45
Deep Percolation Model	49
Basin-wide Averages	50
Changes in Spatial Distribution of Recharge and Runoff	56
Patterns of Recharge and Runoff in the 1980s	57
21 st Century.....	63
Response of Groundwater Discharge to Projected Future Climate	77
Changes in Groundwater Discharge in the Southern Basin Stream	79
Changes in Groundwater Discharge in the Northern and Central Basin	82
DISCUSSION.....	86
Simulated Response of Groundwater Discharge to Climate Change	86
Model Uncertainty.....	87

CONCLUSIONS	91
REFERENCES	94
APPENDIX A: Temperature Regression Statistics.....	98
APPENDIX B: Centroid Selection.....	101
APPENDIX C: 1980s Historical Record and Ensemble Mean GCM Recharge and Runoff Comparisons for the DPM	103
APPENDIX D: 2020s Spatial Changes.....	104
APPENDIX E: 2050s Spatial Changes	109
APPENDIX F: 2080s Spatial Changes.....	114
APPENDIX G: Groundwater Discharge to Select Stream Reaches.....	119
APPENDIX H: Mean Annual Precipitation Changes	139
APPENDIX I: Mean Annual Recharge Changes	140
APPENDIX J: Mean Annual Runoff Changes.....	141
APPENDIX K: Mean Annual Actual Evapotranspiration Changes.....	142

LIST OF TABLES

Number	Page
Table 1. Names of the GCMs.....	15
Table 2. The four thirty year climate periods.....	16
Table 3. Weather stations used by the DPM	27
Table 4. The mean 1962-2008 period recharge, runoff and sums.....	39
Table 5. Seasons through the year and the included months.....	43
Table 6. Ensemble mean changes in annual average temperature and precipitation. .	46
Table 7. Multiple comparison procedure results for recharge in the A1B scenario....	51
Table 8. Multiple comparison procedure results for recharge in the B1 scenario.....	52
Table 9. Multiple comparison procedure results for runoff in the A1B scenario.....	54
Table 10. Multiple comparison procedure results for runoff in the B1 scenario.....	55
Table 11. Differences in basin-wide averaged recharge and runoff.....	56
Table 12. Summary statistics of DPM spatial recharge changes for the A1B emission scenario in the northern region.	65
Table 13. Summary statistics of DPM spatial recharge changes for the B1 emission scenario in the northern region.	65
Table 14. Summary statistics of DPM spatial runoff changes for the A1B emission scenario in the northern region.	67
Table 15. Summary statistics of DPM spatial runoff changes for the B1 emission scenario in the northern region.	67
Table 16. Summary statistics of DPM spatial recharge changes for the A1B emission scenario in the Three Sisters region.....	69
Table 17. Summary statistics of DPM spatial recharge changes for the B1 emission scenario in the Three Sisters region.....	69

Table 18. Summary statistics of DPM spatial runoff changes for the A1B emission scenario in the Three Sisters region.....	70
Table 19. Summary statistics of DPM spatial runoff changes for the B1 emission scenario in the Three Sisters region.....	70
Table 20. Summary statistics of DPM spatial recharge changes for the A1B emission scenario in the southern region.....	71
Table 21. Summary statistics of DPM spatial recharge changes for the B1 emission scenario in the southern region.....	72
Table 22. Summary statistics of DPM spatial runoff changes for the A1B emission scenario in the southern region.....	73
Table 23. Summary statistics of DPM spatial runoff changes for the B1 emission scenario in the southern region.....	73
Table 24. Summary statistics of DPM spatial recharge changes for the A1B emission scenario in the Newberry region.....	75
Table 25. Summary statistics of DPM spatial recharge changes for the B1 emission scenario in the Newberry region.....	75
Table 26. Summary statistics of DPM spatial runoff changes for the A1B emission scenario in the Newberry region.....	77
Table 27. Summary statistics of DPM spatial recharge changes for the B1 emission scenario in the Newberry region.....	77
Table 28. Odell Creek A1B scenario projected mean monthly groundwater discharge.	82
Table 29. Middle Deschutes River A1B scenario projected mean monthly groundwater discharge.....	85

LIST OF FIGURES

Number	Page
Figure 1. The location of the upper Deschutes Basin in central Oregon.....	6
Figure 2. Generalized geology of the Upper Deschutes Basin.....	8
Figure 3. Hydrogeologic units of the upper Deschutes Basin.	11
Figure 4. Conceptual flow model of the water balance.....	21
Figure 5. DPM grid for the upper Deschutes Basin..	23
Figure 6. The spatial distribution of the ten hydrologic soil types.	25
Figure 7. The spatial distribution of the four land cover types.....	26
Figure 8. Graphical display of model validation results.....	38
Figure 9. Annual mean hydrograph of streamflow, simulated recharge + runoff.	40
Figure 10. Mean annual A1B temperatures averaged basin wide.	45
Figure 11. Mean annual B1 temperatures averaged basin wide.....	46
Figure 12. Cumulative yearly precipitation of all GCMs used in the A1B scenario...	47
Figure 13. Cumulative yearly precipitation of all GCMs used in the B1 scenario.. ...	48
Figure 14. Mean monthly recharge for the A1B scenario averaged basin-wide.	50
Figure 15. Mean monthly recharge for the B1 scenario averaged basin-wide.	51
Figure 16. Mean monthly runoff for the A1B scenario averaged basin-wide.....	53
Figure 17. Mean monthly runoff for the B1 scenario averaged basin-wide.....	54
Figure 18. Regions of interest for spatial distributions of recharge and runoff.....	58
Figure 19. Spatial distribution of mean winter recharge and runoff for the 1980s.	60
Figure 20. Locations of stream reaches investigated for changes in groundwater discharge from projected future climate.....	78
Figure 21. Odel Creek A1B emission scenario groundwater discharge.....	81

Figure 22. Deschutes inflow between Lower Bridge and Culver A1B emission scenario groundwater discharge. 84

Figure 23. Anomaly plots of changes in recharge and runoff from the 1980s..... 92

INTRODUCTION

The upper Deschutes River is a groundwater-dominated stream on the eastern side of the Oregon Cascade Range. Surface water rights in the basin are fully appropriated and there is considerable interest in understanding how changes in groundwater usage may affect surface water resources. The USGS Oregon Water Science Center and Oregon Water Resource Department have developed a groundwater flow model for which groundwater recharge rates and distribution were determined using a deep percolation model (DPM) driven by historical climate data (Boyd, 1996). Here that model and the coupled groundwater model are used to investigate a new problem: the effects of climate change on recharge rates and groundwater discharge to streams.

The DPM calculates deep percolation (recharge) on a daily basis by partitioning precipitation through the major hydrologic compartments and fluxes. This partitioning is achieved by a series of physically based relationships which quantify hydrologic processes at each step. In this process, variables such as evapotranspiration, soil moisture, and surface runoff are calculated on a daily basis. The DPM was designed to simulate recharge primarily for large areas or regions with variable weather, soils, and land uses for input to groundwater flow models (Bauer and Vaccaro, 1987; Vaccaro, 2007).

Ultimately, the recharge and evapotranspiration output from the DPM were used to drive a three-dimensional finite difference groundwater flow model to understand the regional groundwater flow system in the upper Deschutes Basin. After the models'

development and because of the reasonable success achieved with them, it was believed that these coupled models could be used in future work as a predictive tool to assist water resource managers in making resource strategies and decisions (Gannett and Lite, 2004).

The Problem

Water resource management typically relies on records of historical streamflow. This approach relies on the premise that future climate variability, and hence streamflow variability, will not exceed past variability. However, this assumption is problematic in light of global warming (Milly et al., 2008). In fact, the climate in the Pacific Northwest appears to be changing (Feng and Hu, 2007). Thus, new tools are required for future water resource planning.

Warming due to climate change may affect the timing of recharge and runoff in the upper Deschutes basin markedly affecting groundwater levels (hydraulic head), groundwater discharge, and streamflow. Any one of these changes or a combination of them could render the past climate record of limited use for water resources planning and management. In particular because the majority of recharge for the basin originates as snowpack in the mountainous areas, and reservoirs supplying summer irrigation waters are located along upper elevation streams; it is important to examine and understand spatial changes in the basin's hydrology induced by climate change for the purposes of reservoir operations.

Climate change projections are made using coupled climate system models, broadly known as general circulation models or global climate models (GCMs), which compute temperature, precipitation, and other variable fields on a relatively coarse spatial scale. In order to be of use for basin-scale hydrological forecasting, the GCM model output must be downscaled to a spatial scale compatible with the DPM.

GCM projections, including daily temperature and precipitation, are available from many climate modeling centers for a standard suite of emission scenarios. Hindcasting, using GCMs to reproduce the historical record, demonstrates that the models realistically capture the statistics of historic climate. The University of Washington's Climate Impacts Group (CIG) has evaluated model performance in the Pacific Northwest and their preferred model suite is used here. The CIG also provides downscaled GCM output fields appropriate for basin-scale research.

Decadal scale climate oscillations are the largest signal affecting the Deschutes Basin's water table levels in the historical record (Gannett et al., 2001). This implies that climate is the main external factor driving variations in groundwater storage and discharge, making attention to climate change an important priority for water management in the basin. In this study; downscaled global climate model data, a deep percolation model, and a groundwater flow model are used to investigate the evolution of the hydrologic budget, particularly recharge and runoff, resulting from probable climate trends in the upper Deschutes Basin through the 21st century. GCM precipitation and temperature output, downscaled to 1/16th degree, are used to drive the DPM and

groundwater flow model that have both been calibrated to the basin. The result is a predictive tool to assist water resource managers and water users.

DESCRIPTION OF THE STUDY AREA

Geography

The upper Deschutes Basin study area, located in central Oregon, encompasses approximately 4,500 square miles (Figure 1). The basin is bounded on the north by Jefferson Creek, the Metolius River, the Deschutes River, and Trout Creek; on the east by the contact between the Deschutes Formation and the older, relatively impermeable John Day Formation; on the south by the drainage divide between the Deschutes Basin and the Fort Rock and Klamath Basins; and on the west by the Cascade Range crest (Lite and Gannett, 2002). A broad upland plain extends from the Cascades to the foothills of the Ochoco Mountains in the northeastern portion of the study area. Crane Prairie and Wickiup Reservoirs located in the southwestern portion of the study area, provide water for the summer irrigation to the central, agricultural portions of the basin (Figure 1). Most population centers and agricultural areas are located on the upland plain (Boyd, 1996). Groundwater is the principal source of municipal water supplies. Most of the irrigation waters supplying approximately 164,000 acres of agricultural land are diverted from the Deschutes River near Bend, although some lands are irrigated using groundwater (Lite and Gannett, 2002). The area north of Bend is crossed by an extensive network of canals.

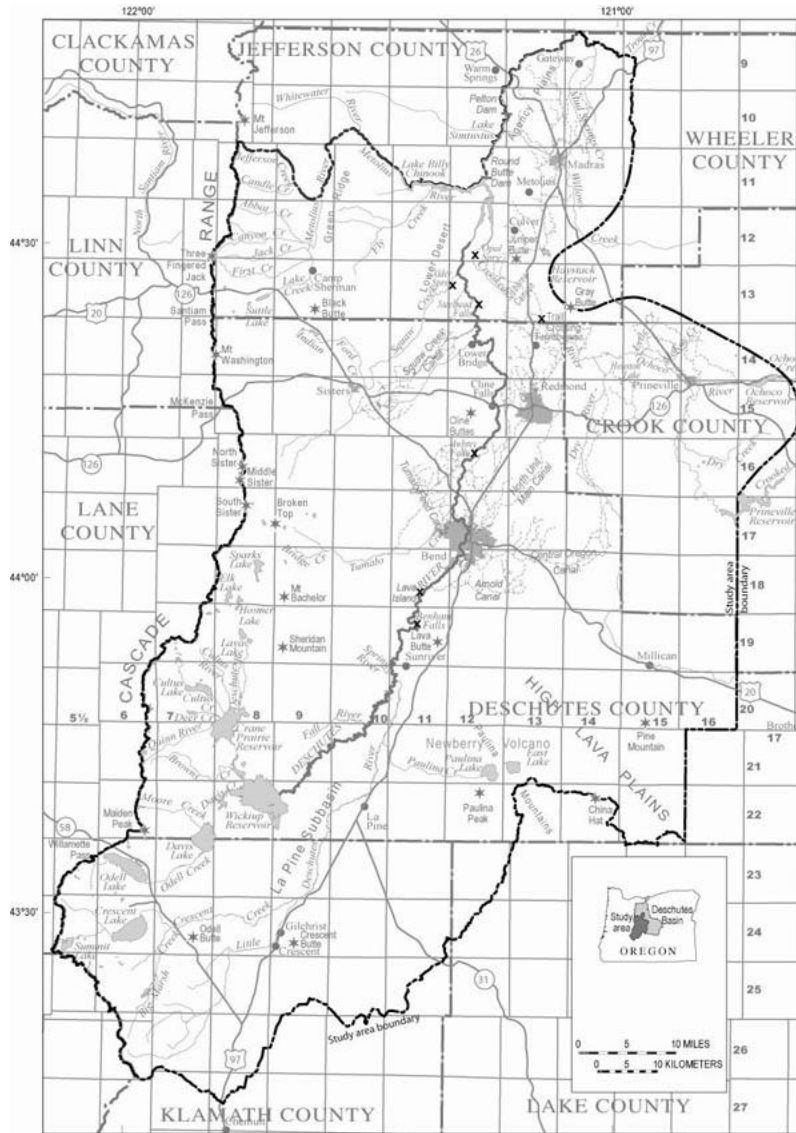


Figure 1. The location of the upper Deschutes Basin in central Oregon, from Lite and Gannet (2001).

Elevations tend to grade from the southern, uppermost portion of the basin, downward toward the north-northeastern basin boundary. Elevation of the land surface in the study area ranges from about 1,300 ft above sea level northeast of the town of

Madras to 10,358 ft in the Cascades along the western boundary (Gannett et al., 2001; Lite and Gannett, 2002). The regional groundwater flow tends to follow this trend.

A high desert climate with warm, dry summers and cool wet winters is typical throughout the basin. As air masses move generally west to east across Oregon, the orographic control of the Cascades has a direct effect on precipitation and temperature distribution in the basin (Lite and Gannett, 2002). Precipitation in the Cascades can locally surpass 200 inches per year, falling primarily as snow during the winter (Taylor, 1993). Precipitation rates decrease rapidly toward the east with less than 10 inches per year falling in central and eastern portions of the region (Lite and Gannett, 2002).

Geologic Setting

The majority of the upper Deschutes Basin is within the Cascade Range geologic province and the Basin and range Province (Lite and Gannett, 2002). The geologic features in this region are the result of volcanic activity since the Oligocene along a north-south trending volcanic arc (Sherrod and Smith, 2000) (Figure 2). Late Miocene volcanic and tectonic activity in the Basin and Range Province, including the High Lava Plains, has been significant in shaping the current landscape (Lite and Gannett, 2002).

The oldest and stratigraphically lowest unit in the study area is the late Eocene to early Miocene John Day Formation. This formation is composed primarily of pyroclastic sequences with locally occurring lava flows near the base (Robinson et al., 1984). The units in this formation generally have low permeability due to diagenetic alteration

(Gannett et al., 2001). Because of this, the John Day formation is considered to be the hydrologic basement for the regional groundwater flow system (Lite and Gannett, 2002). This formation is seen in outcrops along the northern and eastern edges of the study area.

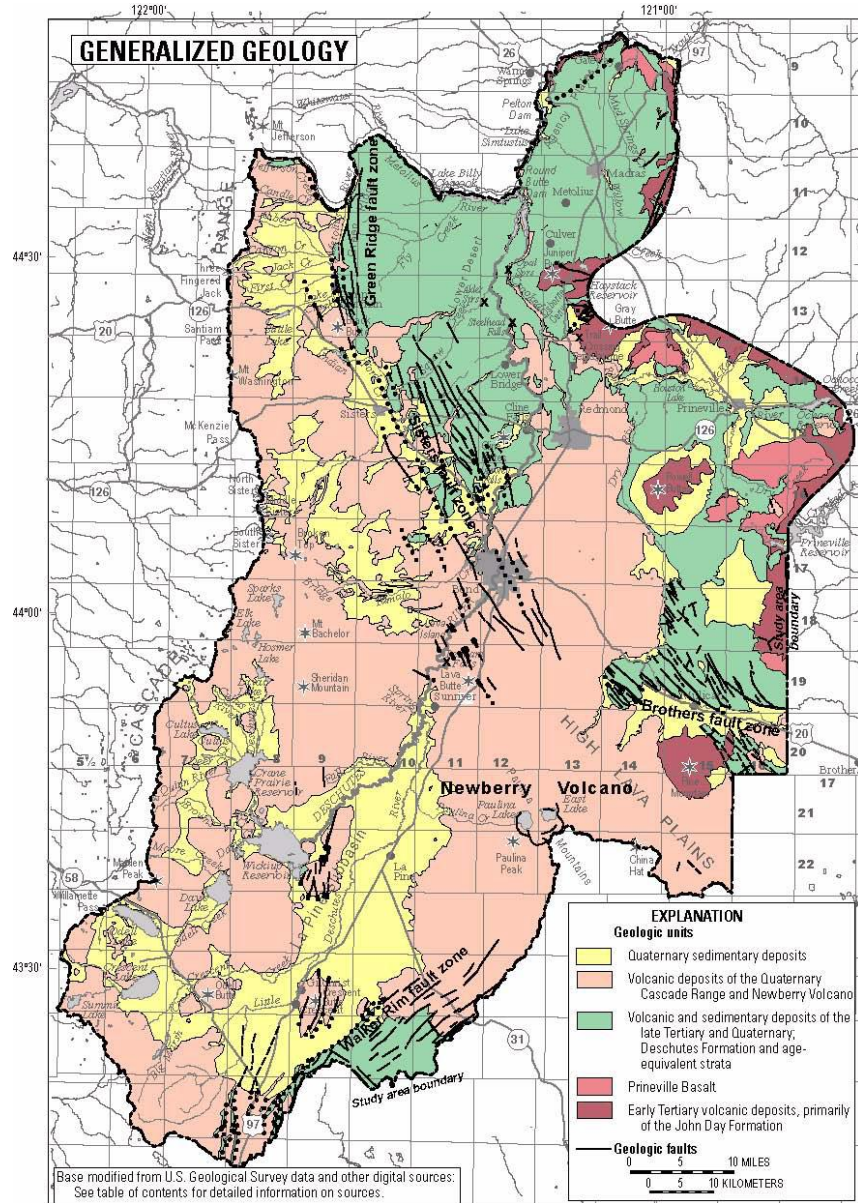


Figure 2. Generalized geology of the Upper Deschutes Basin from Gannett and Lite (2004).

Immediately above the John Day Formation is the middle Miocene Prineville Basalt. The few hundred feet of fractured lava flows in this formation underlie the extreme northeastern portion of the study area (Lite and Gannett, 2002).

The late Miocene to early Pliocene Deschutes Formation is exposed in the north central portion of the study area. It is the principal aquifer here and is composed of multiple volcanic, volcanistic, and epiclastic units that have filled the basin (Lite and Gannett, 2002). Several intrabasin vents ranging from basalt to rhyolite have been identified within this formation (Sherrod et al., 2004).

Late Tertiary to Quaternary lava flows, lava domes, volcanic vents, pyroclastic deposits, and epiclastic sediments compose the western and southern regions of the study area (Sherrod and Smith, 2000). Most of the precipitation contributing to groundwater recharge percolates through these sediments and fractured flows (Lite and Gannett, 2002). Additionally, permeable Quaternary sedimentary deposits exist along and near stream networks within the field area and, permeable Quaternary glacial deposits are located along the western margin of the region.

Tectonic Structures

Faults and fault bounded grabens are common in the basin. These structures create permeability contrasts that affect groundwater flow through juxtaposition of permeable units in the field area and grabens forming depositional centers (Lite and Gannett, 2002). Notable structural zones in the field area include the Cyrus Springs Fault

Zone, the Brothers Fault Zone, the Sisters Fault Zone, and the Walker Rim Fault Zone (Figure 2). Other structures include the Green Ridge (intra-arc graben) escarpment, and the La Pine and Shukash Grabens.

The geology of the Upper Deschutes basin is a major control on the basin's hydrology. The combination of highly permeable volcanic deposits with high precipitation in the Cascade Range results in a large proportion of the precipitation (and snowmelt) infiltrating to become groundwater. This groundwater discharges to streams down gradient in response to stratigraphic, structural, and topographic controls. As a result, the flow of many streams in the study area is almost entirely baseflow. This is especially true during the dry summer months.

Hydrogeologic Units

Geologic units are often combined or subdivided into hydrogeologic units according to their hydrogeologic properties. As the emphasis is on hydrogeologic properties, a hydrogeologic unit can be comprised of a single geologic unit, groups of geologic units, or zones within a single geologic unit. All three situations are found in the upper Deschutes Basin (Lite and Gannett, 2002).

Seven hydrogeologic units were delineated and characterized in the basin by Lite and Gannett (2002) (Figure 3). The first four of these units have the highest permeabilities and are within the Deschutes Formation.

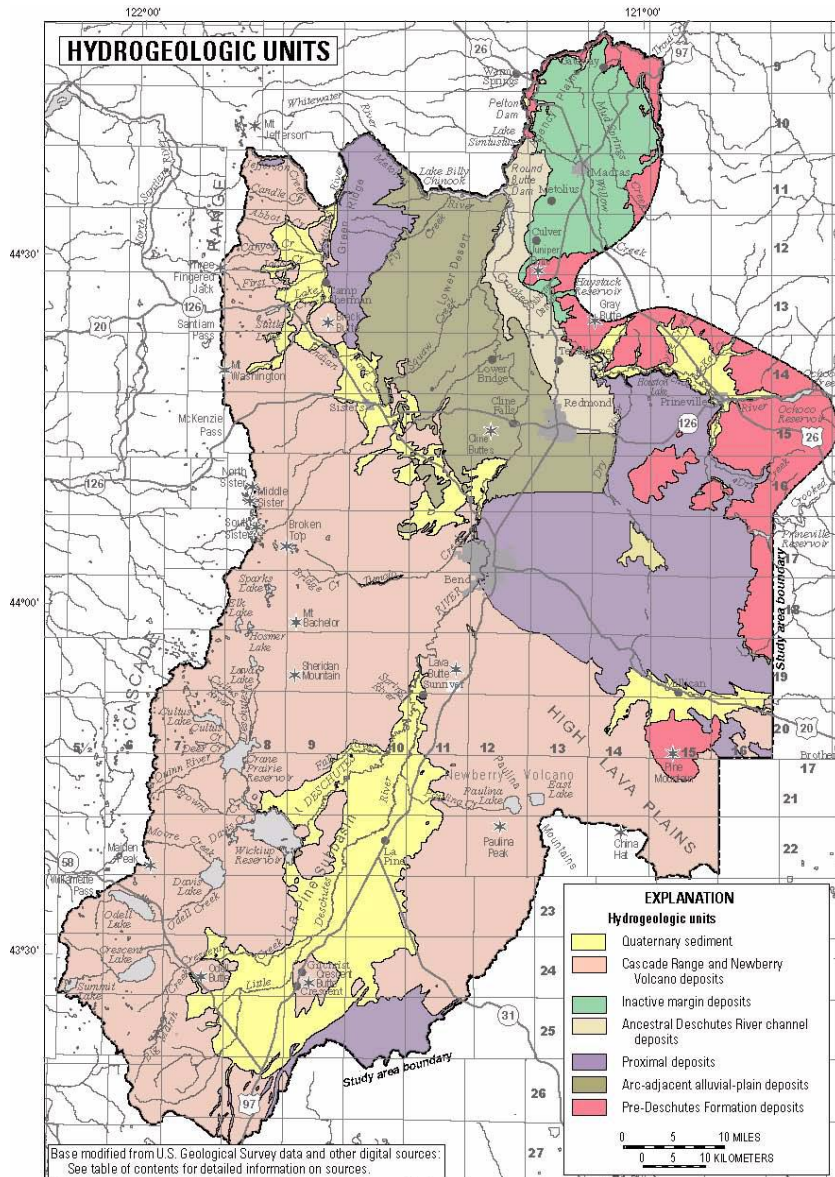


Figure 3. Hydrogeologic units of the upper Deschutes Basin from (Lite and Gannett, 2002).

1. Proximal lava flows including undifferentiated volcanic deposits are the largest and most extensive in the basin. Some lava flows in this unit are

not mapped as Deschutes Formation but are from the same time period.

The unit ranges from permeable to locally highly permeable with well yields up to 2,000 gal/min (0.1262 m³/s) (Lite and Gannett, 2002).

2. Arc-adjacent alluvial-plain facies consisting of sediment interbedded with lava flows and ash fall tuff comprise the second hydrogeologic unit in the Deschutes Formation. This unit is more geologically diverse than surrounding units and is permeable to locally highly permeable. Large capacity irrigation wells in the Lower Bridge area draw from this unit with well yields up to 4,000 gal/min (0.2523 m³/s) (Lite and Gannett, 2002).
3. The generally highly permeable ancestral Deschutes River channel facies is the third unit in the Deschutes Formation. The unit is mostly coarse sand and gravel, intercanyon lava flows, and distal parts of ash-flow tuffs. Well yields range from 2,300 gal/min (0.1451 m³/s) in the vicinity of Redmond to 5,000 gal/min (0.3154 m³/s) at Opal Springs. Highly fractured basalts in this unit contribute to high well yields (Lite and Gannett, 2002).
4. The last unit within the Deschutes Formation is the inactive margin facies. The unit is comprised of fine-grained clastic and pyroclastic material. Therefore it generally has low permeability. Well yields range from 30 to 300 gal/min (1.9 x 10⁻³ to 1.89 x 10⁻² m³/s) (Lite and Gannett, 2002).

5. The coarse grained Quaternary alluvial and glacial outwash sediments along stream networks and the western margin respectively form another hydrogeologic unit. These sediments are permeable and produce where saturated with well yields of 10 to 300 gal/min (6×10^{-5} to 1.89×10^{-2} m³/s).
6. The permeable volcanic deposits of the Cascade Range and Newberry Crater, not including hydrothermally altered rocks at depth, are another hydrogeologic unit in the basin. The unit is comprised of permeable lava flows with minor pyroclastic and volcaniclastic interbeds. This unit is extensive in the western and southern parts of the study area.
7. The last unit, with the lowest permeability consists of Prineville Basalt, John Day Formation, and hydrothermally altered rocks beneath Newberry and the Cascade Range. These all pre-date the Deschutes Formation.

These general hydrologic units based on expressions of surface geology have been further subdivided as specified flux boundaries in both the DPM and regional groundwater flow model.

MODEL DESCRIPTIONS

The work described herein involves the application of a series of computer models beginning with climate models. The processed output of the climate models is used to drive the DPM which, in turn, provides the specified recharge fluxes and maximum ET rates for the groundwater flow model.

Climate System Model Output

Global climate system models (GCMs) simulate interactions among components of Earth's climate system in three dimensions, including the atmosphere, land surface, and ocean. Future climate projections are made by initializing the GCM using information about the historical climate and then run forward in time using atmospheric conditions that reflect expected greenhouse gas (GHG) emissions. These conditions come from GHG scenarios developed by the Intergovernmental Panel on Climate Change (IPCC). Of the many variables involved in a GCM, temperature and precipitation are of interest here. GCM output used in the present study comes from eight different models shown to realistically simulate the climate of the Pacific Northwest (Salathe et al., 2007; Table 1).

Table 1. Names of the GCM used in this research including citations, institution where the models where developed, and countries of origin.

Model Name (Citation)	Institution(s)	Country
CCSM3 (Collins et al., 2006)	National Center for Atmospheric Research	USA
CNRM-CM3 (Salas-Mélia et al., 2006)	Centre National de Recherches Météorologiques	France
ECHAM5/MPI-OM (Jungclaus et al., 2006)	Max Planck Institute for Meteorology	Germany
ECHO-G (Legutke et al., 1999)	Meteorological Institute of the University of Bonn Institute of KMA Model and Data Group	Germany Korea
HadCM3 (Gordon et al., 2000)	Hadley Centre for Climate Prediction and Research	UK
IPSL-CM4 (Marti et al., 2005)	Institut Pierre Simon Laplace	France
MIROC 3.2 (Hasumi and Emori, 2004)	Center for Climate System Research, University of Tokyo National Frontier Research Center for Global Change Institute for Environmental Studies	Japan
PCM (Washington et al., 2000)	National Center for Atmospheric Research	USA

Two IPCC emission scenarios are considered here, A1B and B1. A1B is a relatively high emission scenario, though not the highest considered by the IPCC, while B1 is the lowest of the IPCC scenarios. The resulting ensemble of 16 GCM projections is used to drive the DPM and investigate hydrologic response in the upper Deschutes Basin for three 30-year climate periods (Table 2). The results are averaged to create a multi-

model mean. One minor adjustment is made to account for the shorter simulation time period of the PCM model (Table 1). Model output in that case ends in 2098 so its final climate period is 29 years, 1/1/2070 to 12/31/2098.

Table 2. The four thirty year climate periods as defined for this study.

climate period	start date	end date
1980s	1/1/1970	12/31/1999
2020s	1/1/2010	12/31/2039
2050s	1/1/2040	12/31/2069
2080s	1/1/2070	12/31/2099

GCMs used for climate projections are run with a range of spatial resolutions, usually 2 degrees or coarser. This resolution is not fine enough for basin-scale studies and so the GCM output must be mapped onto a finer local grid. Here, downscaled data is provided by the University of Washington Climate Impacts Group (CIG), via Dr. Heejun Chang in the Portland State University Department of Geography. For these datasets, CIG uses a bias-correction and spatial disaggregation (BCSD) method to map GCM fields to a 1/16th degree grid (Salathe et al., 2007).

Bias Correction and Spatial Disaggregation Downscaling

Bias correction accounts for mean differences between observed and model-simulated fields. The goal is to produce a regional climate projection with no bias with respect to a historical data set, on the model grid. A number of bias-correction methods

have been developed, and the CIG uses the method of Wood et al. (2002), which statistically matches modeled and observed fields over a historical evaluation period. The CIG procedure uses 1950 to 1999 as a training period. First, the observed monthly data for a climate variable is accrued to the climate grid in question. Cumulative distribution functions (CDF) are calculated for observed and modeled monthly mean values during the training period, establishing nonexceedence probabilities at each model grid cell for each month for a variable of interest (Salathe et al., 2007; Wood et al., 2002). Bias correcting transfer functions are created using the inverse CDF for the observed base period data and the CDF for each month in each year of the historic and 21st century GCM runs (Salathe et al., 2007). In effect, the original simulated values are replaced with values having the same nonexceedence probabilities with respect to the observed climatology that the GCM values had with respect to the GCM climatology for every grid cell and calendar month (Wood et al., 2002).

The bias-corrected data must be downscaled to an appropriate grid resolution. The CIG procedure uses different techniques for the temperature and precipitation data (Salathe et al., 2007). For precipitation, local perturbations to the regional field are computed using the historical period 1950 to 1999. These perturbations are then modified to preserve details related to atmospheric circulation (weather patterns) and used to scale, by multiplication, the GCM output grid to the 1/16th degree grid (Widmann et al., 2003). For temperature, local perturbations are computed similarly but no other predictors are

used to modify these perturbations. Temperature perturbations are used to shift, by addition, the GCM output grid to the 1/16th degree grid (Salathe, 2005).

The BCSD downscaling yields monthly time series of mean temperature and total precipitation on a 1/16th degree grid (Salathe et al., 2007). In order to use this data with a daily time step hydrologic model, the data must be temporally disaggregated to produce transient daily time series of total precipitation, and minimum and maximum daily temperatures. This is performed by the CIG using empirical orthogonal function (EOF) analysis to select an analog calendar month from the observed record whose monthly mean spatial precipitation pattern most closely resembles the calendar month to be disaggregated (Salathe et al., 2007). After the analog month is selected, the observed daily values for each centroid are adjusted to the monthly mean producing the disaggregated downscaled time series for both precipitation and temperature (Salathe, 2005). The daily precipitation sequence at each centroid from the analog month is scaled by the ratio of the downscaled monthly mean to the analog monthly mean preserving the downscaled monthly mean (Salathe et al., 2007). For temperature, daily minimums and daily maximums through a year are shifted equally so that their average reproduces the average temperature for a month from the ensemble model member (Salathe et al., 2007; Wood et al., 2002).

Deep Percolation Model

Overview

The Deep Percolation Model is a physically based mass-balance model that operates on a daily time step to estimate groundwater recharge (Bauer and Vaccaro, 1987; Vaccaro, 2007). The model was primarily designed to produce multiyear estimates of recharge (deep percolation) for input into regional groundwater flow models (Vaccaro, 2007). The DPM calculates the water balance for an array of polygons termed hydrologic response units (HRUs) within the model domain. The daily water-budget values can be used to calculate means for longer time periods as needed to match the stress periods of groundwater flow models.

The DPM computes groundwater recharge, R , for each HRU in a region as the residual of various water and energy budget components (Vaccaro, 2007). The initial total precipitation amount is subject to actual evapotranspiration AET and surface runoff SRO . Additionally, the accounting must consider changes in snowpack SNO , soil moisture SM and intercepted moisture storage IS :

$$R = P - AET - SRO - (\Delta SNO + \Delta SM + \Delta IS) \quad (1)$$

In this case, actual evapotranspiration includes soil evaporation, plant transpiration, evaporation of intercepted water, and snow sublimation (Vaccaro, 2007). Equation (1) has been adapted from Vaccaro (2007).

The data needed to drive the DPM includes daily precipitation and daily minimum and maximum surface temperatures (Bauer and Vaccaro, 1987). Daily solar radiation is also an important input but is not readily available with the downscaled GCM products. As an alternative, an equation based on the empirical relationship between temperature and solar radiation is used here (Allen, 1997). Solar radiation is used in potential evaporation calculations for HRUs with non-agricultural land use; otherwise, if no data are input, the model will calculate clear-sky radiation as a function of latitude, slope, aspect, and day of the year (Vaccaro, 2007). These input data are interpolated to HRUs throughout the domain, and the precipitation is partitioned into hydrologic components (evapotranspiration, intercepted water, throughflow, interflow, runoff, etc.) via established empirical relationships using the weather data and parameters from spatially distributed data (Bauer and Vaccaro, 1987; Vaccaro, 2007).

Pertinent physical properties are defined for each HRU including available soil water capacity, soil thickness, soil texture, land use, vegetation cover, rooting depths, interception capacities, long-term average annual precipitation, land-surface elevation, slope and aspect, temperature lapse rates, and daily stream discharge (Bauer and Vaccaro, 1987; Vaccaro, 2007). Daily stream discharge is an optional parameter for HRUs and is not specified for use in the upper Deschutes Basin DPM.

The DPM determines the partitioning of precipitation at any given time step according to temperature and soil properties at the prior step. This requires a series of

evaluations and corresponding calculations, as described schematically in Figure 4 (following Bauer and Vaccaro, 1987). All quantities are calculated on a daily time step. Daily precipitation is specified as being either rain or snow depending upon average temperature. Snowpack storage is subject to sublimation at the 0° C threshold while intercepted rain is subject to evaporation. Remaining precipitation is assigned as water on the ground. Depending on soil properties and level of saturation, surface runoff

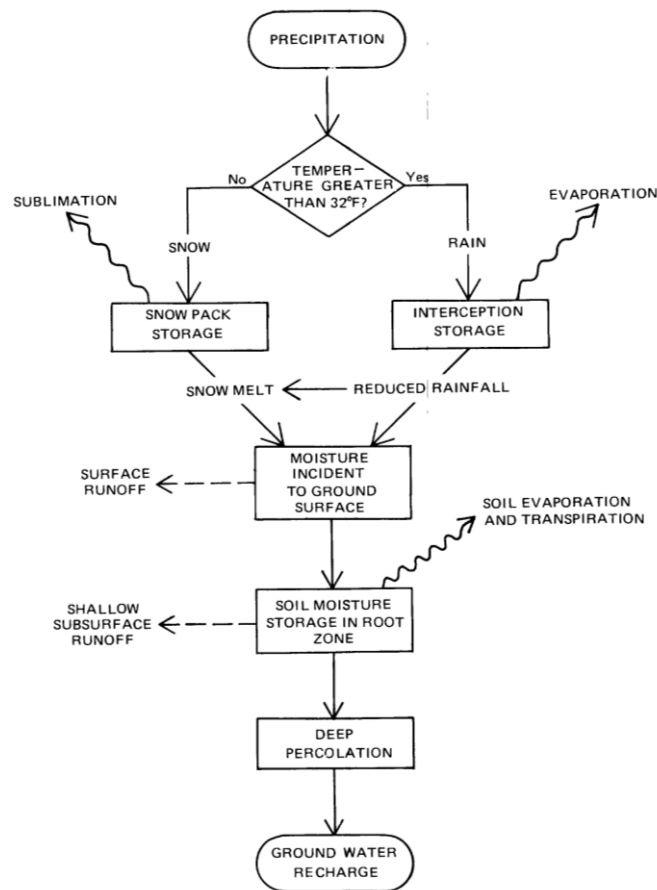


Figure 4. Conceptual flow model of the water balance, from Bauer and Vaccaro (1987).

is then partitioned from infiltrating water. A portion of the water moving through the root zone is lost to soil evaporation, plant transpiration, and interflow while the remainder becomes recharge.

Deschutes Basin DPM

A DPM was calibrated for the upper Deschutes Basin and employed for the estimation of groundwater recharge (Boyd, 1996). The DPM was calibrated by comparing model simulated recharge and runoff to measured runoff and assumed baseflow at a stream gauging station at the lowest point of the model from 1961 to 1994, effectively integrating conditions in the entire upper Deschutes Basin (Boyd, 1996). Calibration at the subbasin scale was largely unsuccessful. It is hypothesized that groundwater flow between subbasins occurs which cannot be accounted for by the model (Boyd, 1996).

Model boundaries and domain

Horizontal boundaries for the upper Deschutes Basin model domain are the drainage divides that surround the basin, except where the generalized Deschutes Formation / John Day Formation geologic contact is used along the eastern boundary (Boyd, 1996). Both the drainage divides and the contact are considered no-flow boundaries for groundwater, and the only sizeable quantity of surface water that enters the basin is from the Crooked River. This external flux was accounted for during the

calibration process (Boyd, 1996). The model domain was divided into a grid of 3,471 square HRUs with dimensions of 6000 ft (1829 m) per side (Figure 5).

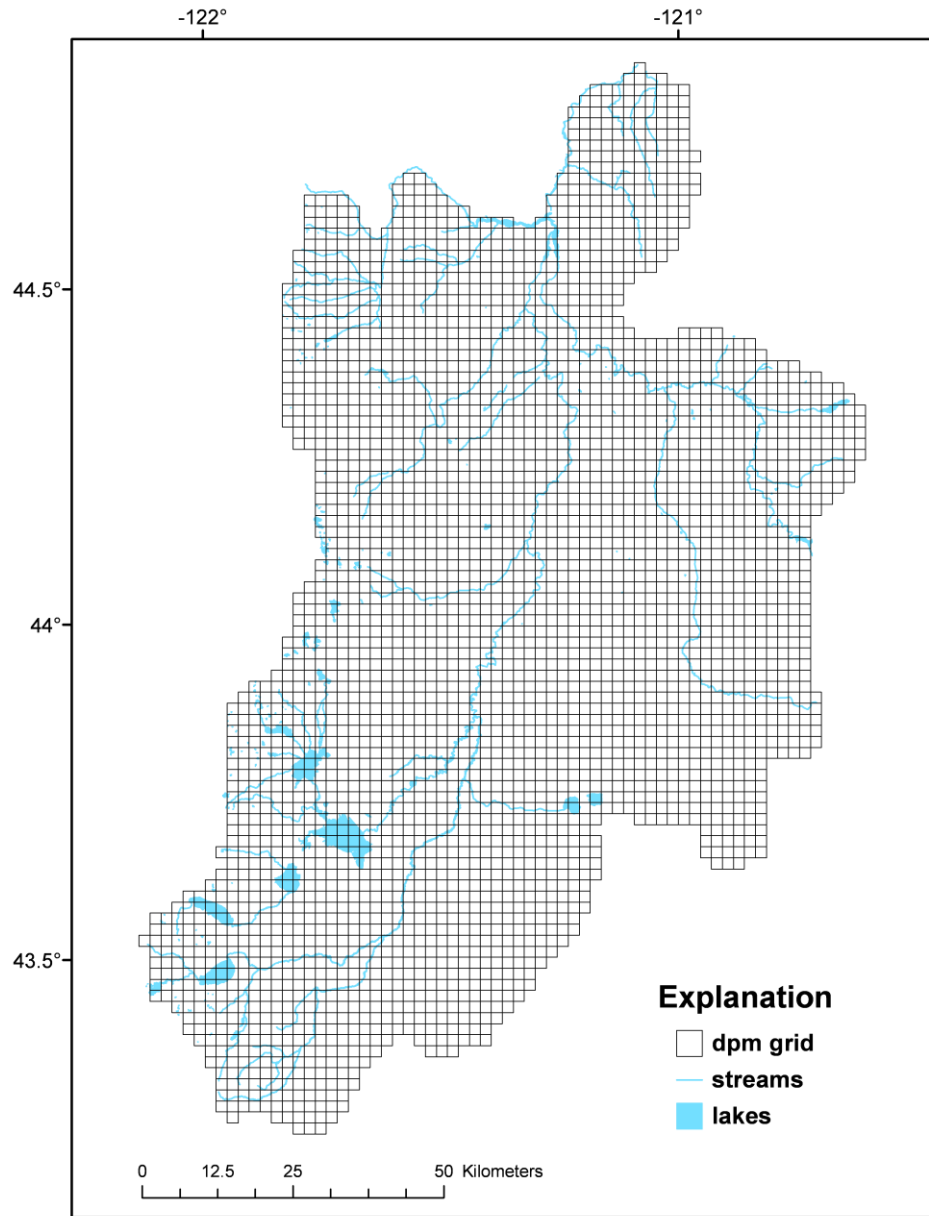


Figure 5. DPM grid for the upper Deschutes Basin. Grid cell dimensions are 1829 meters by 1829 meters.

Spatially Distributed Data

Each model grid cell contains the following spatially distributed data as specified by Bauer and Vaccaro (1987) and Vaccaro (2007): long term average annual precipitation, soil type, land cover type, average land surface altitude, average slope, average aspect, longitude, latitude, effective length (half the average spacing between smallest drainage channels), and effective slope (average slope between smallest drainage channels) (Boyd, 1996).

Long term average annual precipitation data for the basin comes from the Precipitation-elevation Regressions on Independent Slopes Model (PRISM) (Daly et al., 1994). Soil data including the ratio of sand, silt, and clay; properties; and thickness (number of six inch layers) for each type used by the model, came from the State Soil Geographic Database and was supplied to Boyd (1996) by the U.S. Department of Agriculture, Soil Conservation Service in Portland, Oregon. Using this soil data and cluster analysis, Boyd (1996) reduced the number of soils in the basin to ten hydrologic soil types (Figure 6). Four land cover types are used in the basin and each has specific values for maximum root depth, maximum foliar cover, and maximum interception storage capacity (Figure 7) (Boyd, 1996).

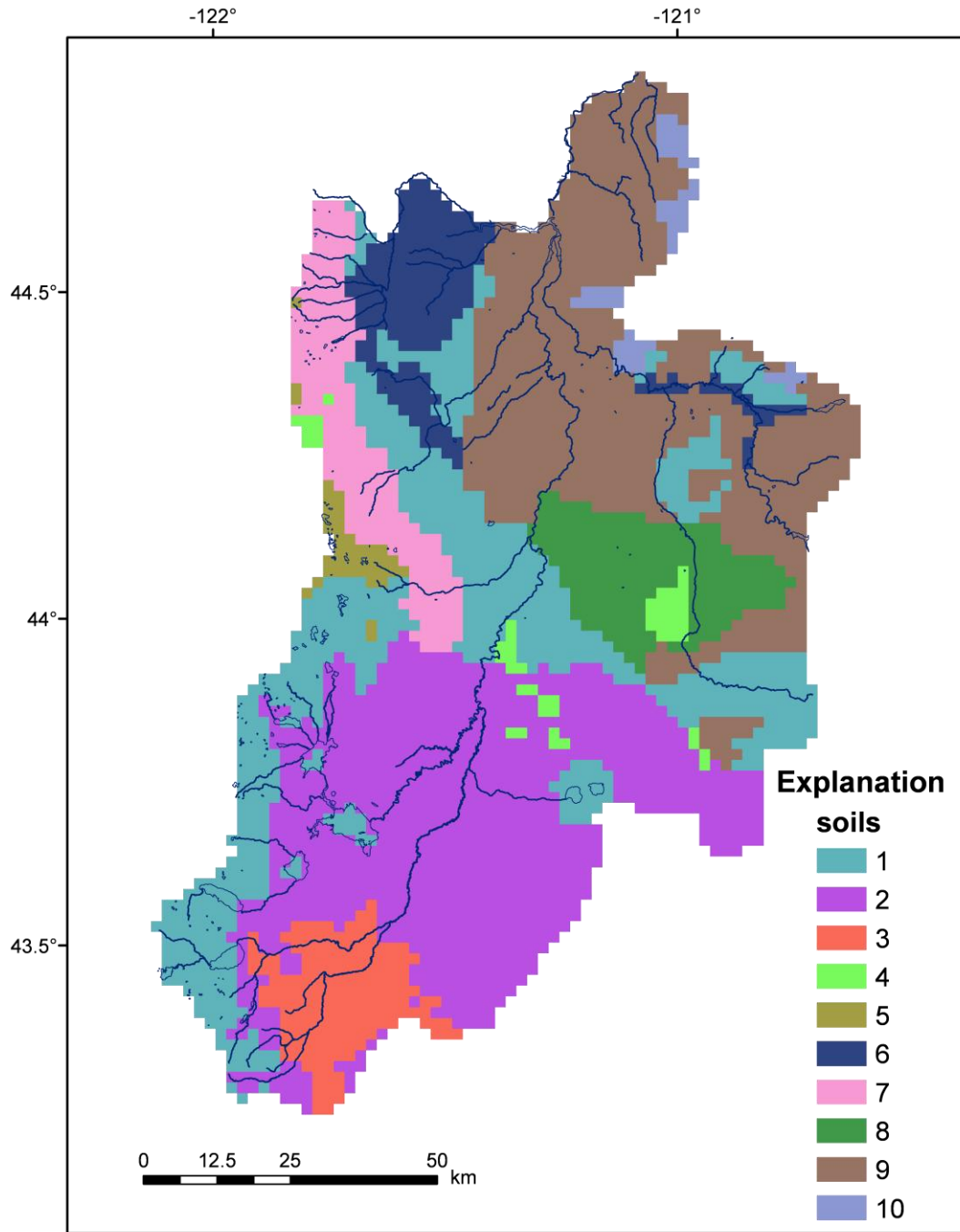


Figure 6. The spatial distribution of the ten hydrologic soil types used by the Deschutes Basin DPM.

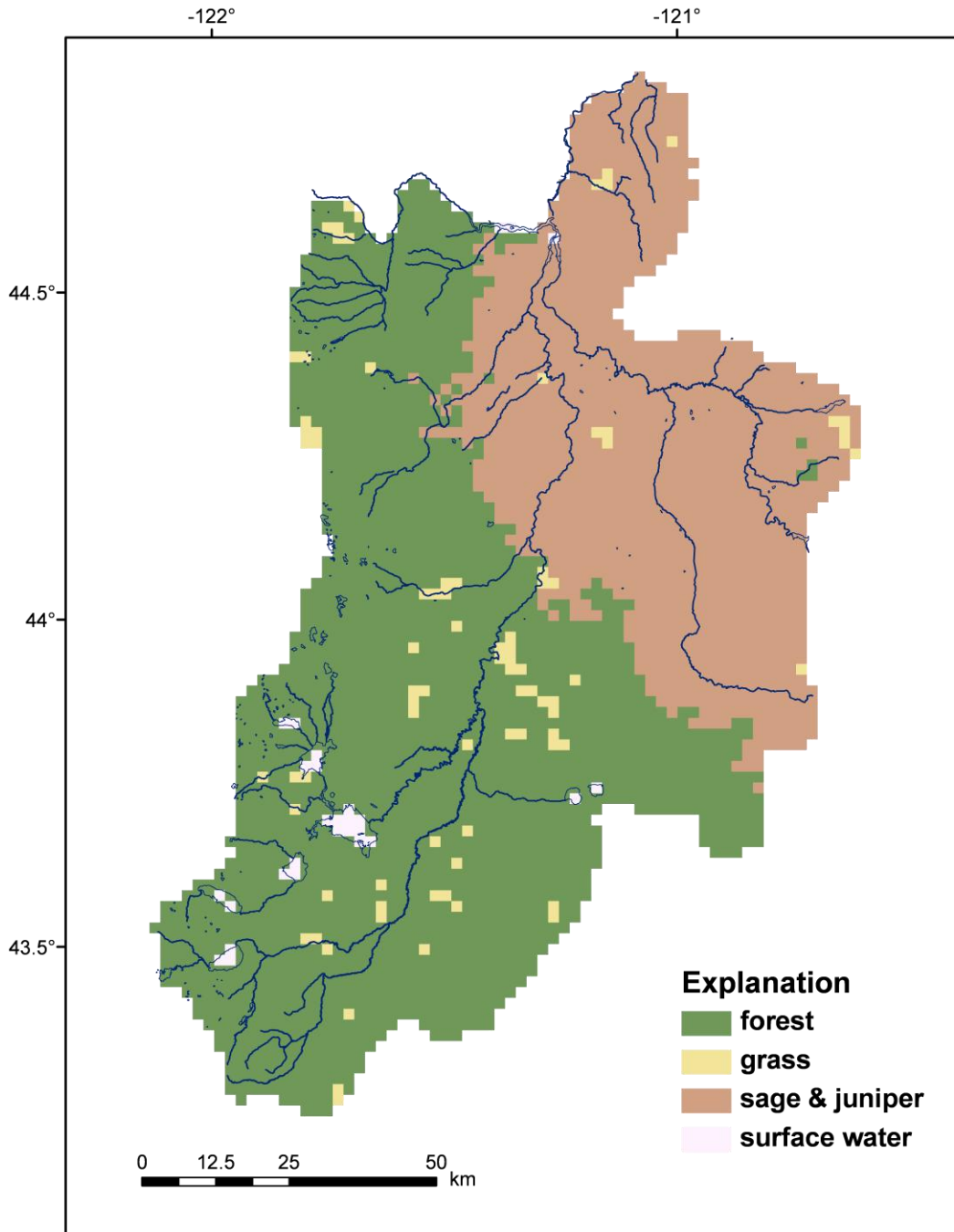


Figure 7. The spatial distribution of the four land cover types used by the Deschutes Basin DPM.

Daily Weather Data

Daily weather data from six climate stations in the basin are conditionally interpolated throughout the basin by the model (Table 3). However, not all stations provide all types of weather data. Daily precipitation and temperature data recorded at five weather stations are used by the model, while Redmond Roberts Airfield is the only station to provide daily solar radiation.

Table 3. Weather stations used by the DPM to interpolate weather data throughout the basin, table adapted from Boyd (1996).

Climate Station	Station ID	Elevation above sea level (m)	Precipitation Stations	Temperature and Dew Point	Solar Radiation
Bend	0694	1112.5	X	X	
Brothers	1067	1414.3		X	
Madras	5139	679.7	X		
Prineville 4 NW	6883	865.6	X	X	
Redmond Roberts Field					
FAA	7062	932.7	X	X	X
Wikiup Dam	9316	1328.9	X	X	

Temperature and precipitation are interpolated to grid cells using an inverse distance squared (IDS) weighting method from climate stations within 80.5 km of the grid cell in question (Bauer and Vaccaro, 1987; Boyd, 1996). For precipitation the IDS weighting is scaled by the ratio of average annual precipitation of the cell to the station. For temperature, and associated PET, the IDS weighting is corrected with monthly

temperature lapse rates and elevation differences between the cell and climate stations (Bauer and Vaccaro, 1987; Boyd, 1996).

Regional Groundwater Model

The regional groundwater flow model of Gannett and Lite (2004) for the upper Deschutes Basin employs the U.S. Geological Survey modular three-dimensional finite-difference groundwater flow modeling code (MODFLOW) developed by McDonald and Harbaugh (1988). This numerical model solves discretized equations for the movement of groundwater through porous media which is described by Darcy's Law and the conservation of mass (Gannett and Lite, 2004; McDonald and Harbaugh, 1988). The governing equation is:

$$\frac{\partial}{\partial x} \left(K_{xx} \frac{\partial h}{\partial x} \right) + \frac{\partial}{\partial y} \left(K_{yy} \frac{\partial h}{\partial y} \right) + \frac{\partial}{\partial z} \left(K_{zz} \frac{\partial h}{\partial z} \right) - W = S_s \frac{\partial h}{\partial t} \quad (2)$$

where K_{xx} , K_{yy} , and K_{zz} are values of hydraulic conductivity in the x, y and z directions in a Cartesian coordinate system, with axes assumed to align with principal directions of hydraulic conductivity (LT⁻¹), h is hydraulic head (L), W is a volumetric flux per unit volume and represents sinks and/or sources (T⁻¹), S_s is the specific storage of the porous material (L⁻¹), and t is time (T) (from Gannett and Lite 2004).

Spatial discretization and boundary conditions

The regional groundwater flow system of the basin is represented as an array of 127 rows, 87 columns, and 8 layers. Lateral dimensions of grid cells ranges from 2000 feet to 10,000 feet (609.6 m to 3048 m) per side. Each layer is uniform in thickness and thicknesses range from 100 feet (30.48 m) for the first 5 layers to 800 feet (243.84 m) for the bottom layer (Gannett and Lite, 2004). The thickness of the bottommost layer varied depending on the elevation of the basement confining unit that defines the base of the model.

Boundary conditions used in the model include no-flow, head-dependent flux, and specified flux boundaries. Most geographic boundaries are represented by no-flow boundary conditions. Streams within the basin are represented as head-dependent flux boundaries across which groundwater moves to or from a stream at a rate proportional to the difference in hydraulic head between the aquifer and stream stage. Recharge was determined using the DPM and is a specified flux boundary condition (Gannett and Lite, 2004). Evapotranspiration (ET) directly from the water table by phreatophytes is simulated as a head dependent flux boundary with a maximum rate based on the difference between potential and actual ET calculated by the DPM. On farm-losses in agricultural areas of the basin and irrigation canal leakage are specified flux boundaries calculated independently from field data (Gannett and Lite, 2004)

Transient simulations of regional groundwater flow in the Deschutes basin can run on monthly time steps.

METHODS

Historical Daily Climate Data

Acquisition of up-to-date historic climate data was necessary in order to update model validation and assess prior calibration. Historical daily climate data was acquired through September 2008 in the following manner: Daily precipitation and temperature data from 1997 through 9/30/2008 for the six climate stations in the basin were downloaded from NNDC Climate Data Online (NOAA Satellite and Information Service and National Climatic Data Center, 2009). Precipitation and temperature data were downloaded from the Bureau of Reclamation's Agrimet website from automated agricultural weather stations (Bureau of Reclamation, 2009). These Agrimet sites are near the Bend, Madras, and Redmond climate stations, respectively, and the data from these sites was expected to correlate to the NNDC weather stations. Data availability varies from site to site but as much temperature and precipitation data for the 1997-2008 time period as possible were collected. Temperature and precipitation data was downloaded from 05/01/2003 through 09/30/2008 from the site near Bend and from 01/01/1997 from the sites near Redmond (Powell Butte) and Madras. Solar data was downloaded from Agrimet from 01/01/1985 through 2008 for their Madras site and from 09/01/1993 to 09/30/2008 for their Powell Butte site.

There were many instances of missing or questionable data in the precipitation and temperature records. Data gaps were repaired by linearly regressing NNDC against Agrimet data. The procedure worked well for temperature but not for precipitation so the

normal ratio method was used to fill values for missing precipitation data at the six climate stations (Dunne and Leopold, 1978). An example of the general normal ratio equation used to fill a missing precipitation value for the Bend climate station is:

$$P_{Bend} = \frac{1}{5} [(N_{Bend} / N_{Brothers}) * P_{Brothers} + (N_{Bend} / N_{Madras}) * P_{Madras} + (N_{Bend} / N_{Prineville}) * P_{Prineville} + (N_{Bend} / N_{Redmond}) * P_{Redmond} + (N_{Bend} / N_{Wickiup}) * P_{Wickiup}] \quad (3)$$

in which subscripted P are precipitation values for or at indicated climate stations, and subscripted N are long term normal annual precipitation at the indicated stations.

The long term normal annual precipitation are (1971 to 2000) means at each climate station, obtained from the Oregon Climate Service (Oregon Climate Service, 2009). In some instances, more than one station was missing precipitation on the same day and equation (3) was adjusted accordingly.

All regressions on climate station data in this study are performed at the 0.05 level of significance, although the number of regressors used varies with available data.

Missing daily temperature values for Brothers, Prineville, and Bend were added to the daily temperature data sets by regressing temperature data against data from the other available NNDC climate stations. As a missing record on a particular day for one station may be accompanied by a missing record from one or more other stations, several possible combinations of linear multiple regressions were required to fill the gaps dependent upon the station in question. Regressors For the Brothers' station include all other stations, all minus Prineville station, all minus Redmond station, and all minus

Prineville and Redmond stations for missing daily minimum temperatures for a total of four regression equations (Appendix A.1). The same is true for the missing maximum daily temperatures at Brothers (Appendix A.2). Regressors for the missing Prineville minimum temperatures include many possible combinations reflecting the fact that this is the most incomplete dataset of any in the basin with nine necessary regression equations (Appendix A.3). Missing maximum temperatures for Prineville are somewhat less requiring two less regression equations (Appendix A.4). The missing minimum and maximum temperatures for the Bend station required five regression equations (Appendix A.5-A.6). Additionally, two missing minimum temperature values for Wickiup were added to daily temperature sets in the same manner (Appendix A.7). For the aforementioned stations, this method of using as many stations' temperature data as possible in regression equations was found to have the highest correlations, lowest standard errors, and lowest mean residuals for these stations as opposed to linear regressions of missing temperatures against a single climate station. The last climate station used for distributing temperatures by the DPM, Redmond, was found to have the highest correlation, lowest standard error, and lowest average residual when linearly regressed against a nearby Agrimet weather station site (Appendix A.8). Consequently, these linear regression equations were used to create values for gaps in the temperature record at these sites.

The original solar data used to calibrate the DPM for the upper Deschutes basin came from observations at Redmond Roberts Airfield. Solar data beyond 1991 is

unavailable at this site because the project for which the data was collected has ended. For the updated model validation used here, solar data was obtained from 1985 through 09/30/2008 from the Madras Agrimet weather station. Redmond solar data from 1985 to 1990 was linearly regressed against 1985 to 1990 Madras Agrimet data. The data are well correlated with a correlation coefficient of 0.95 and a coefficient of determination of 0.91 at the 0.05 level of significance. Consequently, values for the Redmond Roberts Airfield were created via this regression equation from January 1991 to May 2003. In the relatively few instances where Madras solar data was missing for certain dates, values generated from Boyd's (1996) regression equation were used:

$$\begin{aligned} solrad = & (-9.75643 * rtmin) + (5.782812 * rtmax) + (4.280205 * ptmin) \\ & + (6.745874 * ptmax) - 225.3845 \end{aligned} \quad (3)$$

In which *solrad* is solar radiation (langleys/hr), *rtmin* and *rtmax* are Redmond daily minimum and maximum temperatures respectively, and *ptmin* and *ptmax* are Prineville daily minimum and maximum temperatures respectively. Beginning in 05/01/2003, solar data from Powell Butte near Redmond is available through the NNDC Climate Data Online database. The latitude of the two sites are 44.265 degrees and 44.2667 degrees north, close enough to warrant using the Powell Butte data through 2008.

Deep Percolation Model Updating and Validation

Before the updated DPM validation is discussed, it is important to review the methodology of the previous calibration of the model. Stream flow at the Madras stream gauge station was used as a target for model calibration because it measures all of the surface water leaving the upper Deschutes basin. In addition, this gauge is below the point where the Deschutes and Crooked Rivers have cut through the permeable part of the geologic section. As a result, nearly all groundwater discharges upstream of the station. The Madras stream gauge record, therefore, contains the sum of baseflow and runoff for the entire upper Deschutes basin. For model calibration, it is important to distinguish between the recharge and runoff components of streamflow in the model. Baseflow separation cannot be used because the Deschutes River and some of its tributaries are highly regulated. Boyd (1996) determined baseflow to be about 85% via low flow statistics. However, independent estimates by Gannett et al. (2003) are used in this study.

For model calibration, saturated vertical hydraulic conductivity, which determines the partitioning of excess soil moisture between surface runoff and groundwater recharge was adjusted for each of the 10 hydrologic soil types through successive runs to meet target values for surface runoff for the basin and sub-basins (Boyd, 1996). After target values were achieved for subbasins, it was determined that the sum of simulated runoff and recharge values did not meet the target value for the entire basin. It was theorized that precipitation values were too low at high elevations. This was compensated for by

increasing PRISM model high elevation precipitation (Boyd, 1996). An additional problem acknowledged by Boyd (1996) is the consumptive use (evaporative loss) of irrigation waters in the basin. The upper Deschutes DPM does not simulate irrigation inputs and so cannot account for this secondary loss. In effect, the model's budget calculations are for a natural system. This must be accounted for in model validation.

The validation method used here is based on streamflow at the Madras gauge, but factors in boundary conditions and deviations from the natural system. Boyd's thesis was part of a comprehensive groundwater study which was completed several years after his thesis was published. An improved understanding of the system now exists although monthly time series data for many hydrologic fluxes are still unavailable. This means that a rigorous validation with statistical analyses is not currently possible although graphical comparisons can be made.

The evaluation of the DPM is based on the comparison between simulated runoff and recharge with estimates of runoff and recharge at the Madras gauge. It has been estimated that stream flow at the Madras gauge, river mile 100, is approximately 91% baseflow which is a reasonable proxy for groundwater recharge in the upper basin (Gannett et al., 2003). In-place recharge calculated by the DPM cannot be compared to the stream gage record due to the complex connections between surface water and groundwater along stream networks, irrigation canals and irrigated fields. Applied irrigation water, irrigation canal leakage, stream leakage, reservoir leakage, and drainage wells in urban areas all alter the percentage of total recharge in the basin. This artificial

recharge is not simulated by the DPM but shows up in the streamflow record. Additionally, consumptive use of irrigation water which is lost to evaporation affects the volumetric flow-rate of the Deschutes River. Mainly the artificial recharge from canal leakage and irrigation of crops has perturbed the percentages of recharge and runoff from the state of the natural system at the stream gauge near Madras. However, the stream gauge near Culver, 21 river miles south of the Madras Gauge, is generally unaffected by artificial recharge. The proportion of groundwater discharge at this location is 81% (Gannett et al., 2003). This is reasonable indicative of the natural system; in fact, the proportion of in place recharge as calculated by the DPM is likely to be less than the 81% at the Culver gauge due to secondary recharge from high-elevation stream losses (Marshall W. Gannett, U.S. Geological Survey, personal communication, 2010). The percentage of baseflow at the Culver gauge is applied to the total volume at the Madras gauge data to represent the proportion and volume of in-place recharge of the natural system. Before this is done, adjustments must be made to boundary conditions and on-farm losses must be accounted.

In addition to recharge from precipitation, it has been estimated that approximately 850 cfs ($24.072 \text{ m}^3/\text{s}$) enter the groundwater system from interbasin flow (Gannett et al., 2001). About 800 cfs ($22.656 \text{ m}^3/\text{s}$) from this total flows into the Metolius River Drainage through the Cascade Range divide from the west and about 50 cfs ($1.416 \text{ m}^3/\text{s}$) flow into the southeastern portion of the basin from the Fort Rock Basin (Gannett et al., 2001). This flux, which originates outside the upper Deschutes Basin

must be subtracted from the Madras gauge record before comparison with DPM estimates. It was estimated that 350 cfs (9.912 m³/s) of diverted surface water was lost to agricultural consumptive use (Gannett et al., 2001). Using the 1994 figure as an estimate, the on-farm losses must be added back to the Madras gauge. Additionally, the only sizeable input of surface water crossing the eastern model boundary is from the Crooked River. Therefore, the annual mean stream flow from the Crooked River near Prineville stream gauge is subtracted from the annual mean stream flow of the Deschutes River near Madras for the 1962 through 2008 water years. After these calculations are performed, the stream gauge data may be compared to the DPM output (Figure 8).

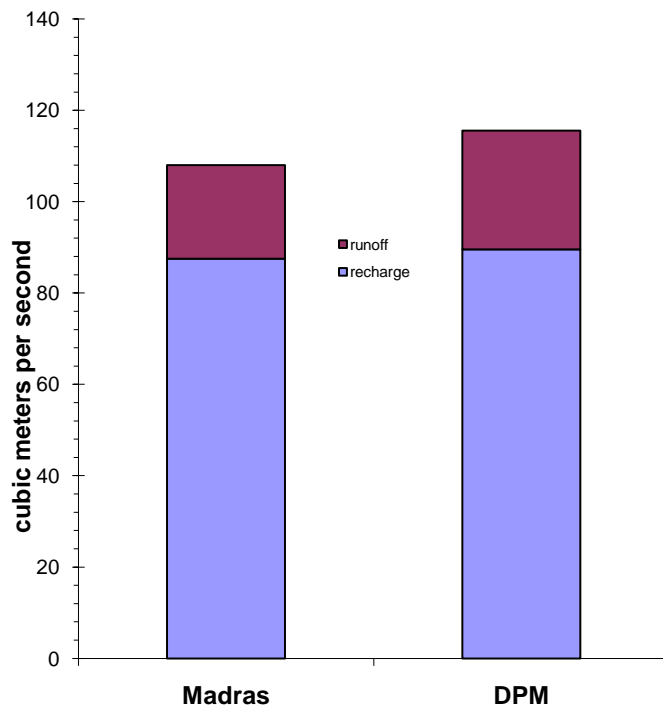


Figure 8. Graphical display of model validation results. The mean 1962-2008 period sum of annual recharge and runoff for the adjusted Madras stream gauge and the mean period DPM sum of annual recharge and runoff as well as the proportions of each.

The DPM results indicate that groundwater recharge, and hence baseflow, accounts for 77.5% of total basin yield while the amount of runoff is approximately 22.5%. This is 3.5% less recharge and 3.5% more runoff by volume than the observed record at Madras, adjusted as described. Assuming estimates for the observed record were handled correctly, the outcome of the validation exercise is favorable (Table 4).

Table 4. The mean 1962-2008 period recharge, runoff and sums calculated from annual means as well as the absolute difference between the adjusted observed record and the DPM calculations.

	Madras	DPM	Difference
	m ³ /s	m ³ /s	m ³ /s
recharge	87.5	89.6	2.1
runoff	20.5	26.0	5.5
sum	108.0	115.6	7.6

An annual mean hydrograph can also be constructed to compare the DPM sum of recharge and runoff with the adjusted annual observed stream gauge record near Madras (Figure 9). However, this is not the function of the DPM. It is rather the function of the groundwater flow model. What the hydrograph does illustrate, however, is the DPM's ability to capture the effects of the Pacific Decadal Oscillation (PDO) using the same temperature and precipitation forcings in which it is seen in the observed record. To make this comparison, DPM annual recharge data must first be smoothed. This is because recharge pulses diffuse as they travel from the Cascades to discharge regions in the center of the basin. To simulate this diffusion, a simple five year running average is employed which is fairly consistent with the observed attenuation and delay of recharge pulses in wells across the basin (see fig. 32 of Gannet, et al., 2001). Consequently, the DPM annual sums of recharge and runoff can only be compared to the adjusted observed sum of baseflow and runoff from 1966 to 2008 (Figure 9).

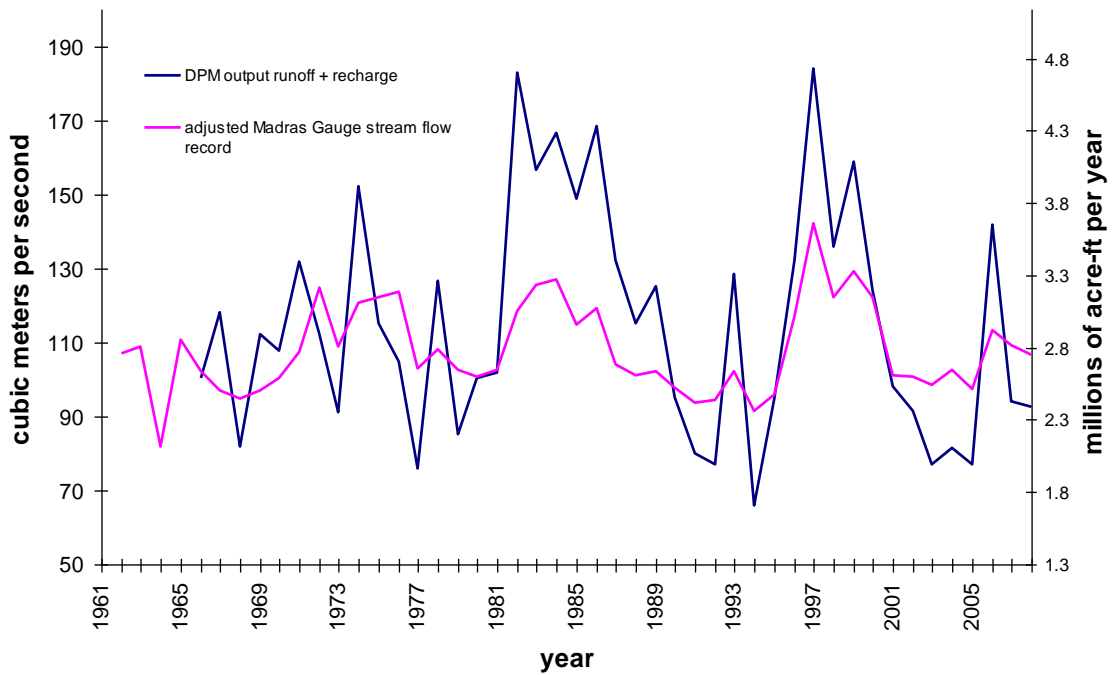


Figure 9. Annual mean hydrograph showing streamflow, simulated recharge + runoff. A five year moving average has been employed on the simulated recharge annual mean data.

Downscaled General Circulation Model Climate Data

GCM climate data was available for the period from 1961-2099 downscaled to a 1/16th degree grid and disaggregated to a daily time step. The nearest grid centroids of the downscaled GCM data received were for representing time series for future precipitation and temperatures at climate stations. Downscaled GCM grid points were selected by calculating and comparing the monthly means of precipitation from the four nearest centroids to each weather station and comparing them to the longest period of stationary record for the weather station. In this way, the centroid with the closest

precipitation match to the historical record for the majority of models was selected to represent the precipitation and temperature at weather stations into the 21st century.

(Appendix B) contains the selection results of the centroid matches.

Downscaled GCM data for solar radiation does not currently exist for the basin. Instead, an equation relating air-temperature to daily solar radiation, R_s (W m^{-2}) is used (Allen, 1997; Hargreaves and Samani, 1982). The equation has the form:

$$R_s = K_r (T_{\max} - T_{\min})^{0.5} R_a \quad (4)$$

Where T_{\max} and T_{\min} are mean daily maximum and minimum air temperature in degrees Celsius, K_r is an empirical coefficient, and R_a is extraterrestrial radiation (Allen, 1996):

$$R_a = \frac{G_{sc}}{\pi} d_r (\omega_s \sin \varphi \sin \delta + \cos \varphi \cos \delta \sin \omega_s) \quad (5)$$

In which R_a is daily average extraterrestrial radiation (W m^{-2}), G_{sc} is the solar constant (1367 W m^{-2}), d_r is the relative distance factor from Earth to Sun, δ is solar declination in radians, φ is latitude in radians (positive for northern hemisphere and negative for southern), and ω_s is the sunset hour angle in radians.

The sunset hour angle is calculated following:

$$\omega_s = \frac{\pi}{2} - \arctan \left[\frac{-\tan \varphi \tan \delta}{(1 - \tan^2 \varphi \tan^2 \delta)^{0.5}} \right] \quad (5)$$

The relative distance factor from the Earth to the Sun and solar declination are:

$$d_r = 1 + 0.33 \cos \left(\frac{2\pi}{365} J \right) \quad (6)$$

and

$$\delta = 0.409 \sin\left(\frac{2\pi}{365} J - 1.39\right) \quad (7)$$

where J is the number of day in year. The coefficient K_r in equation (4) is empirically derived. By comparing calculated solar radiation data to observed radiation data at the Redmond weather station and looking for the closest one to one relationship, K_r was determined to be 0.147. Regressing the calculated solar radiation with $K_r = 0.147$ against the observed solar radiation from 1961 to 1991 shows a strong correlation, coefficient of determination ≈ 0.98 . The calculated daily solar radiation values are then converted to Langley's per day for use in the model.

Procedure

After the DPM is run for all ensemble members and both emission scenarios, the results for each emission scenario are averaged in each climate period. A weighted average is used for the 2080s period because the PCM data only extends through 2098. For each climate period, mean monthly hydrographs of recharge and runoff are constructed. The mean seasonal total amounts of recharge and runoff are calculated by simply summing the mean monthly values of the included months for each time period (Table 5). A one-way Analysis of Variance (ANOVA) is then performed to see if there is

Table 5. Seasons through the year and the included months.

Season	Months		
Fall	September	October	November
Winter	December	January	February
Spring	March	April	May
Summer	June	July	August

any statistical difference between climate periods for a particular season. This is followed by Levene's Tests checking for heteroscedacity assumptions that are important to multiple comparison procedures. If variances between one or more groups are determined to be heterogeneous, Scheefe's multiple comparison procedure at the 0.05 level of significance is used to determine which climate periods are statistically different for each season. Otherwise Tukey's Honestly Significant Difference multiple comparison procedure at the 0.05 level of significance is used to determine which climate periods are statistically different for each season (Hochberg and Tamhane, 1987). This statistical procedure is also used for all mean monthly hydrographs presented, and error bars convey the results of testing. For a particular month, if the error bars between climate periods are disjoint, there is a statistical difference between means.

Spatial distribution maps of recharge and runoff are then created for each season's climate period. Additionally, percent changes from the 1980s base period maps are created to show the evolution of changes in the spatial distribution of precipitation and recharge throughout the 21st century.

The DPM recharge and phreatic plant evapotranspiration outputs throughout the entire simulation period are used as inputs for the groundwater flow model. The resulting output data is used to create mean monthly hydrographs displaying of baseflow for selected streams in the basin for each climate period.

RESULTS

Downscaled GCM Temperature and Precipitation as Interpolated by the DPM

Projected average annual temperatures averaged over the entire basin indicate net warming throughout the simulation period for all GCMs in both the A1B and B1 emission scenarios (Figure 10 & Figure 11). Both time series have a coefficient of determination of approximately 0.96. The magnitude is larger in the A1B scenario than in B1, and the ensemble mean annual average warming is 1.1° C and approximately 0.8° C, respectively for climate periods after the 1980s (Table 6).

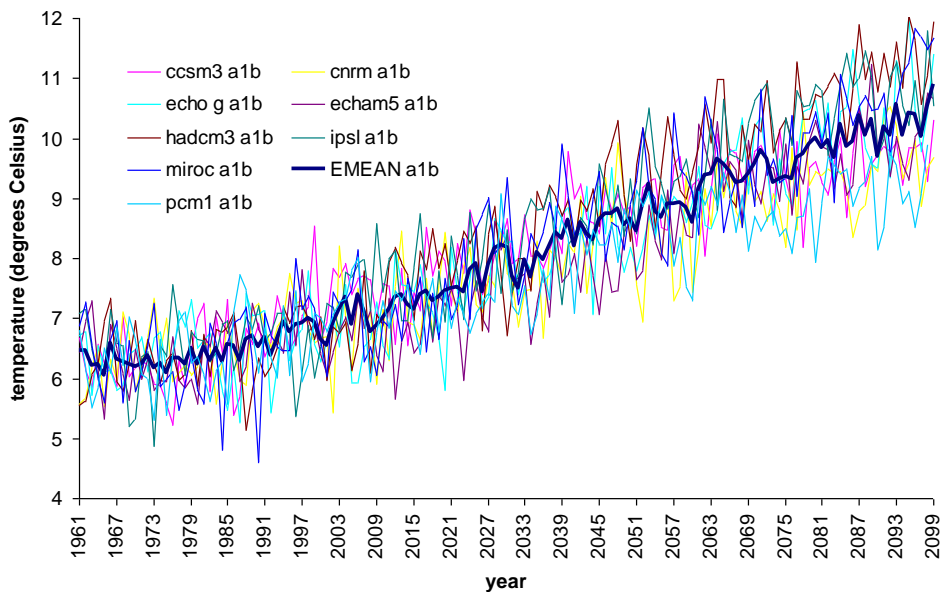


Figure 10. Mean annual temperatures averaged for the entire upper Deschutes basin as determined by the DPM driven by all GCMs used in the A1B emission scenario. The ensemble mean is shown as a heavy blue line.

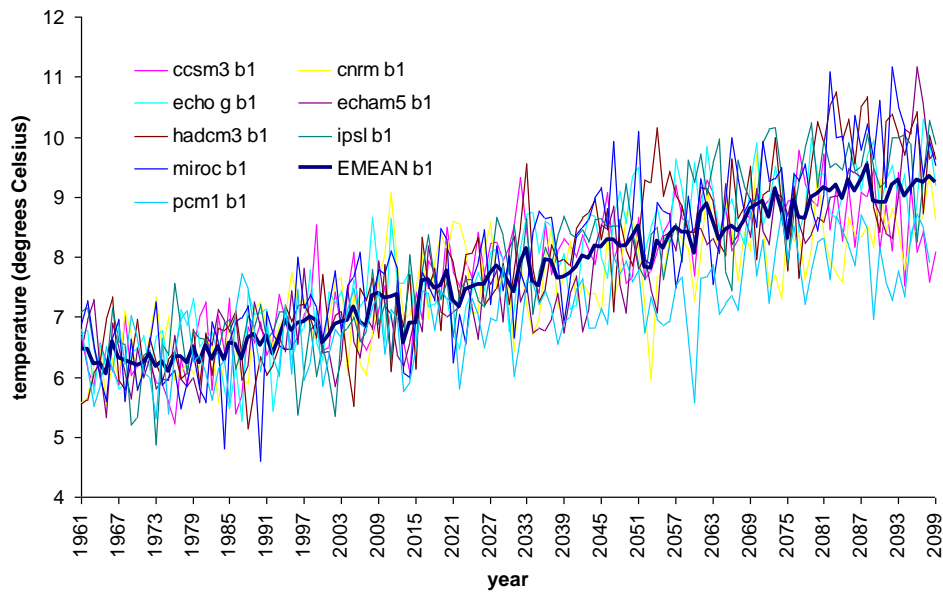


Figure 11. Mean annual temperatures averaged for the entire upper Deschutes basin as determined by the DPM driven by all GCMs used in the B1 emission scenario. The ensemble mean is shown as a heavy blue line.

Table 6. Ensemble mean changes in annual average temperature also averaged over the entire basin and total precipitation percent changes for three 30 year climate periods from the corresponding 1980s averages.

	B1		A1B	
	temperature	precipitation	temperature	precipitation
2020s	1.0±0.4° C	-0.1%	1.2±0.5° C	-2.4%
2050s	1.8±0.4° C	0.2%	2.4±0.5° C	0.2%
2080s	2.6±0.4° C	0.1%	3.4±0.5° C	1.0%

Over the entire simulation period, no annual mean trend in precipitation emerges over the basin for either the A1B or B1 scenario (Figure 12 & Figure 13). Also, statistical testing on mean annual precipitation between climate periods for both GHG

emission scenarios does not indicate any statistical significance to differences (Table 6). However, statistical testing performed on mean seasonal precipitation shows a statistical difference between all future climate periods and the 1980s climate period for the A1B scenario, and a statistical difference between the 2080s and the 1980s for the B1 scenario for the summer season only. The differences indicate small decreases in precipitation after the 1980s, however, these summer decreases are not driving the principal changes in the basin's hydrology.

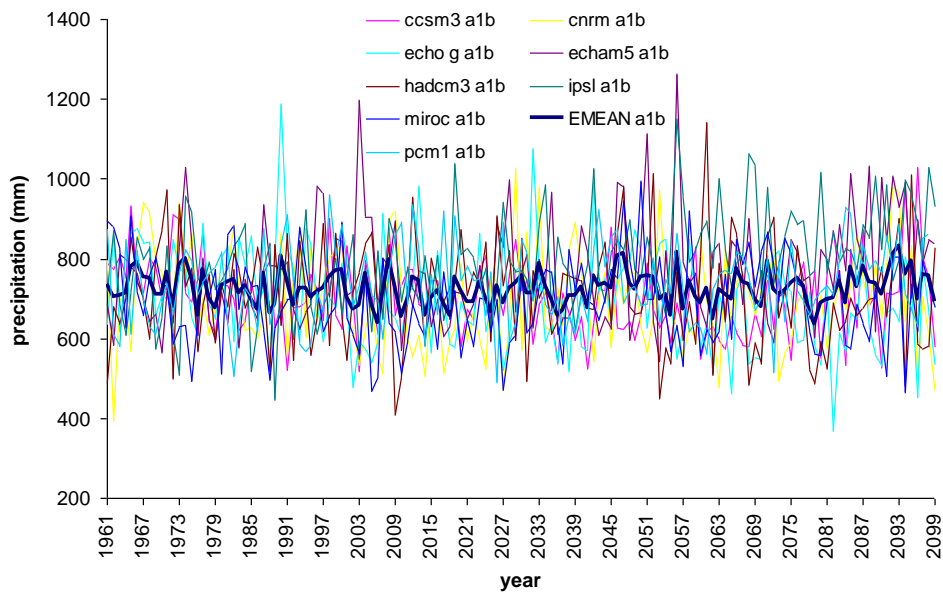


Figure 12. Cumulative yearly precipitation of all GCMs used in the A1B scenario. The ensemble mean is shown as a heavy blue line.

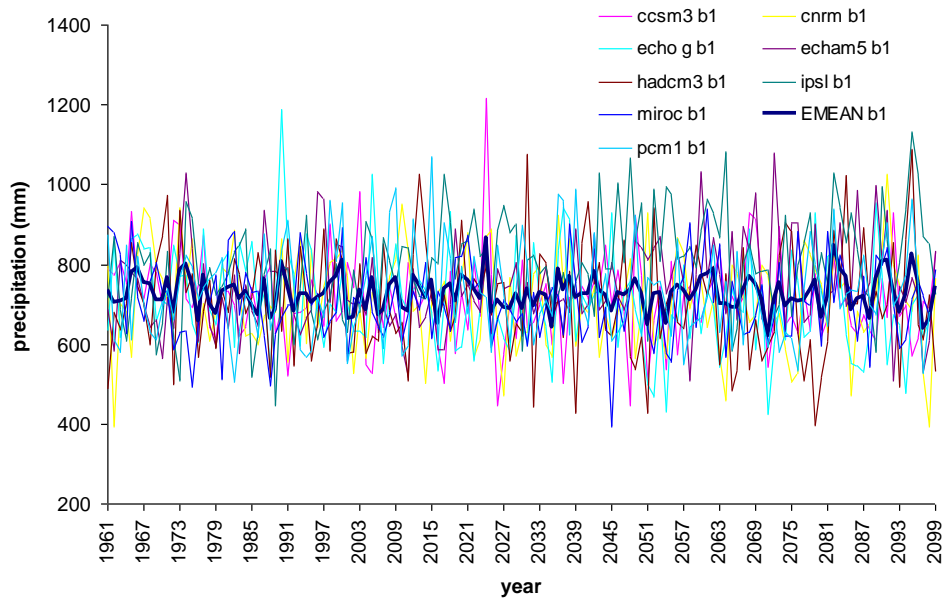


Figure 13. Cumulative yearly precipitation of all GCMs used in the B1 scenario. The ensemble mean is shown as a heavy blue line.

The trend in ensemble means of annual average temperature from the eight GCMs used in this study for both emission scenarios closely resembles the results of a regional study of future climate scenarios for the Pacific Northwest in which an ensemble of 20 GCMs was analyzed (Mote et al., 2008). The basin-wide observed mean temperature trend is statistically significant at any confidence level for both ensembles indicating that the trends are distinguishable from natural variability (Mote et al., 2008). The precipitation time series used here varies somewhat from Mote et al. (2008). No significant trend is indicated by the ensemble means of total yearly precipitation in this study suggesting that future precipitation does not stand apart from natural variability through the 21st century. Studies of the entire Pacific Northwest region find a similar pattern until late in the 21st century (Mote et al., 2008).

Deep Percolation Model

Forecasts of mean monthly values averaged basin-wide for the 1980s ensemble mean DPM hydrologic budget variables agree well with the DPM budget variables using historical temperature and precipitation observations (Appendix C). This is to be expected as the BCSD downscaling method is designed to capture the statistics of primary fields using historical observations. DPM ensemble mean forecasts of recharge and runoff quantities for the 2020s, 2050s, and 2080s, can thus be compared meaningfully to the 1980s ensemble mean baseline values.

Projected changes in the hydrologic budget of the upper Deschutes Basin are determined primarily by the model's sensitivity to warming. It should be noted that the standard practice, followed, of determining solar radiation using modeled temperature introduces an unknown error if the present-day empirical relationship between daily temperature range and insolation does not hold in the future. While total precipitation, averaged basin-wide, changes little over the study period, the annual cycle of snow accumulation and melt is modified by the change in temperature, which in turn affects the hydrologic cycle. For all future time periods at the 0.05 level of significance, there are no statistically significant differences in the modeled future mean annual cumulative amounts of recharge and runoff from the 1980s baseline period for the B1 scenario while the only statistical significance is between the 2020s and 2080s for the A1B scenario.

However, the timing of recharge and runoff progressively shift from spring to winter as time progresses into the 21st century.

Basin-wide Averages

The basin-wide averaged mean monthly recharge shifts from a spring dominated pattern to a situation in which winter recharge is also significant in both the A1B and B1 scenarios (Figure 14 and Figure 15). The shift becomes more pronounced as the time periods progress into the 21st century although in the 2080s there is still a spring recharge pulse related to the melting of diminished mountain snowpack.

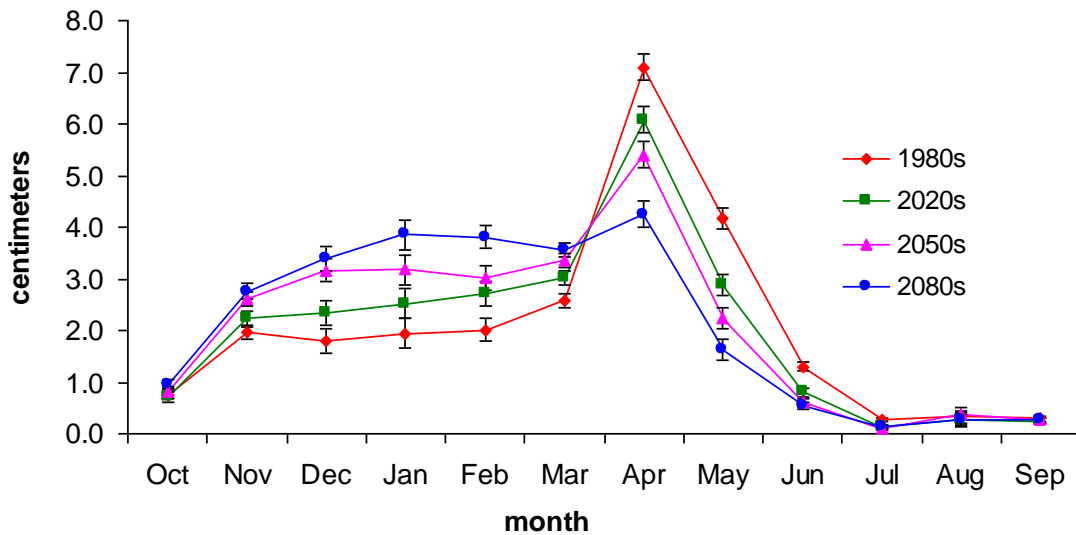


Figure 14. Mean monthly recharge for the A1B scenario averaged basin-wide for the four climate periods. Disjoint error bars between climate periods for a month indicate statistically significant differences (95% confidence) for that month.

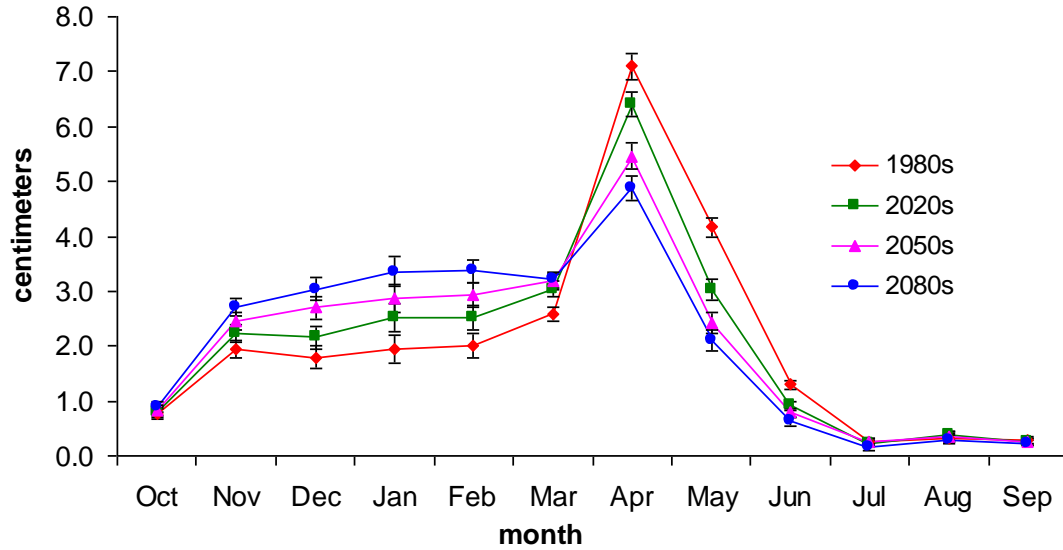


Figure 15. Mean monthly recharge for the B1 scenario averaged basin-wide for the four climate periods. Disjoint error bars between climate periods for a month indicate statistically significant differences (95% confidence) for that month.

Confirming what visual inspection of model recharge output suggests, statistical testing performed at the 0.05 level of significance on mean seasonal recharge indicates that the differences between means for all climate periods in both seasons are statistically significant for both emission scenarios (Table 7 and Table 8).

Table 7. Multiple comparison procedure results for recharge in the A1B scenario at the 0.05 level of significance. A “D” in a cell indicates that the difference between the row and column time period is statistically significant.

	Winter				Spring				
	1980s	2020s	2050s	2080s	1980s	2020s	2050s	2080s	
1980s		D	D	D	1980s		D	D	D
2020s	D		D	D	2020s	D		D	D
2050s	D	D		D	2050s	D	D		D
2080s	D	D	D		2080s	D	D	D	

Table 8. Multiple comparison procedure results for recharge in the B1 scenario at the 0.05 level of significance. A “D” in a cell indicates that the difference between the row and column time period is statistically significant.

	Winter					Spring			
	1980s	2020s	2050s	2080s		1980s	2020s	2050s	2080s
1980s		D	D	D	1980s		D	D	D
2020s	D		D	D	2020s	D		D	D
2050s	D	D		D	2050s	D	D		D
2080s	D	D	D		2080s	D	D	D	

Shifts in recharge for DPM ensembles driven with both emission scenarios have the same timing which can be seen by comparing Figure 14 to Figure 15. The difference between the two emission scenarios is the magnitude of the shift that occurs. When the DPM is driven by the A1B scenario, volumetrically greater shifts in the seasonal timing occur. This is related to the greater A1B warming. However, the fact that all time periods are statistically different from each other for both emission scenarios indicates that the rate of change of the seasonal recharge shift is similar for both scenarios.

Although volumetrically less than recharge, the mean monthly values of runoff suggest a similar shift from mainly spring runoff to decreased spring runoff and increased winter runoff for both emission scenarios (Figure 16 and Figure 17). While statistically significant differences in runoff between periods do exist in the A1B scenario for the month of March, as indicated by disjoint error bars, the values themselves are not very different and tend to converge toward a common range for this month for both emission

scenarios (Figure 16 and Figure 17). This is because snowpack is no longer increasing in the month of March for any climate period—temperatures and actual soil evaporation are increasing across the basin where there has not been or is no longer snowpack. In short, lower mid-elevation to mid-elevation soils in the basin with soil properties which tend to generate larger amounts of runoff when saturated are no longer saturated in the month of March. The hydrologic properties of soils responsible for the partitioning of water between recharge and runoff will be discussed in a following section.

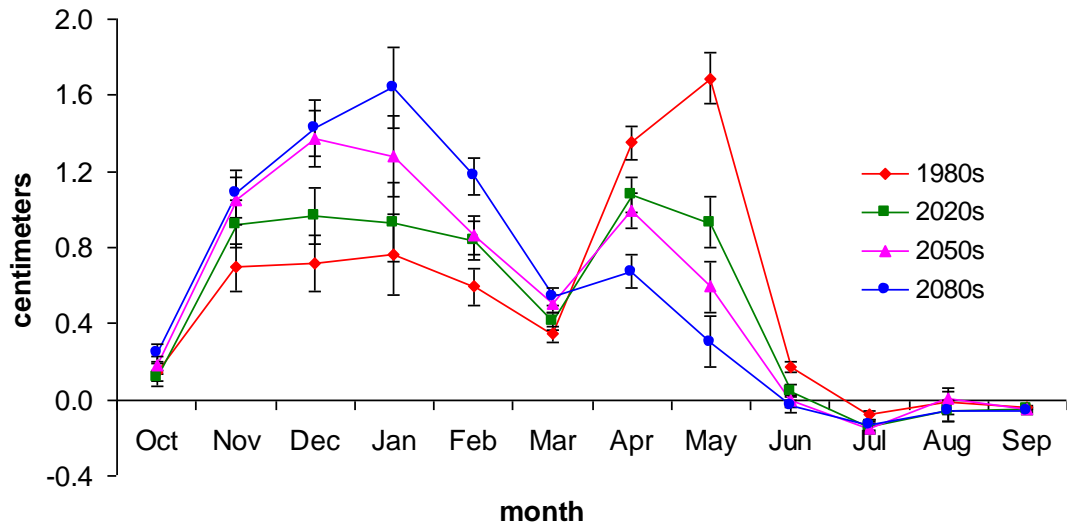


Figure 16. Mean monthly runoff for the A1B scenario averaged basin-wide suggesting a seasonal shift in runoff. Disjoint error bars between climate periods for a month indicate statistically significant differences (95% confidence) for that month.

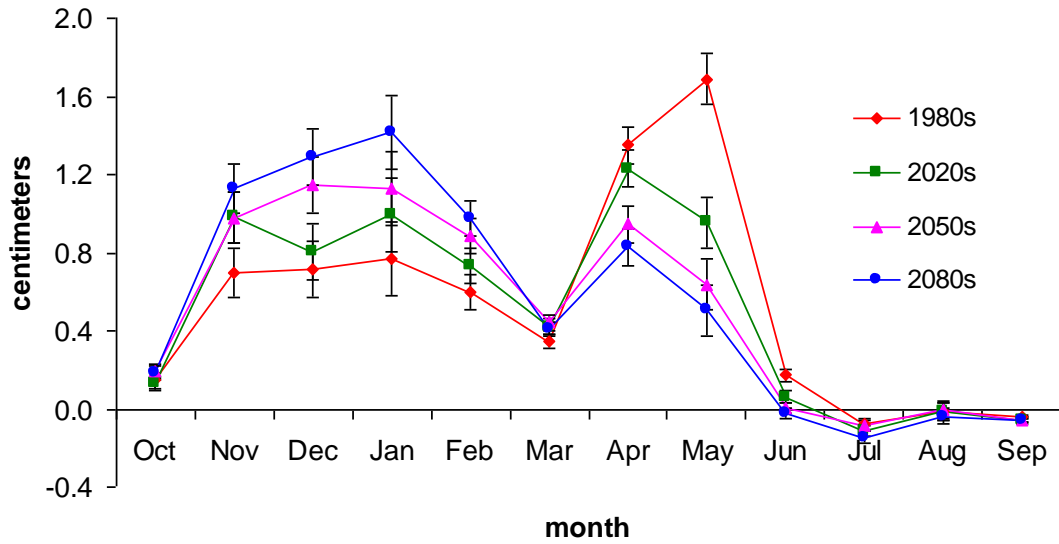


Figure 17. Mean monthly runoff for the B1 scenario averaged basin-wide suggesting a shift through the time periods from spring to winter runoff. Disjoint error bars between climate periods for a month indicate statistically significant differences (95% confidence) for that month.

Statistical testing has been performed to determine if the seasonal shifts from period to period suggested by the DPM basin-wide average mean monthly hydrographs are statistically significant (Table 9 & Table 10).

Table 9. Multiple comparison procedure results for runoff in the A1B scenario at the 0.05 level of significance.

	Winter				Spring			
	1980s	2020s	2050s	2080s	1980s	2020s	2050s	2080s
1980s	■	D	D	D	1980s	■	D	D
2020s	D	■	D	D	2020s	D	■	D
2050s	D	D	■	D	2050s	D	D	■
2080s	D	D	D	■	2080s	D	D	D

Table 10. Multiple comparison procedure results for runoff in the B1 scenario at the 0.05 level of significance.

	Winter				Spring				
	1980s	2020s	2050s	2080s	1980s	2020s	2050s	2080s	
1980s			D	D	1980s		D	D	D
2020s			D	D	2020s	D		D	D
2050s	D	D			2050s	D	D		
2080s	D	D			2080s	D	D		

For the A1B scenario, the DPM ensemble differences in mean totals for all periods are statistically significant for winter runoff, and the only periods that do not differ in a statistically significant way for spring runoff are the 2020s and 2050s (Table 9). Runoff hydrographs indicate that the shift in B1 runoff is similar to the shift in A1B runoff but with lesser magnitude after mid-century. For the B1 emission scenario, changes in mean winter runoff become statistically significant after the 2020s, but no other significant difference is detected through the latter part of the century. Changes in mean spring runoff are statistically significant from the 1980s to the 2020s and from the 2020s to the 2050s, but no significance is detected between the 2050s and 2080s mean totals. It is apparent with the B1 emission scenario that seasonal shifts in runoff do occur, but at a slower rate than the A1B emission scenario.

The winter and spring basin-wide average trends are of opposite sign under both emission scenarios. Differences in basin-wide average winter mean seasonal totals relative to the 1980s base period tend to increase as periods progress into the future while differences in basin-wide average spring mean seasonal totals tend to decrease (Table

11). If a difference between two consecutive future periods is not statistically significant, the difference from the 1980s for the more future period is not considered for basin-wide averages.

Table 11. Differences in basin-wide averaged recharge and runoff in centimeters per year from the 1980s base period; n/a indicates that the period is not statistically different from the preceding period.

	winter			spring		
	2020s	2050s	2080s	2020s	2050s	2080s
A1B recharge	1.8±1.8	3.6±1.9	5.3±2.1	-1.9±1.9	2.9±1.9	-4.4±1.8
B1 recharge	1.5±1.8	2.7±2	4.0±1.9	-1.4±1.7	-2.8±1.8	-3.7±1.9
A1B runoff	0.7±1.0	1.4±1.1	2.2±1.4	-1.0±0.9	n/a	-1.9±0.8
B1 runoff	n/a	1.1±1.1	n/a	-0.8±0.9	-1.4±0.8	n/a

Changes in Spatial Distribution of Recharge and Runoff

Changes in the spatial distribution of recharge and runoff are important for the groundwater flow model. Evaluating spatial patterns provides additional insights into the hydrologic response to climate change not revealed by basin-wide averages. Like the basin-wide average results, spatial changes are considered relative to the 1980s baseline period. Here, winter and spring seasonal changes in recharge and runoff relative to the 1980s are analyzed using the spatial distribution of in-place recharge and runoff in future climate periods.

Patterns of Recharge and Runoff in the 1980s

Orographic precipitation is the ultimate source of runoff and in-place recharge in the basin. As a result, the areas generating recharge and runoff overlap somewhat; although, the extent of the recharge zone is generally the greater of the two. Because most runoff and recharge are generated at higher elevations, the discussion here focuses on spatial changes between climate periods at higher elevations; namely the northwestern portion of the basin, the Three Sisters Vicinity including Broken Top, the area south of the Three Sisters near the Cascades including uplands near the southern boundary of the basin, and Newberry Volcano in the southeast portion of the basin (Figure 18). Hereafter, these areas of the basin will be referred to as the North Cascades Region, Three Sisters Region, South Cascades Region, and Newberry Region respectively. In the following paragraphs, DPM recharge and runoff spatial results are expressed in units of length representing the depth of water in a grid cell or series of cells.

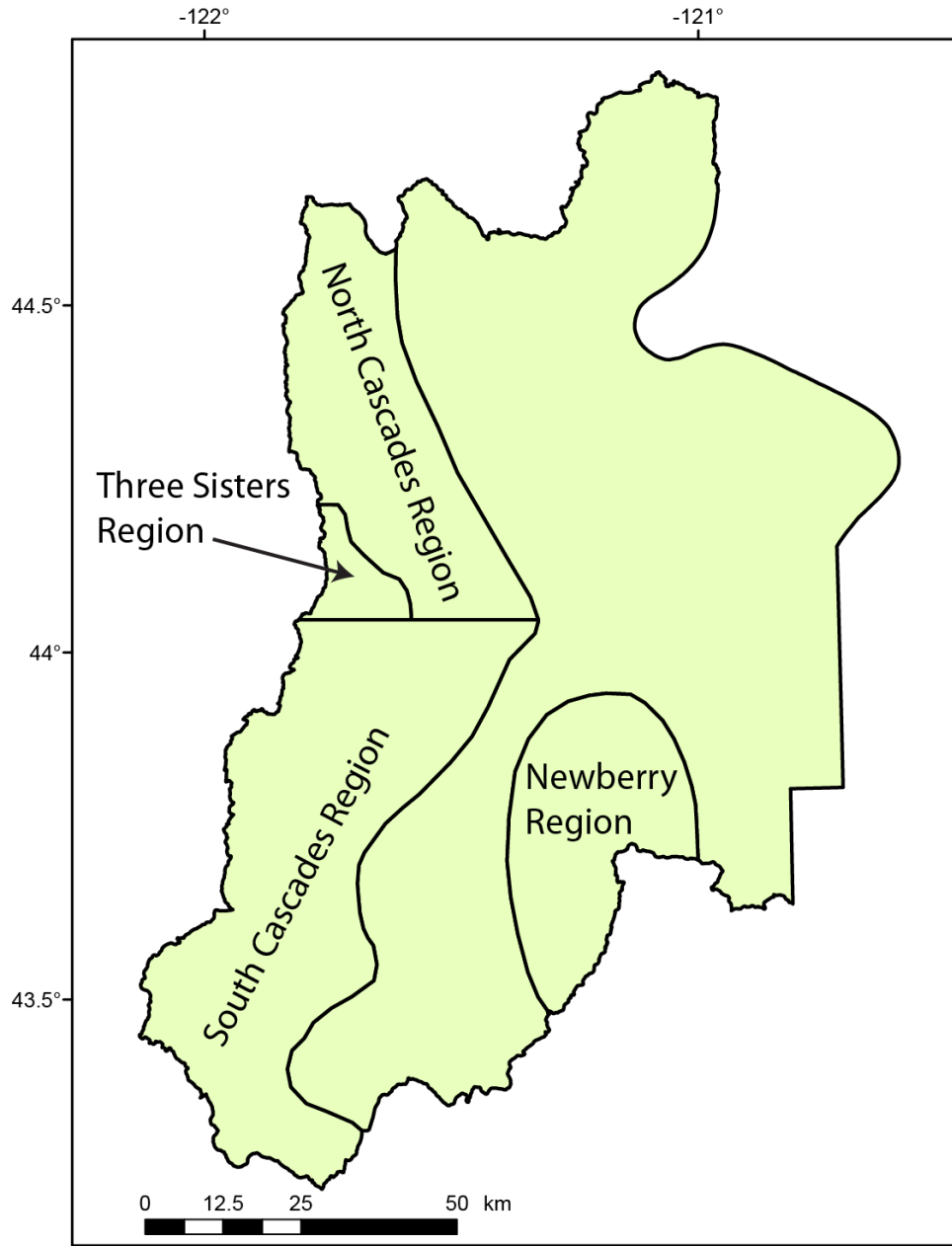


Figure 18. Regions of interest for spatial distributions of recharge and runoff.

Winter in-place recharge for the 1980s commonly ranges from 10 to 37 cm in and near the Cascades with locally heavier amounts of up to approximately 41cm near the

Cascade crest in the North Cascades Region (Figure 19A). Farther east in the Newberry Region, recharge on the volcano is more subdued with a range from about 3 to 7 cm on the southern slopes with locally heavier amounts in the caldera and interspersed on the northern and southern flanks (Figure 19A).

Spring recharge quantities are significantly higher than winter with 20 cm to 63 cm common in the South Cascades Region and amounts exceeding 70 cm near the crest (Figure 19B). In the Three Sisters Region recharge generally exceeds 160 cm with several grid cells ranging up to approximately 196 cm (Figure 19B). In the North Cascades region, near the crest, recharge in excess of 100 cm is found but amounts rapidly decrease with decreasing elevation (Figure 19B). Spring recharge is about 40 cm at the crest of Newberry Volcano and decreases to about 10 cm on the lower slopes in the Newberry Region (Figure 19B).

Winter runoff ranges from about 2 cm to about 45 cm in the regions adjacent to the Cascades with the largest amounts of runoff occurring in the upper elevations of the South Cascades Region (Figure 19C). Minimal runoff occurs in the Newberry Region during the winter season (Figure 19C). Spring runoff is largest around the border of the Three Sisters and South Cascades Regions with some cells exceeding 100 cm (Figure 19D). Elsewhere throughout these two regions, spring runoff amounts ranging from 10 to 37 cm are common in the mid to upper elevations. Few cells in the North Cascades

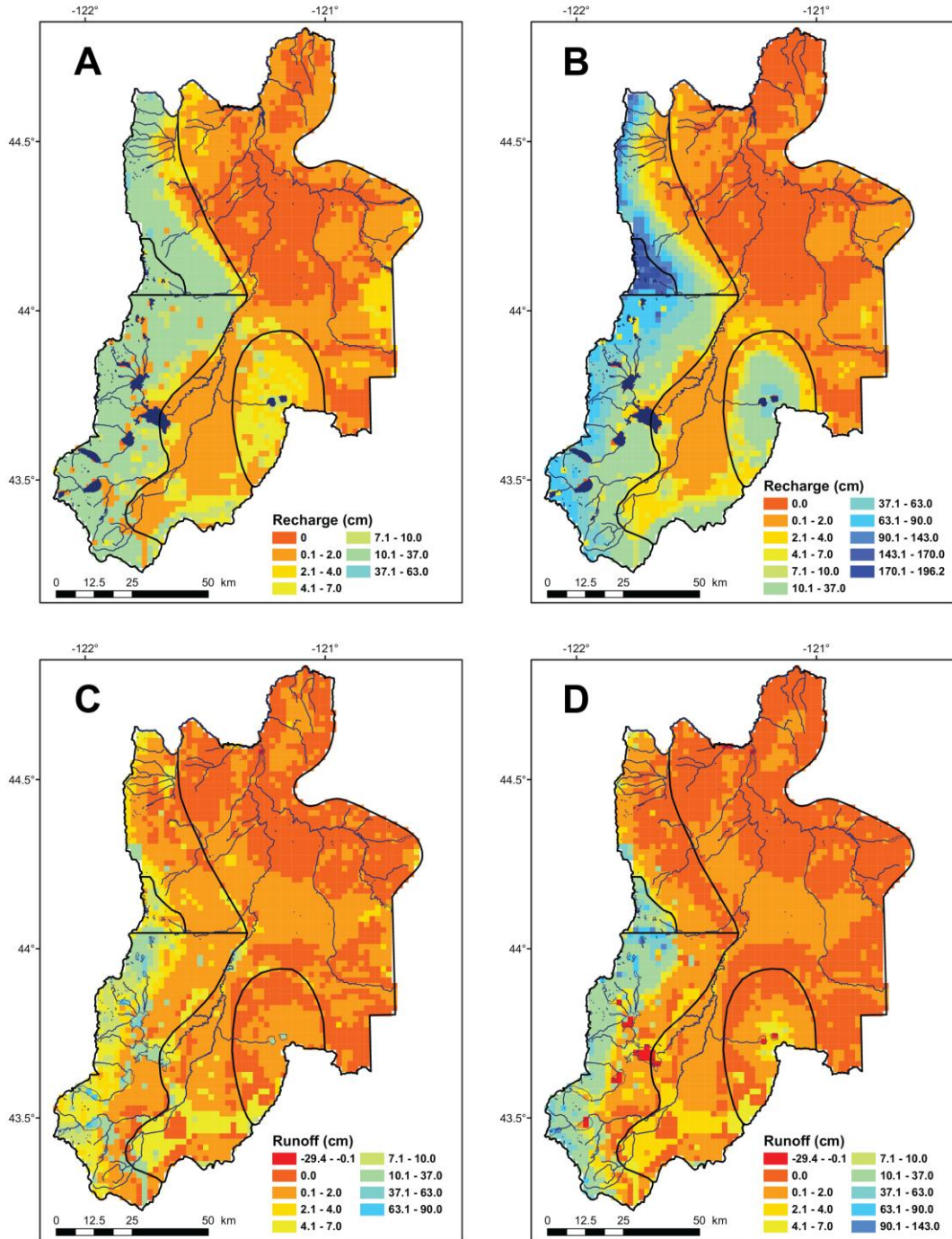


Figure 19. (A) The spatial distribution of mean winter recharge for the 1980s. (B) 1980s spatial distribution of recharge for spring. (C) The spatial distribution of mean winter runoff for the 1980s. (D) The spatial distribution of spring runoff for the 1980s.

Region produce significant spring runoff, however, just north of the Three Sisters region runoff in a series of cells ranges from about 20 to 40 cm. Newberry experiences around 3 to 7 cm of spring runoff in higher elevation grid cells but amounts rapidly diminish with decreasing elevation, with the exception of the southernmost tip of this region (Figure 19D). The DPM produces negative runoff values in both winter and spring for few grid cells. These are cells with a land cover type designated as open (surface) water and negative values indicate that the total storage in the water body has been reduced (Vaccaro, 2007). Open water cells are assumed to have an outflow and the storage for these cells is calculated by comparing precipitation to evaporation (Vaccaro, 2007).

The climatic and geologic controls on the partitioning of water in the baseline period DPM simulations must be taken into consideration in order to fully understand the modeled response to climate change after the 1980s. This begins with the form and timing of precipitation.

For all climate periods and both emission scenarios, the DPM-calculated basin-wide average precipitation frequency and amounts are highest from November through January, and the majority of the precipitation occurs at elevations above approximately 4500 ft. Most of this water arrives as snow during winter months and is stored as snowpack during the 1980s baseline period. Recharge and runoff occur principally at higher elevations when rising air temperatures allow snowpack to melt into saturated soils (Figure 19A). Rising temperatures yield snowmelt by providing energy directly to melting and by causing rain on snow events at times during the spring. The meltwater

goes either into recharge or runoff depending primarily on the depth of snowpack, rate of snowpack melt, and the infiltration capacity of the substrate where the melt is occurring.

The DPM assumes infiltration capacity for a grid cell is equal to saturated vertical hydraulic conductivity (VKSAT) under unit gradient of the substrate when the soil is fully saturated (Vaccaro, 2007). Consequently, VKSAT (LT^{-1}) assigned to a grid cell affects the ratio of recharge to shallow subsurface runoff (Bauer and Vaccaro, 1987; Boyd, 1996; Vaccaro, 2007). The highest rates of infiltration, corresponding to the highest VKSAT cell values and leading to large values of recharge, occur in the High Cascades around in the Three Sisters Region and in the North Cascades Region along the crest (Figure 19B). These areas are also where the largest amounts of precipitation occur, along with the southwestern tip of the basin near Summit Lake.

Spatial variations in soil properties are the principal control on the partitioning of runoff and recharge for the basin in the spring. The Three Sisters Region and the upper elevations of the South Cascades Region generates more direct spring runoff than the North Cascades Region during the 1980s (Figure 19D). Greater amounts of runoff despite high VKSAT values in the High Cascades of the Three Sisters Region can be explained by a relatively high horizontal permeability soil property and the very large volume of the snowpack that occurs here. The situation is different for the western margin in the South Cascades Region, where VKSAT is lower. Here, when the soils are saturated by snowmelt, the lower VKSAT partitions a higher fraction of water to runoff.

21st Century

Changes in the spatial distribution and timing of recharge and runoff through the 21st century can be examined using means from the climate periods. Mean spring and winter absolute changes are compiled by subtracting the ensemble mean of a future climate period's season from the 1980s ensemble mean of the same season individually for model grid cells. Summary statistics for absolute change and percent change discussed in this section are for the regions of interest as described in the preceding section (Figure 18).

Because two different methods are used to calculate change, spatial maps of the two fields can be different (Appendix D-F). Similarly, summary statistics presented for absolute change are for the entire region of interest while summary statistics presented for percent changes are only for the shaded areas in each region (Appendix D-F). Also, although included in runoff spatial maps of absolute change, the changes in open water cells are left out of summary statistics for regions of interest because the dominant factors affecting hydrologic fluxes is different in these cells.

It is informative to visually represent a climate period's seasonal changes in recharge and runoff for a grid cell or a region in terms of the percent changes from the 1980s. However, because the amounts of recharge or runoff can vary greatly between winter and spring for a particular region during the baseline period, percent changes do not tell the whole story. It is important to consider the absolute change from the 1980s for a season to keep the volumetric changes of a region in perspective.

Hydrologic changes in the North Cascades Region during the 21st century are characterized by a dominant pattern of increasing winter recharge with greatest increases occurring in the highest elevations and decreasing spring recharge with greater percent changes occurring below the Cascade crest in both GHG emission scenarios (Appendix D-F). Winter changes in recharge for the 2020s A1B emission scenario in the North Cascades Region, about 1271 km², show percent increases of up to 66% along the Cascade margin grading down to about 4% to the eastern edge with a median change of about 18% (Table 12; Appendix D.1). The corresponding changes in spring recharge for this period and emission scenario show losses up to 7% along the Cascade crest with losses increasing up to 75% along the eastern edge of this region with a median loss of 22% (Table 12; Appendix D.2). Similarly the 2020s B1 scenario has winter gains ranging from 51% in the upper elevations decreasing to 5% as elevations decrease yielding a median gain of 13% (Table 13; Appendix D.3). Reductions in spring recharge for the 2020s B1 scenario range from 3% in the upper elevations to 49% in the foothills with a median loss of 19% (Table 13; Appendix D.4). In both GHG emission scenarios, spatial variation in recharge and runoff within the region increases as climate periods progress with increasing medians in spring and decreasing medians in winter (Table 12 and Table 13).

Table 12. Summary statistics of DPM spatial recharge changes for the A1B emission scenario in the northern region.

	period	median (cm)	max (cm)	min (cm)	median (%)	max (%)	min (%)
Winter	2020s	1.8	12.7	0.0	18	66	4
	2050s	3.6	23.8	0.0	36	121	14
	2080s	5.1	36.9	0.0	52	415	21
Spring	2020s	-1.9	0.0	-20.9	-22	-7	-75
	2050s	-2.5	0.0	-31.9	-29	-12	-77
	2080s	-3.6	0.0	-47.7	-41	-19	-91

Table 13. Summary statistics of DPM spatial recharge changes for the B1 emission scenario in the northern region.

	period	median (cm)	max (cm)	min (cm)	median (%)	max (%)	min (%)
Winter	2020s	1.3	8.7	0.0	13	51	5
	2050s	2.3	18.5	0.0	23	102	5
	2080s	4.2	26.7	0.0	41	134	16
Spring	2020s	-1.6	0.0	-14.4	-19	-3	-49
	2050s	-2.8	0.0	-29.2	-32	-9	-80
	2080s	-3.7	0.0	-38.0	-43	-14	-92

The North Cascade Region receives high precipitation near the Cascade crest but due to soil properties, this does not translate into large runoff volumes. Because of this, small seasonal changes can produce fairly large percent changes that sometimes appear anomalous in comparison to the rest of the basin or even adjacent cells (Appendix D-F). This is particularly true in the spring when gains instead of losses are seen in a few cells

around Santiam Pass, particularly in the A1B emission scenario (Appendix D-F). This is likely due to warmer temperatures increasing the rate of snowmelt and more rain on snow events in the early spring so that the infiltration capacity is exceeded in this high precipitation area. For the 2020s A1B scenario, changes in winter runoff in the North Cascades Region range from decreases of 32% to increases of 96% with the median change being an increase of 26% (Table 14; Appendix D.1). Spring 2020s A1B changes range from losses of 40% to gains of 33% with a regional median loss of only 19% (Table 14; Appendix D.2). In the 2050s A1B scenario, winter increases are higher than spring decreases, ranging from 20% to 210% with a median increase of 76% (Table 14; Appendix E.1). Spring changes for this climate period and scenario range from losses of 47% to gains of 74% with a median 17% increase (Table 14; Appendix E.2). The 2080s A1B winter and spring changes are similar but have larger amplitudes in both winter gains and spring losses (Table 14, Appendix F.1-2). For the B1 scenario, winter runoff increases by a smaller amount and at a slower rate than the A1B scenario (Table 15; Appendices D.1, E.1; F.1). However, B1 spring runoff losses are higher in volume than the A1B scenario for all time periods in this region (Table 15).

Table 14. Summary statistics of DPM spatial runoff changes for the A1B emission scenario in the northern region.

	period	median (cm)	max (cm)	min (cm)	median (%)	max (%)	min (%)
Winter	2020s	0.0	6.0	-0.6	26	96	-32
	2050s	0.2	10.7	0.0	76	210	20
	2080s	0.2	16.5	0.0	95	536	30
Spring	2020s	0.0	0.3	-14.5	-19	33	-40
	2050s	0.0	0.6	-19.0	-17	74	-47
	2080s	0.0	0.5	-28.9	-30	82	-78

Table 15. Summary statistics of DPM spatial runoff changes for the B1 emission scenario in the northern region.

	period	median (cm)	max (cm)	min (cm)	median (%)	max (%)	min (%)
Winter	2020s	0.0	4.0	-0.2	17	35	7
	2050s	0.1	8.8	0.0	61	170	9
	2080s	0.2	11.9	0.0	64	187	25
Spring	2020s	0.0	0.3	-11.9	-21	47	-33
	2050s	0.0	0.2	-20.1	-32	-8	-51
	2080s	0.0	0.4	-24.5	-40	31	-67

The Three Sisters Region, an area of prominent stratovolcanos including Broken Top, has the highest elevations and receives the greatest precipitation in the basin. Its area is only about 157 km² making it the smallest region considered. Changes in spatial patterns of recharge are unique in this region of the basin because there are many spring gains interspersed with losses on the flanks throughout the region in all climate periods and in both GHG emission scenarios. This results in small net gains in spring recharge or minor losses. Winter recharge changes tend to follow the same pattern as the rest of the

recharge zone in the basin. 2020s A1B winter recharge increases range from 35% to 93% with a median of 55% (Table 16, Appendix D.1). Changes in 2020s spring recharge for this scenario range from losses of 14% to gains of 14%, and the median is a loss of about 1% (Table 16, Appendix D.2). 2020s B1 recharge changes are similar, although there are gains in recharge in both winter and spring. However, winter gains range from 26% to 66% with a median of 44% while the spring changes range from 9% loss to 14% gains with the median being a gain of 2% (Table 17, Appendix D.4). Increases in winter recharge nearly double in the 2050s for this GHG emission scenario with a median increase of 105% (Table 17, Appendix E.1). For the 2050s A1B emission scenario, gains in recharge range from 68% to 222% with a median gain of 105% (Table 16; Appendix E.1). Corresponding spring losses for this GHG emission scenario and climate period are subdued with a median 4% loss and a range from losses of 21% to gains of 30% (Table 16; Appendix E.2). The B1 emission scenario has similar spatial distributions of recharge for the 2050s although the magnitudes of loss and gain are smaller (Table 17; Appendix E.3, E.4). For the 2080s, gains in A1B winter recharge increases range from 109% to 396% with a median gain of 174% (Table 16, Appendix F.1). Spring changes range from losses of 32% to gains of 42% with a median 12% loss (Table 16, Appendix F.2). Winter gains in recharge in the 2080s B1 emission scenario range from 75% to 258% with a median of 118%, and spring losses range from losses of 25% to gains of 32% with a median 6% loss being half the A1B emission scenario median change (Table 17, Appendix F.3, F.4).

Table 16. Summary statistics of DPM spatial recharge changes for the A1B emission scenario in the Three Sisters region.

	period	median	max	min	median	max	min
		(cm)	(cm)	(cm)	(%)	(%)	(%)
Winter	2020s	9.7	13.4	3.6	55	93	35
	2050s	18.3	24.5	8.7	105	222	68
	2080s	29.6	39.6	14.6	174	396	109
Spring	2020s	-0.9	19.0	-20.3	-1	14	-14
	2050s	-6.4	42.7	-31.4	-4	30	-21
	2080s	-17.1	57.5	-50.0	-12	42	-32

Table 17. Summary statistics of DPM spatial recharge changes for the B1 emission scenario in the Three Sisters region.

	period	median	max	min	median	max	min
		(cm)	(cm)	(cm)	(%)	(%)	(%)
Winter	2020s	7.5	9.4	2.6	44	66	26
	2050s	15.1	19.7	5.5	88	141	54
	2080s	20.0	27.5	10.1	118	258	75
Spring	2020s	3.3	20.2	-13.4	2	14	-9
	2050s	-4.0	31.9	-27.9	-2	23	-18
	2080s	-9.2	44.1	-38.0	-6	32	-25

The Three Sisters Region exhibits relatively large gains in winter runoff and either small spring gains or minimal losses in spring runoff. Median percent changes show that winter runoff is increasing but at a fairly constant rate between climate periods in the A1B scenario (Table 18; Appendix D.1, E.1, F.1). A median 7% spring gain in runoff occurs in the A1B 2020s, which decreases to a 9% median loss in the 2050s (Table 18, Appendix D.2, E.2). The median change is a loss in spring runoff which doubles in

the 2080s A1B emission scenario to 18% (Table 18, Appendix F.2). The B1 scenario winter runoff is similar to its A1B counterpart except that the magnitude of increases is smaller (Table 19, Appendix D-F). However, median changes in the B1 scenario spring never become losses, although gains are minimal by the 2080s (Table 19).

Table 18. Summary statistics of DPM spatial runoff changes for the A1B emission scenario in the Three Sisters region.

	period	median	max	min	median	max	min
		(cm)	(cm)	(cm)	(%)	(%)	(%)
Winter	2020s	4.4	9.7	0.9	86	215	48
	2050s	8.5	16.6	3.2	167	466	89
	2080s	12.3	25.9	4.3	247	721	127
Spring	2020s	1.1	9.6	-18.7	7	46	-27
	2050s	0.0	17.5	-26.1	-9	84	-35
	2080s	-2.9	15.9	-41.1	-18	110	-49

Table 19. Summary statistics of DPM spatial runoff changes for the B1 emission scenario in the Three Sisters region.

	period	median	max	min	median	max	min
		(cm)	(cm)	(cm)	(%)	(%)	(%)
Winter	2020s	1.9	5.4	0.4	45	99	22
	2050s	5.5	13.5	1.1	126	280	63
	2080s	8.2	17.5	2.8	169	443	89
Spring	2020s	-0.1	8.8	-14.3	-1	29	-27
	2050s	-0.3	14.5	-25.7	-6	61	-38
	2080s	-0.3	16.7	-33.0	-5	100	-42

The South Cascade Region’s recharge zone is the largest considered, with an extent of about 2421 km². It extends from just south of the Three Sisters area along the

western side of the basin to the southern boundary of the basin. Winter 2020s A1B gains in recharge range from 9% to 100% with a median of 34% (Table 20; Appendix D.1). Spring changes in recharge for this period and GHG emission scenario range from losses of 53% to gains of 29% with a median loss of 18% (Table 20, Appendix D.2). The B1 emission scenario 2020s gains in winter recharge range from 8% to 73% with a median gain of 28% (Table 21; Appendix D.3). Spring losses range from decreases of 42% to increases of 31% with a median 15% loss (Table 21; Appendix D.4). The same pattern of winter gains with somewhat smaller spring losses for the 2050s and 2080s occurs in both emission scenarios in this area with the magnitudes of change being higher for the A1B scenario (Table 20; Table 21; Appendix E-F).

Table 20. Summary statistics of DPM spatial recharge changes for the A1B emission scenario in the southern region.

	period	median (cm)	max (cm)	min (cm)	median (%)	max (%)	min (%)
Winter	2020s	6.0	11.9	-0.1	34	100	9
	2050s	11.4	21.4	-0.1	65	209	26
	2080s	15.6	34.7	0.0	92	317	38
Spring	2020s	-4.7	2.5	-19.9	-18	29	-53
	2050s	-7.7	5.4	-29.3	-28	29	-68
	2080s	-11.2	4.5	-46.1	-41	37	-90

Table 21. Summary statistics of DPM spatial recharge changes for the B1 emission scenario in the southern region.

	period	median (cm)	max (cm)	min (cm)	median (%)	max (%)	min (%)
Winter	2020s	4.7	8.5	-0.1	28	73	8
	2050s	8.6	17.6	-0.1	50	151	17
	2080s	12.3	24.0	-0.1	71	225	31
Spring	2020s	-3.6	4.2	-13.9	-15	31	-42
	2050s	-7.3	4.7	-27.3	-28	33	-75
	2080s	-9.7	4.8	-36.1	-36	47	-84

Orographic precipitation and soil properties combine to produce large volumes of runoff per unit area in the South Cascades Region relative to other regions. Winter 2020s A1B changes in runoff range from a loss of 2% to 242% gains relative to the 1980s with a region-wide median 49% gain (Table 22; Appendix D.1). The corresponding region-wide reduction in spring runoff ranges from decreases of 73% to increases of 29% with a median 39% loss (Table 22; Appendix D.2). The B1 scenario 2020s winter increases range from 13% to 108% with a median gain of about 30%. Spring losses for this scenario range from decreases of 58% in the middle elevations to gains of 22% in the southern portion of the basin (Table 23; Appendix D.4). The region-wide median value shows spring decreases barely exceed winter gains for this emission scenario with its median 31% decrease (Table 23). Similar difference in magnitude between A1B and B1 scenarios is seen in winter runoff for the 2050s and 2080s in this region. However, the spring median is a loss which is slightly greater in the B1 emission scenario for the

2050s, although the magnitude of loss is greater for the 2080s spring (Table 22; Table 23; Appendix E-F).

Table 22. Summary statistics of DPM spatial runoff changes for the A1B emission scenario in the southern region.

	period	median	max	min	median	max	min
		(cm)	(cm)	(cm)	(%)	(%)	(%)
Winter	2020s	1.3	14.6	-0.9	49	242	-2
	2050s	3.0	27.9	0.0	92	468	2
	2080s	5.0	41.7	0.0	142	622	4
Spring	2020s	-2.2	7.9	-20.5	-39	29	-73
	2050s	-2.6	11.3	-30.5	-52	21	-99
	2080s	-3.3	6.3	-44.0	-71	12	-90

Table 23. Summary statistics of DPM spatial runoff changes for the B1 emission scenario in the southern region.

	period	median	max	min	median	max	min
		(cm)	(cm)	(cm)	(%)	(%)	(%)
Winter	2020s	0.8	10.3	-0.2	30	108	13
	2050s	2.3	22.0	0.0	76	355	30
	2080s	3.6	29.8	0.0	103	408	42
Spring	2020s	-1.6	7.7	-15.2	-31	22	-58
	2050s	-2.7	9.4	-29.2	-54	23	-86
	2080s	-3.2	7.7	-36.5	-63	28	-97

The Newberry Region, a broad shield volcano with a topographic expression of about 1370 meters to 2435 meters, encompasses about 963 km². Because Newberry volcano is in the lee of the Cascade Range, it receives less precipitation than the Cascade Range. Due to its elevation, however, it receives more precipitation than the surrounding

area and is a locus of groundwater recharge. For the A1B scenario, 2020s projected increases in winter recharge range from increases of 14% at the base to 223% at the rim of the caldera with a median gain of 61% (Table 24; Appendix D.1). Reductions in spring recharge range from 7% to 46% for this scenario in the 2020s with a median loss of 21% (Table 24, Appendix D.2). For the 2020s B1 scenario, increases in winter recharge and decreases in spring recharge are similar to the A1B scenario although with reduced magnitudes in both seasons (Table 25; Appendix D.3). The 2050s A1B increases in winter recharge range from 27% to 517% at the rim with a median gain of 136% (Table 24; Appendix E.1). B1 scenario 2050s increases in winter recharge range from 20% to 346% with a median increase of 101% (Table 25; Appendix E.3). The 2050s A1B reductions in spring recharge range from 60% to 10% with a median decrease of 28% (Table 24; Appendix E.2). However, in one of the few cases where B1 magnitudes are more extreme than A1B magnitudes, the 2050s B1 emission scenario reductions in recharge range from 69% to 11% with a median decrease of 34% (Table 24; Appendix E.4). Winter increases in recharge for the 2080s A1B scenario range from 38% on the northwest flank of the volcano to 842% near the caldera with a median increase of 204% (Table 24; Appendix F.1). Spring reductions in recharge for this emission scenario and climate period are lower than gains with a reduction range of 83% to 23% and a median reduction of 42% (Table 24; Appendix F.2). Winter increases and spring reductions for the 2080s B1 emission scenario are similar to A1B's but with smaller magnitude (Table 25; Appendix F.3, F.4).

Table 24. Summary statistics of DPM spatial recharge changes for the A1B emission scenario in the Newberry region.

	period	median (cm)	max (cm)	min (cm)	median (%)	max (%)	min (%)
Winter	2020s	2.1	4.7	0.0	61	223	14
	2050s	4.5	8.9	0.0	136	517	27
	2080s	6.4	14.1	0.0	204	842	38
Spring	2020s	-1.9	-0.1	-5.0	-21	-7	-46
	2050s	-2.7	0.0	-9.0	-28	-10	-60
	2080s	-4.0	-0.2	-13.9	-42	-23	-83

Table 25. Summary statistics of DPM spatial recharge changes for the B1 emission scenario in the Newberry region.

	period	median (cm)	max (cm)	min (cm)	median (%)	max (%)	min (%)
Winter	2020s	1.8	3.5	0.0	53	180	12
	2050s	3.3	7.1	0.0	101	346	20
	2080s	5.3	9.5	0.0	153	567	32
Spring	2020s	-1.4	-0.1	-3.9	-15	-4	-40
	2050s	-2.9	-0.2	-8.2	-34	-11	-69
	2080s	-3.8	-0.1	-10.2	-38	-16	-76

Relatively low annual precipitation results in relatively less runoff in the Newberry Region than in other regions discussed here. It is important to note that percent changes in runoff only encompass the small shaded areas of spatial maps (Appendix D-F). Due to the relatively small area under consideration, the results for this region will focus on median changes. The 2020s A1B emission scenario has a median increase in runoff of 82% (Table 26; Appendix D.1). Spring runoff resulting from the 2020s A1B scenario shows a median decrease in runoff of 38% (Table 26, Appendix

D.2). At 46%, The B1 2020s median winter increase in runoff is about half the A1B scenario's increase and most of the change is near the southern basin boundary (Table 27, Appendix D.3). 2020s B1 scenario reductions in spring runoff occur in and around the caldera with a median loss of 27% (Table 17; Appendix D.4). Gains in winter runoff resulting from the 2050s A1B scenario are more than double the 2020s A1B gains with a median increase of 167% (Table 26; Appendix E.1). Corresponding reductions in 2050s spring runoff under the A1B scenario have a median decrease of 48% (Table 26; Appendix E.2). Increases in winter runoff during the 2050s under the B1 scenario produce a median change of 110% (Table 27, Appendix E.3). Decreases in spring runoff under this emission scenario for the 2050s have a median of 51% (Table 27; Appendix E.4). The areal extent of percent change increases by the 2080s for both seasons, particularly in the A1B emission scenario (Appendix F). Median 2080s winter increases in runoff are 276% for the A1B scenario in this region (Table 26; Appendix F.1). The median loss is 63% in the 2080s A1B spring (Table 26; Appendix F.2). For the 2080s B1 scenario, the median winter increase in runoff is 183% while the median spring decreases is 54% (Table 27; Appendix F.3, F.4).

Table 26. Summary statistics of DPM spatial runoff changes for the A1B emission scenario in the Newberry region.

	period	median (cm)	max (cm)	min (cm)	median (%)	max (%)	min (%)
Winter	2020s	0.0	3.0	0.0	82	326	32
	2050s	0.0	6.2	0.0	167	642	79
	2080s	0.0	8.7	0.0	276	1087	87
Spring	2020s	0.0	0.0	-2.8	-38	-17	-85
	2050s	0.0	0.2	-3.6	-48	-16	-91
	2080s	0.0	0.0	-4.8	-63	-34	-91

Table 27. Summary statistics of DPM spatial recharge changes for the B1 emission scenario in the Newberry region.

	period	median (cm)	max (cm)	min (cm)	median (%)	max (%)	min (%)
Winter	2020s	0.0	2.6	0.0	46	84	33
	2050s	0.0	4.6	0.0	110	482	58
	2080s	0.0	7.1	0.0	183	696	74
Spring	2020s	0.0	0.0	-2.1	-27	-12	-57
	2050s	0.0	0.0	-3.6	-51	-27	-79
	2080s	0.0	0.0	-4.6	-54	-36	-84

Response of Groundwater Discharge to Projected Future Climate

The regional groundwater flow model of the upper Deschutes Basin by Gannett and Lite (2004) is used to evaluate changes in groundwater discharge to along selected stream reaches in response to future climate (Figure 20). Large volumes of groundwater discharge to streams in three main areas of the upper Deschutes Basin. These include the southern, uppermost portions of the basin within and near the Cascades; the Metolius

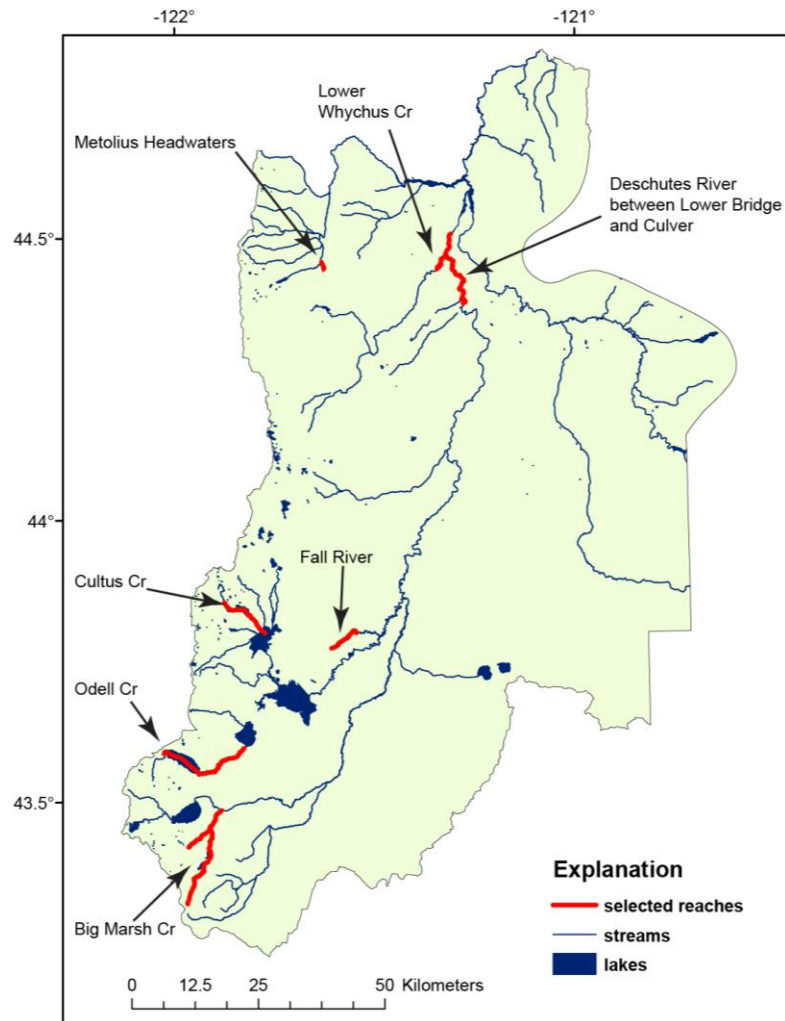


Figure 20. Locations of stream reaches investigated for changes in groundwater discharge from projected future climate.

sub-basin in the northwestern portion of the basin adjacent to the Cascades; and the area in and around the confluence of the Deschutes, Crooked, and Metolius rivers in the north-central portion of the basin (Gannett et al., 2001).

The largest seasonal variations of groundwater discharge, in the upper Deschutes Basin, are in the smaller streams in and near the Cascade margin (Gannett and Lite, 2004;

Gannett et al., 2001; Lite and Gannett, 2002). This is due to the shallow, short flow paths in and near the primary recharge zone as well as the hydrogeologic control of aquifer storage properties in this region. Mean monthly hydrographs from the regional groundwater flow model used in this study exhibit a range of seasonal variations. Changes in the timing and volume of recharge under future climate propagate through the groundwater system and result in changes in groundwater discharge to streams. One fundamental change is a shift in the timing of peak groundwater discharge from early summer to spring. There are also changes in total volume of groundwater discharge to certain streams. Although changes in total annual precipitation are small, changes in the volume of groundwater discharge to streams vary due to changes in the proportion of recharge to runoff, which ultimately affects the geographic distribution of recharge. In general, the response of groundwater discharge to projected future climate is similar under both the A1B and B1 greenhouse gas emission scenarios, except the magnitude of the response is large under A1B. The geographic differences in the response of groundwater discharge are described in the following sections.

Changes in Groundwater Discharge in the Southern Basin Stream

Groundwater discharge component to streams in the uppermost portion of the Deschutes Basin show that peak discharge is highest in early summer for the 1980s. Seasonality is seen in the mean monthly hydrograph of groundwater discharge for Odell

Creek, an upper elevation stream (Figure 21). This is the dominant pattern in the southern portion of the basin for both emission scenarios (Appendix G.1-G.15). Changes in discharge between time periods for a given month are statistically significant, indicating that increases in discharge are occurring from December to April (disjoint error bars in Figure 21A). Peak groundwater discharge shifts from May to earlier in the spring throughout the 21st century (Figure 21B). The mean monthly hydrograph shown for Odell Creek is typical of groundwater fed streams in the uppermost basin (Appendix G.1-G.14). In addition to the shift in timing of groundwater discharge, the cumulative mean annual amount of discharge for Odell Creek tends to increase by the end of the century (Figure 21;

Table 28). This also is typical for this portion of the basin (Appendix G.1-G.14). The increase in annual discharge is due largely to increases in winter volume. For Odell Creek, the increase in mean annual volume between the 1980s and 2020s is not statistically significant, however, those volumes are statistically smaller than volumes in the 2050s and 2080s (Figure 21A). The increase in groundwater discharge to these streams is due in part to increases in the ratio of recharge resulting from changes in timing and rate of snowmelt.

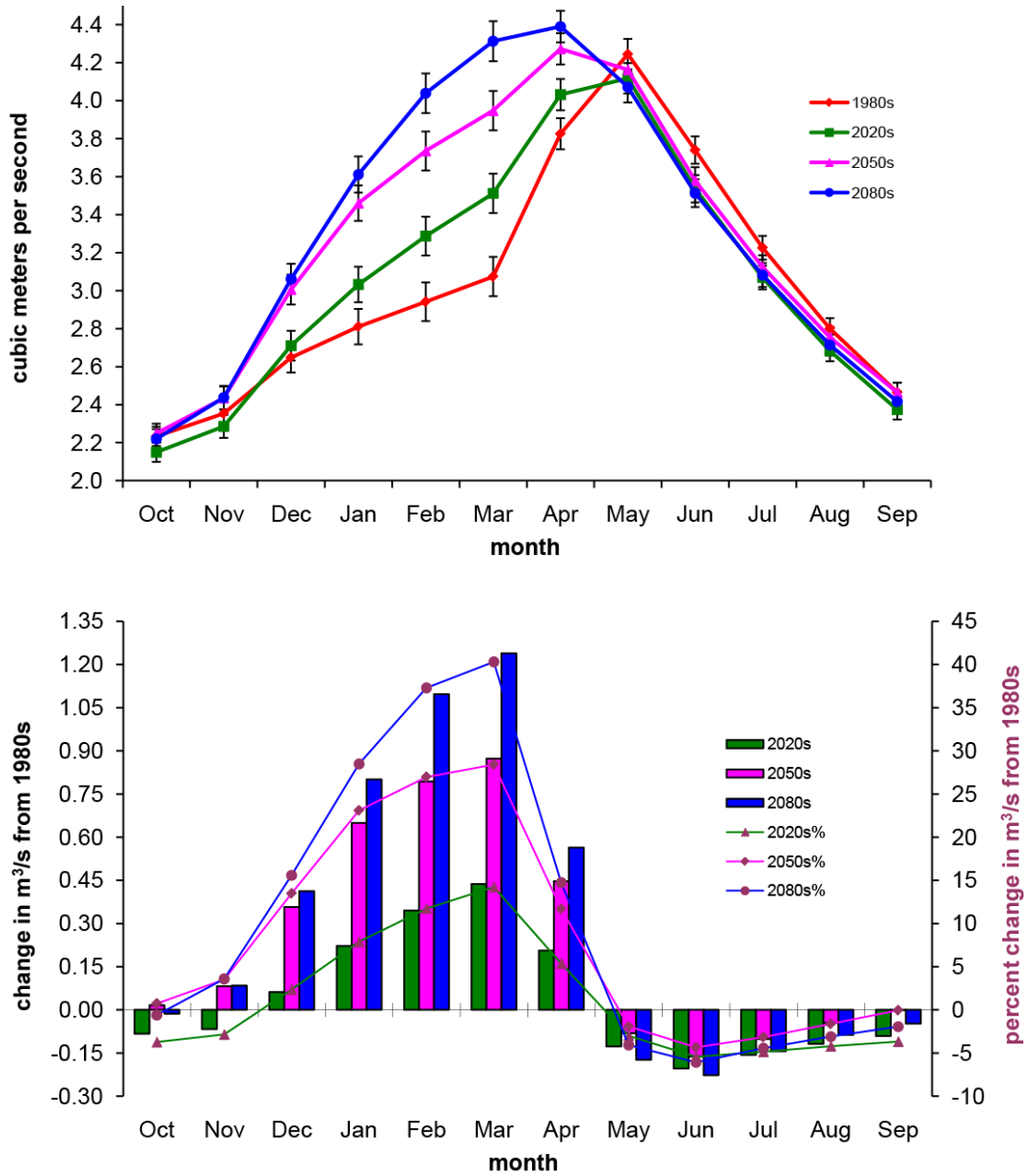


Figure 21. Odel Creek groundwater discharge: (Top) Groundwater flow model results of discharge using the A1B scenario forcing. (Bottom) The change in discharge (cfs) from the 1980s baseline period and the percent change in discharge showing the magnitude of the change .

Table 28. Odell Creek A1B scenario projected mean monthly groundwater discharge.

month	Odell Creek			
	1980s (m ³ /s)	2020s (m ³ /s)	2050s (m ³ /s)	2080s (m ³ /s)
Oct	2.233	2.150	2.250	2.220
Nov	2.353	2.286	2.435	2.437
Dec	2.648	2.711	3.006	3.061
Jan	2.811	3.032	3.460	3.611
Feb	2.942	3.287	3.735	4.039
Mar	3.074	3.512	3.947	4.313
Apr	3.826	4.032	4.273	4.390
May	4.244	4.117	4.163	4.071
Jun	3.740	3.536	3.577	3.513
Jul	3.226	3.069	3.124	3.082
Aug	2.801	2.683	2.755	2.714
Sep	2.464	2.374	2.463	2.416
mean	3.030	3.066	3.266	3.322

Changes in Groundwater Discharge in the Northern and Central Basin

Large spring complexes discharging to streams distant from the Cascades, such as those feeding the Deschutes River between Lower Bridge and Culver lack the prominent seasonal signal seen in streams close to the Cascades in the southern basin (Figure 22). The lack of seasonality is mostly due to diffusion of recharge pulses along the relatively long flow paths feeding these streams (see Gannett et al., 2001, Fig 32). Differences in the size of the seasonal pulse are also due to geographic differences in aquifer storage properties. The Metolius River mean monthly hydrograph shows slightly more seasonality than confluence area hydrographs because its headwaters are adjacent to the

Cascade Range in the northwest portion of the basin (Appendix G.21, G22). Because it integrates such a large area, however, the Metolius shows more loss of seasonality than small upper basin streams.

Unlike the southern Cascade area, there is a slight decrease in simulated mean monthly groundwater discharge to streams in the northern and central portions of the basin. Although statistically significant, losses in mean monthly discharges from the 1980s baseline period for inflow to the Deschutes River between Lower Bridge and Culver are small (Figure 22A-B). The same is true when the mean annual differences are considered although the aggregated monthly losses in baseflow for the 2020s and 2050s may possibly be significant when considering stream management (Table 29; Appendix G.20). These small mean annual volumetric losses are typical for the streams investigated in the northwestern and north-central discharge areas (Appendix G.15-24).

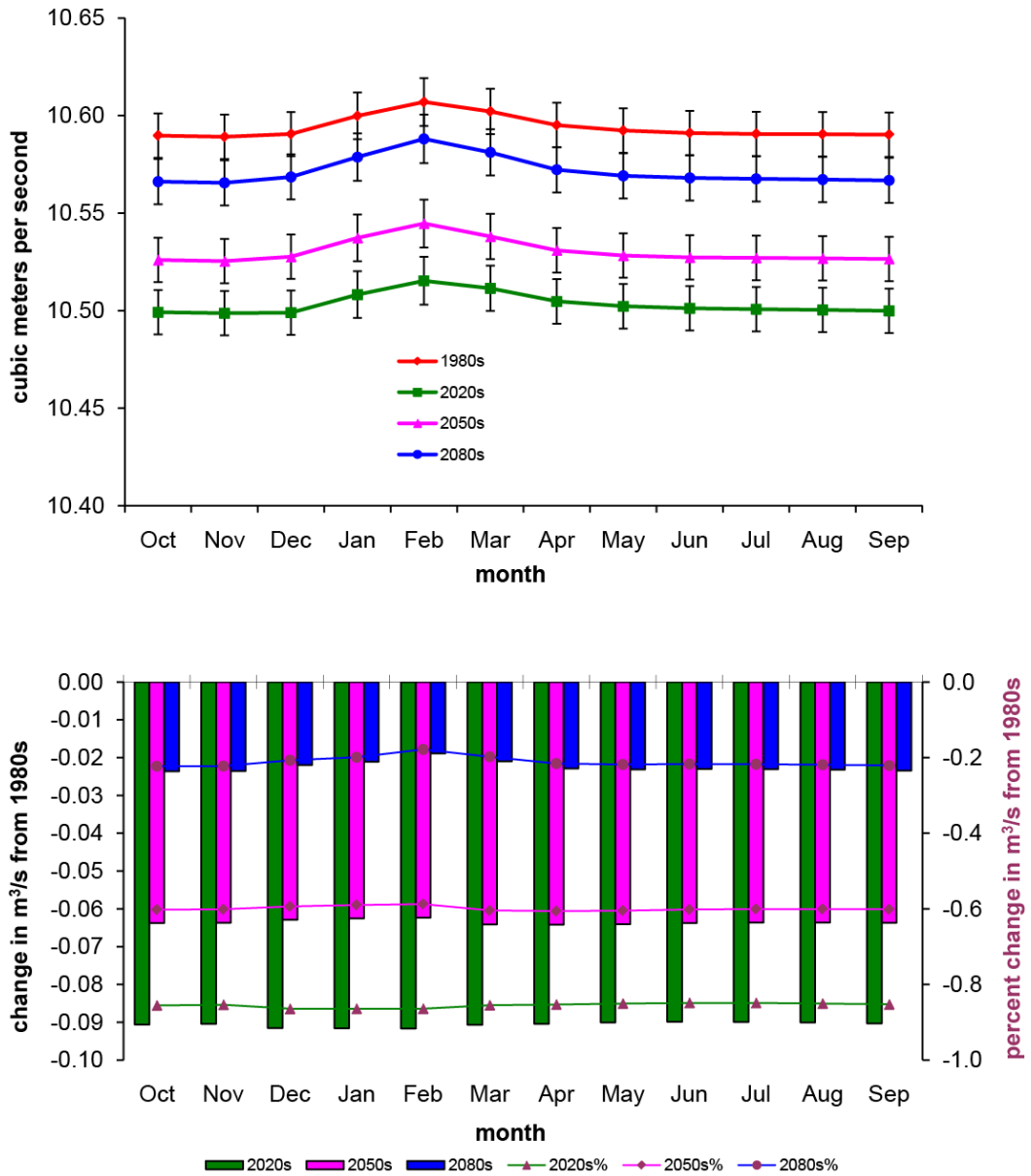


Figure 22. Deschutes inflow between Lower Bridge and Culver: (Top) Groundwater flow model results of discharge using the A1B scenario forcing. (Bottom) The change in discharge (cfs) from the 1980s baseline period and the percent change in discharge showing the magnitude of the change.

Table 29. Middle Deschutes River A1B scenario projected mean monthly groundwater discharge.

Inflow to Deschutes between Lower Bridge and Culver				
	1980s	2020s	2050s	2080s
month	(m ³ /s)	(m ³ /s)	(m ³ /s)	(m ³ /s)
Oct	10.590	10.499	10.526	10.566
Nov	10.589	10.499	10.525	10.565
Dec	10.590	10.499	10.528	10.569
Jan	10.600	10.508	10.537	10.579
Feb	10.607	10.515	10.545	10.588
Mar	10.602	10.511	10.538	10.581
Apr	10.595	10.505	10.531	10.572
May	10.592	10.502	10.528	10.569
Jun	10.591	10.501	10.527	10.568
Jul	10.591	10.501	10.527	10.568
Aug	10.590	10.500	10.527	10.567
Sep	10.590	10.500	10.526	10.567
mean	10.594	10.503	10.530	10.572

DISCUSSION

Simulated Response of Groundwater Discharge to Climate Change

The seasonality of groundwater discharge to streams and mean annual volumes are projected to change under the future climate scenarios considered here. That response varies geographically due to the length of the flow paths and aquifer storage properties. Increasing temperatures across time periods of the A1B and B1 emission scenarios cause seasonal changes in in-place recharge and runoff which manifests as a change in mean monthly groundwater discharge. These monthly changes represent shifts in the timing of annual discharge as well as changes in the mean annual volumes. Statistical testing of basin-wide averages indicates no differences in basin-wide precipitation and few mean annual differences in basin-wide recharge and runoff between time periods.

Mean annual volumetric changes in discharge cannot be attributed to seasonal shifts in recharge and runoff if basin-wide average volumes of mean annual recharge are not changing significantly between time periods. In order for mean annual volumetric changes in groundwater discharge to occur between time periods for different stream responses to vary across the basin; mean annual spatial distributions of recharge across the primary recharge zone must exhibit a similar difference (Appendix I). Warming increase changes the form of precipitation and affects the rate of snowmelt. However, a mean annual precipitation gradient varies spatially across the basin, but spatial changes in precipitation do not have the magnitude to account for changes in the spatial distribution of recharge (Appendix H). The delineated Three Sisters and near-crest North Cascades

Regions, receive the highest precipitation in the basin. Decreases in recharge here result from the infiltration capacities of soil being exceeded as more precipitation shifts from snow to rain, rain on snow events, and increased rate of snowmelt. Therefore mean annual decreases in recharge are offset mainly by mean annual increases in runoff but also by changes in evapotranspiration here (Appendix J; Appendix K). The infiltration capacity of soils in the South Cascades Region is relatively low and is exceeded by spring snowmelt during the 1980s. However, as the spring recharge pulse decreases and winter recharge increases via warming throughout the 21st century, a longer period of time is created for deep percolation to occur. Therefore, the increases in mean annual recharge are offset by decreases in mean annual runoff and changes in evapotranspiration in the Southern Cascades Region (Appendix J; Appendix K).

Model Uncertainty

Uncertainty in the hydrologic cycle projections presented here arises from two sources, imperfect knowledge of future emissions scenarios and limitations in the models used to make the projections. Model uncertainty may be due to limitations in the mathematical representation of physical processes, imperfect knowledge of the empirical coefficients in those equations, and imperfect boundary and initial conditions used in the models. Downscaling may introduce error via interpolation and errors in the observational climate data used to direct the downscaling (Benestad et al., 2008; Maurer, 2007). Uncertainty associated with the GCM output fields used to drive hydrologic

models are generally understood to dominate uncertainty in the resulting projections of the hydrologic cycle (Chang and Jung, 2010; Maurer, 2007; Prudhomme and Davies, 2009).

Both qualitative and quantitative methods have been developed to evaluate model uncertainty. These methods seek to assess the reliability of model projections given the sources of uncertainty described above. Formal methods, such as Bayesian inference and other statistical inference methods have been developed for this purpose and are used to compute probability density functions for GCMs and other types of models. Here, uncertainty in future GCM projections was handled through the use of ensemble means after individual runs through the DPM. Underlying this approach is the presumption that ensembles are a good representation of the distribution of future climate changes (Mote et al., 2008). A multi-model mean or median from an ensemble of GCMs has been shown to generally outperform any single GCM (Gleckler et al., 2008).

Formal sensitivity analysis and parameter optimization using combinations of the important parameters leading to an uncertainty analysis for the DPM was an early goal in project development but was eventually deemed unfeasible. Any optimization scheme requires an “objective function” against which model output for any given combination of model parameters may be compared. However, the highly regulated nature of waterways in the basin--baseflow separation is not possible--and the lack of hydrologic flux data made that function difficult to define. This is the same issue which prevents a rigorous statistical validation of the DPM, as discussed in the model validation section.

Thus, probability density functions for recharge and runoff throughout the basin cannot be constructed.

Boyd (1996) used multiple regressions to identify the most important parameters for estimating recharge for the entire basin. These include specific yield, saturated vertical hydraulic conductivity, and soil texture (silt, sand, and clay ratios), along with the precipitation. On a finer scale, interception capacity, root depth, effective slope, effective length, and effective slope were also shown to be important in some areas. This suggests that soil properties, land cover, elevation, effective length, and effective slope are parameters to be adjusted for a sensitivity analysis of the DPM.

Parameter values for the regional groundwater flow model were determined through regression analysis using MODFLOWP (Gannett and Lite, 2004). Hydraulic conductivity parameters for the model were optimized and 95% confidence intervals were established for zones representing geographic areas at certain depths within the basin for the model. When establishing steady-state model parameters prior to optimization, the model developers reported taking care to remain faithful to the geologic data and overall geologic understanding (Gannett and Lite, 2004). Optimization did not cause an unreasonable departure from the geologic data (Gannett and Lite, 2004).

Both the DPM and regional groundwater flow model have been applied in the upper Deschutes Basin using historical data with reasonable success (Gannett and Lite, 2004). The greatest source of uncertainty in the suite of models used here is in the GCM projections of future change. Uncertainty in the downscaled GCM data has been

addressed using ensemble means for two emission scenarios. Thus, the projections reported here should be a useful representation of future changes in recharge and runoff in the upper Deschutes.

CONCLUSIONS

Simulations of the hydrologic response to climate change using downscaled GCM output along with mass balance and groundwater flow models indicates that the upper Deschutes Basin's snowpack-dominated hydrology is sensitive to warming temperatures of projected future climate. The ensembles of climate projections used here yield increasing mean annual basin-wide temperatures with no statistically significant change in basin-wide average precipitation for either emission scenario over the next century. This forcing on basin hydrology in turn affects the snowpack by changing the form of precipitation resulting in less snow and more rain and by increasing the rate of snowmelt. The higher of the two emission scenarios used in this study, SRES A1B, yields the highest temperatures and largest changes in basin hydrology. The ensemble mean annual temperature averaged basin-wide for the A1B scenario warms $1.2\pm 0.5^{\circ}\text{C}$ between the 1980s and 2020s and the warming continues at about the same rate through the rest of the century. The B1 emission scenario's ensemble mean annual temperature averaged for the basin warms $1.0\pm 0.4^{\circ}\text{C}$ between the 1980s and 2020s and continues on with average warming of 0.8°C between future climate periods. The DPM model driven by these forcings produces decreasing spring recharge and runoff and increasing winter recharge and runoff (Figure 23).

Evaluating the geographic distribution of changes in recharge and runoff provides additional insights into the processes underlying those changes and regions most

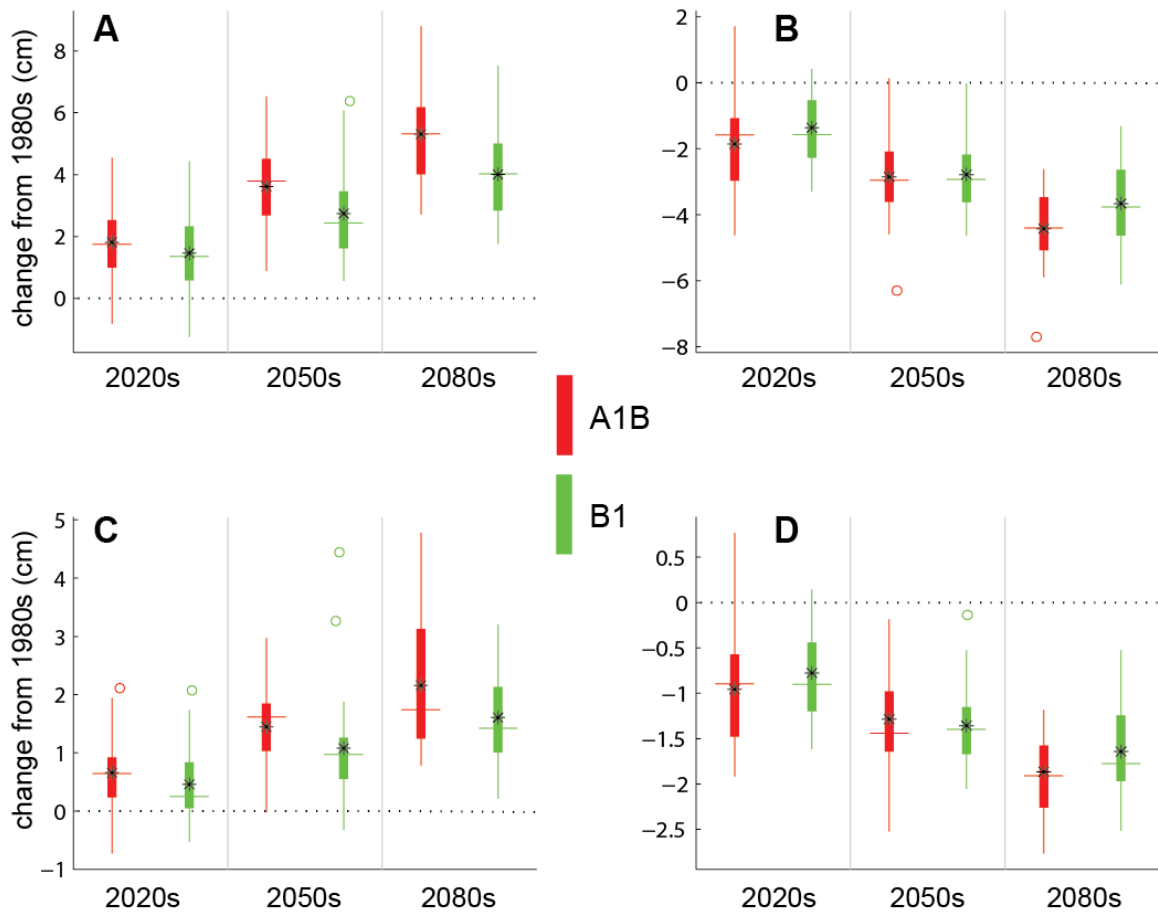


Figure 23. Anomaly plots of changes in recharge and runoff from the 1980s. Vertical scales differ between plots and black asterisks in boxes indicate mean annual values. A) Increasing winter recharge. B) Decreasing spring recharge. C) Increasing winter recharge. D) Decreasing spring runoff.

affected by future warming. Spring and winter spatial change maps created with DPM data for both emission scenarios show that the magnitude of changes in recharge and direct runoff differ somewhat by location in the basin. Seasonal shifts in recharge occur throughout the primary recharge zone, while the largest seasonal shifts in runoff occur in the southern half of the Cascades within the basin.

Groundwater flow simulations yield a range in response of groundwater discharge to streams depending on the scale of the groundwater system (length of flow path) and location in the basin. Smaller streams near the Cascade margin and in the upper portion of the basin, which exhibit strong seasonality will likely experience shifts in timing of peak discharge, as well as volumetric gains through the 21st century in response to warming. These shifts in timing are the result of seasonal shifting of in-place recharge.

Springs feeding streams in the northern and central portions of the basin, such as the Middle Deschutes River, lack a prominent seasonal signal. Also, modeled groundwater discharges to these streams tend to have very small volumetric decreases for future climate periods. The small changes in discharge volume for the large streams and the changes in discharge volume to the southern, smaller stream systems are due to more precipitation falling as rain and the increasing rate of snowmelt due to warming.

REFERENCES

- Allen, R., 1996, Assessing Integrity of Weather Data for Reference Evapotranspiration Estimation: *Journal of Irrigation and Drainage Engineering*, v. 122, no. 2, p. 97-106.
- , 1997, Self-Calibrating Method for Estimating Solar Radiation from Air Temperature: *Journal of Hydrologic Engineering*, v. 2, no. 2, p. 56-67.
- Bauer, H., and Vaccaro, J., 1987, Documentation of a Deep Percolation Model for Estimating Ground-Water Recharge: US Geological Survey Open-File Report, p. 86-536.
- Benestad, R. E., Hanssen-Bauer, I., and Chen, D., 2008, Empirical-Statistical Downscaling: Hackensack, World Scientific Publishing, 215 p.
- Boyd, T., 1996, Groundwater Recharge of the Middle Deschutes Basin, Oregon: Portland, Oregon, Portland State University: MS thesis, 86 p.
- Bureau of Reclamation, 2009, AgriMet: The Pacific Northwest Cooperative Agricultural Weather Network: accessed January 20, 2009: <http://www.usbr.gov/pn/agrimet/>
- Chang, H., and Jung, I., 2010, Spatial and Temporal Changes in Runoff Caused by Climate Change in a Complex Large River Basin in Oregon: *Journal of Hydrology*.
- Collins, W., Bitz, C., Blackmon, M., Bonan, G., Bretherton, C., Carton, J., Chang, P., Doney, S., Hack, J., and Henderson, T., 2006, The Community Climate System Model: CCSM3: *Journal of Climate*, v. 19, no. 11, p. 2122-2143.
- Daly, C., Neilson, R., and Phillips, D., 1994, A Statistical-Topographic Model for Mapping Climatological Precipitation over Mountainous Terrain: *Journal of Applied Meteorology*, v. 33, no. 2, p. 140-158.
- Dunne, T., and Leopold, L., 1978, *Water in Environmental Planning*, 818 pp, WH Freeman, New York.
- Feng, S., and Hu, Q., 2007, Changes in Winter Snowfall/Precipitation Ratio in the Contiguous United States: *J. Geophys. Res.*, v. 112, no. D15, p. D15109.

- Gannett, M., and Lite, K., 2004, Simulation of Regional Ground-Water Flow in the Upper Deschutes Basin, Oregon: U.S. Geological Survey Water-Resources Investigations Report 03-4195, 84 p.
- Gannett, M. W., Lite, K. E., Jr., Morgan, D. S., and Collins, C. A., 2001, Ground-Water Hydrology of the Upper Deschutes Basin, Oregon: U.S. Geological Survey Water-Resources Investigations Report 00-4162, 78 p.
- Gannett, M. W., Manga, M., and Lite, K. E., Jr., 2003, Groundwater Hydrology of the Upper Deschutes Basin and its Influence on Streamflow, *in* O'Conner, J. E., and Grant, G. E., eds., *A Peculiar River: Geology, Geomorphology, and Hydrology of the Deschutes River, Oregon*: Washington D.C., American Geophysical Union, p. 31-49.
- Gleckler, P., Taylor, K., and Doutriaux, C., 2008, Performance Metrics for Climate Models: *Journal of Geophysical Research*, v. 113, no. D6, p. D06104.
- Gordon, C., Cooper, C., Senior, C., Banks, H., Gregory, J., Johns, T., Mitchell, J., and Wood, R., 2000, The Simulation of SST, Sea Ice Extents and Ocean Heat Transports in a Version of the Hadley Centre Coupled Model Without Flux Adjustments: *Climate Dynamics*, v. 16, no. 2, p. 147-168.
- Hargreaves, G., and Samani, Z., 1982, Estimating Potential Evapotranspiration: *Journal of the Irrigation and Drainage Division*, v. 108, no. 3, p. 225-230.
- Hasumi, H., and Emori, S., 2004, K-1 coupled GCM (MIROC) Description.
- Hochberg, Y., and Tamhane, A. C., 1987, *Multiple Comparison Procedures*: Hoboken, NJ, John Wiley & Sons.
- Jungclaus, J., Keenlyside, N., Botzet, M., Haak, H., Luo, J., Latif, M., Marotzke, J., Mikolajewicz, U., and Roeckner, E., 2006, Ocean Circulation and Tropical Variability in the Coupled Model ECHAM5/MPI-OM: *Journal of Climate*, v. 19, no. 16, p. 3952-3972.
- Legutke, S., Voss, R., and Klimarechenzentrum, D., 1999, ECHO-G: The Hamburg atmosphere-ocean coupled circulation model, DKRZ-Report, v. 18.
- Lite, K. E., Jr., and Gannett, M. W., 2002, Geologic Framework of the Regional Ground-Water Flow System in the Upper Deschutes Basin, Oregon: US Geological Survey Water-Resources Investigations Report 02-4015, 44 p.

- Marti, O., Braconnot, P., Bellier, J., Benshila, R., Bony, S., Brockmann, P., Cadule, P., Caubel, A., Denvil, S., and Dufresne, J., 2005, The New IPSL Climate System Model: IPSL-CM4: Note du Pôle de Modélisation, v. 26, p. 1288–1619.
- Maurer, E., 2007, Uncertainty in Hydrologic Impacts of Climate Change in the Sierra Nevada, California, Under Two Emissions Scenarios: *Climatic Change*, v. 82, no. 3, p. 309-325.
- McDonald, M., and Harbaugh, A., 1988, A Modular Three-Dimensional Finite-Difference Ground-Water Flow Model: US Geological Survey Techniques of Water-Resources Investigations, Book 6, Chapter A1: US Geological Survey, Reston, VA, USA, p. 586.
- Milly, P. C. D., Betancourt, J., Falkenmark, M., Hirsch, R. M., Kundzewics, Z. W., Lettenmaier, D. P., and Stouffer, R. J., 2008, Stationarity is Dead: Whither Water Management?: *Science*, v. 319, p. 573-574.
- Mote, P., Salathé, E., Dulière, V., and Jump, E., 2008, Scenarios of Future Climate for the Pacific Northwest.
- NOAA Satellite and Information Service, and National Climatic Data Center, 2009, NNDC Climate Data Online accessed January 13, 2009: <http://www7.ncdc.noaa.gov/CDO/cdo>
- Oregon Climate Service, 2009: accessed 1/19/2009: <http://www.ocs.oregonstate.edu/index.html>
- Prudhomme, C., and Davies, H., 2009, Assessing Uncertainties in Climate Change Impact Analyses on the River Flow Regimes in the UK. Part 2: future climate: *Climatic Change*, v. 93, no. 1, p. 197-222.
- Robinson, P., Brem, G., and McKee, E., 1984, John Day Formation of Oregon: A Distal Record of Early Cascade Volcanism: *Geology*, v. 12, no. 4, p. 229.
- Salas-Mélia, D., Chauvin, F., Déqué, M., Douville, H., Gueremy, J., Marquet, P., Planton, S., Royer, J., and Tyteca, S., 2006, Description and Validation of the CNRM-CM3 Global Coupled Model: *Climate Dynamics*.
- Salathe, E., 2005, Downscaling Simulations of Future Global Climate with Application to Hydrologic Modelling: *International Journal of Climatology*, v. 25, no. 4, p. 419-436.

- Salathe, E. P., Jr, Mote, P. W., and Wiley, M. W., 2007, Review of Scenario Selection and Downscaling Methods for the Assessment of Climate Change Impacts on Hydrology in the United States Pacific Northwest: *International Journal of Climatology*, v. 27, no. 12, p. 1611-1621.
- Sherrod, D., and Smith, J., 2000, Geologic Map of Upper Eocene to Holocene Volcanic and Related rocks of the Cascade Range, Oregon, US Geological Survey Washington, DC.
- Sherrod, D., Taylor, E., Ferns, M., Scott, W., Conrey, R., and Smith, G., 2004, Geologic Map of the Bend 30- \times 60-Minute Quadrangle, Central Oregon.
- Taylor, G. H., 1993, Normal Annual Precipitation: State of Oregon: Corvallis, Oregon State University, Oregon Climate Service, map.
- Vaccaro, J., 2007, A Deep Percolation Model for Estimating Ground-Water Recharge: Documentation of Modules for the Modular Modeling System of the US Geological Survey: U.S. Geological Survey Scientific Investigations Report 2006-5318, p. 30.
- Washington, W., Weatherly, J., Meehl, G., Semtner Jr, A., Bettge, T., Craig, A., Strand Jr, W., Arblaster, J., Wayland, V., and James, R., 2000, Parallel Climate Model (PCM) Control and Transient Simulations: *Climate Dynamics*, v. 16, no. 10, p. 755-774.
- Widmann, M., Bretherton, C., and Salathé, E. P., Jr, 2003, Statistical Precipitation Downscaling Over the Northwestern United States Using Numerically Simulated Precipitation as a Predictor: *Journal of Climate*, v. 16, no. 5, p. 799-816.
- Wood, A., Maurer, E., Kumar, A., and Lettenmaier, D., 2002, Long Range Experimental Hydrologic Forecasting for the Eastern US: *J. Geophys. Res.*, v. 107, no. 4429, p. 98195-2700.

APPENDIX A: Temperature Regression Statistics

The following tables list the correlation coefficient, the coefficient determination, standard error and average residual for regression equations used with the specified regressand and combinations of regressors.

Appendix A.1. Statistics generated from the minimum temperature regressions for Brothers.

Regression	R	R²	Standard error	Average residual
Brothers vs. All	0.94	0.87	4.31	3.34
w/o Prineville	0.93	0.87	4.36	3.37
w/o Redmond	0.94	0.87	4.32	3.35
w/o Prineville & Redmond	0.93	0.87	4.39	3.40

Appendix A.2. Statistics generated from the maximum temperature regressions for Brothers.

Regression	R	R²	Standard error	Average residual
Brothers vs. All	0.98	0.95	4.05	2.96
w/o Prineville	0.97	0.95	4.13	3.04
w/o Redmond	0.98	0.95	4.05	2.96
w/o Prineville & Redmond	0.97	0.95	4.14	3.04

Appendix A.3. Statistics generated from the minimum temperature regressions for Prineville.

Regression	R	R²	Standard error	Average residual
Prineville vs. All	0.93	0.86	4.18	3.30
w/o Bend	0.91	0.84	4.47	3.54
w/o Brothers	0.92	0.85	4.23	3.33
w/o Madras	0.93	0.86	4.19	3.29
w/o Redmond	0.92	0.85	4.22	3.33
w/o Bend & Madras	0.91	0.83	4.50	3.54
w/o Bend & Redmond	0.90	0.82	4.63	3.70
w/o Brothers & Redmond	0.92	0.85	4.29	3.37
w/o Madras & Redmond	0.92	0.85	4.26	3.33

Appendix A.4. Statistics generated from the maximum temperature regressions for Prineville.

Regression	R	R²	Standard error	Average residual
Prineville vs. All	0.97	0.95	3.88	2.90
w/o Bend	0.97	0.95	4.05	3.07
w/o Brothers	0.97	0.95	3.96	2.96
w/o Madras	0.97	0.95	4.00	3.00
w/o Redmond	0.97	0.95	3.93	2.92
w/o Bend & Redmond	0.97	0.94	4.12	3.10
w/o Brothers & Redmond	0.97	0.95	4.02	2.99

Appendix A.5. Statistics generated from the minimum temperature regressions for Bend.

Regression	R	R²	Standard error	Average residual
Bend vs. All	0.96	0.92	3.08	2.41
w/o Prineville	0.96	0.91	3.29	2.56
w/o Redmond	0.96	0.92	3.21	2.51
w/o Madras & Prineville	0.95	0.91	3.32	2.57
w/o Prineville & Redmond	0.95	0.90	3.52	2.76

Appendix A.6. Statistics generated from the maximum temperature regressions for Bend.

Regression	R	R²	Standard error	Average residual
Bend vs. All	0.98	0.96	3.29	2.52
w/o Prineville	0.98	0.96	3.44	2.61
w/o Redmond	0.98	0.96	3.29	2.52
w/o Madras & Prineville	0.98	0.96	3.47	2.62
w/o Prineville & Redmond	0.98	0.96	3.46	2.61

Appendix A.7. Statistics generated from the temperature regressions for Wickiup.

Regression	R	R²	Standard error	Average residual
Wickiup vs. All	0.97	0.95	4.02	2.99

Appendix A.8. Statistics generated from the linear regressions for the Redmond climate station using records from the nearby Agrimet weather station at Powell Butte as the regressor for minimum and maximum temperatures.

Regression	R	R²	Standard error	Average residual
Redmond vs Agrimet (T_{min})	0.95	0.90	3.71	2.78
Redmond vs Agrimet (T_{max})	0.98	0.96	3.51	2.36

APPENDIX B: Centroid Selection

The following tables show the basis for downscaled GCM centroid selection. Mean monthly total precipitation hydrographs were compared for the longest stationary record of a climate station and its four nearest centroids for all downscaled GCMs. An exception is the Bend climate station, where only the three centroids were available to compare to the historical record for five of the downscaled GCMs. Mean absolute error (MAE) is used to judge the fit between downscaled GCM forecasts for a centroid and historical precipitation recorded at the stations. MAE is calculated as follows:

$$MAE = \frac{1}{n} \sum_{i=1}^n |p_i - h_i|$$

In which, $n = 12$ (for each month of the hydrograph), p_i is a downscaled GCM predicted mean total precipitation for a month, and h_i is the mean total historical amount of precipitation recorded at the climate station for the same month. All MAEs are reported in millimeters and the best fit to a historical record is highlighted in the tables along with the location of the centroid, latitude and longitude, with the best overall fit. The centroid with the best fit to the historical record of a station for the majority of downscaled GCMs was selected for use with ensembles. However, two centroids were of nearly equal use as a future surrogate Redmond station. Data had already been compiled and processed for three of the eight downscaled GCMs for one of the centroids, so this particular centroid was selected.

Appendix B1. Centroids nearest the Bend climate station

centroid location	ccsm3	cnrm	echam5	echo-g	hadcm3	ipsl	miroc	pcm1
44.03125 -121.34375	n/a	n/a	n/a	2.80	n/a	2.06	n/a	n/a
44.03125 -121.28125	1.74	1.76	1.92	1.82	1.57	1.18	1.66	1.92
44.09375 -121.28125	2.47	2.55	2.16	2.22	2.92	2.12	3.02	2.91
44.09375 -121.34375	1.87	1.92	1.89	1.99	1.97	1.29	2.02	2.14

Appendix B2. Centroids nearest the Madras climate station

centroid location	ccsm3	cnrm	echam5	echo-g	hadcm3	ipsl	miroc	pcm1
44.21875 -121.15625	1.86	1.60	1.93	1.77	1.79	1.48	1.78	1.98
44.21875 -121.09375	1.75	1.57	1.84	1.75	1.45	1.21	1.73	1.84
44.28125 -121.09375	2.19	2.18	2.29	2.40	1.52	1.72	2.12	2.16
44.28125 -121.15625	2.34	2.30	2.44	2.53	1.61	1.85	2.24	2.31

Appendix B3. Centroids nearest the Prineville climate station

centroid location	ccsm3	cnrm	echam5	echo-g	hadcm3	ipsl	miroc	pcm1
44.21875 -121.15625	3.58	3.29	3.47	3.63	3.36	3.03	3.68	3.41
44.21875 -121.09375	2.12	2.10	2.00	2.12	2.06	1.78	2.18	2.26
44.28125 -121.09375	2.53	2.38	2.45	3.27	2.52	2.15	2.57	2.55
44.28125 -121.15625	3.01	2.83	2.99	3.03	2.94	2.61	3.14	3.00

Appendix B4. Centroids nearest the Redmond climate station

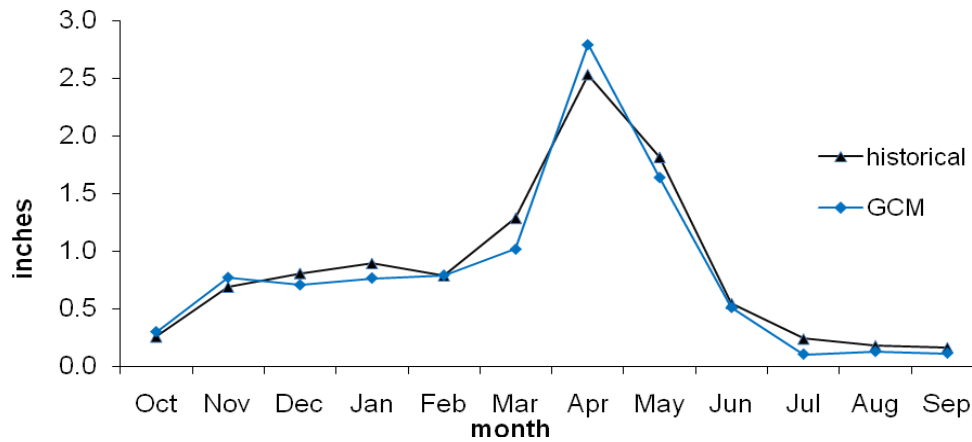
centroid location	ccsm3	cnrm	echam5	echo-g	hadcm3	ipsl	miroc	pcm1
44.21875 -121.15625	1.35	1.83	1.64	1.68	1.46	1.31	1.46	1.82
44.21875 -121.09375	1.76	1.64	1.86	1.83	1.67	1.36	1.90	1.84
44.28125 -121.09375	1.57	1.58	1.56	1.63	1.87	1.28	1.86	1.83
44.28125 -121.15625	1.58	1.71	1.57	1.65	1.95	1.37	1.94	2.01

Appendix B5. Centroids nearest the Wickiup climate station

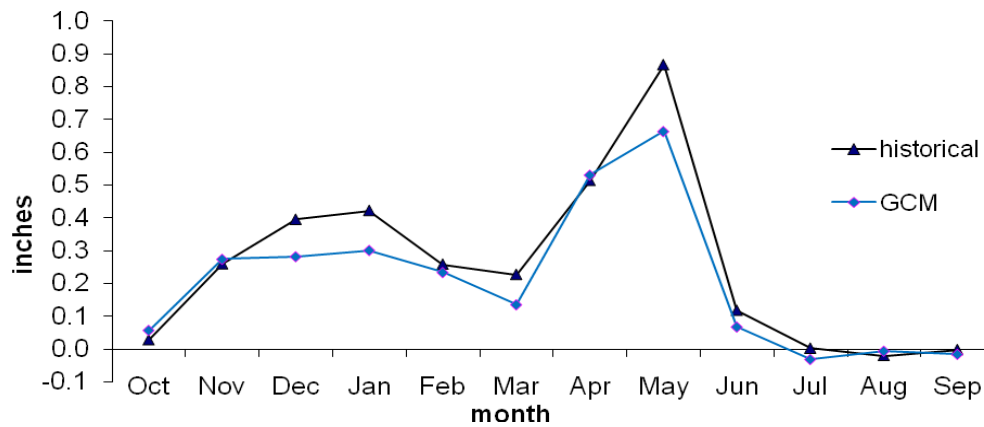
centroid location	ccsm3	cnrm	echam5	echo-g	hadcm3	ipsl	miroc	pcm1
43.65625 -121.71875	6.01	7.08	6.86	7.92	4.81	6.22	5.30	5.79
43.65625 -121.65625	4.94	5.99	5.51	6.80	3.75	5.16	4.52	4.72
43.71875 -121.65625	3.07	3.50	3.96	3.34	1.91	1.98	2.96	2.97
43.71875 -121.71875	4.39	5.43	5.36	6.20	3.34	4.58	3.50	10.02

APPENDIX C: 1980s Historical Record and Ensemble Mean GCM Recharge and Runoff Comparisons for the DPM

Mean monthly hydrographs comparing DPM basin-wide averaged recharge and runoff data for the 1980s historical climate stations' data and the 1980s GCM ensemble mean hindcast.



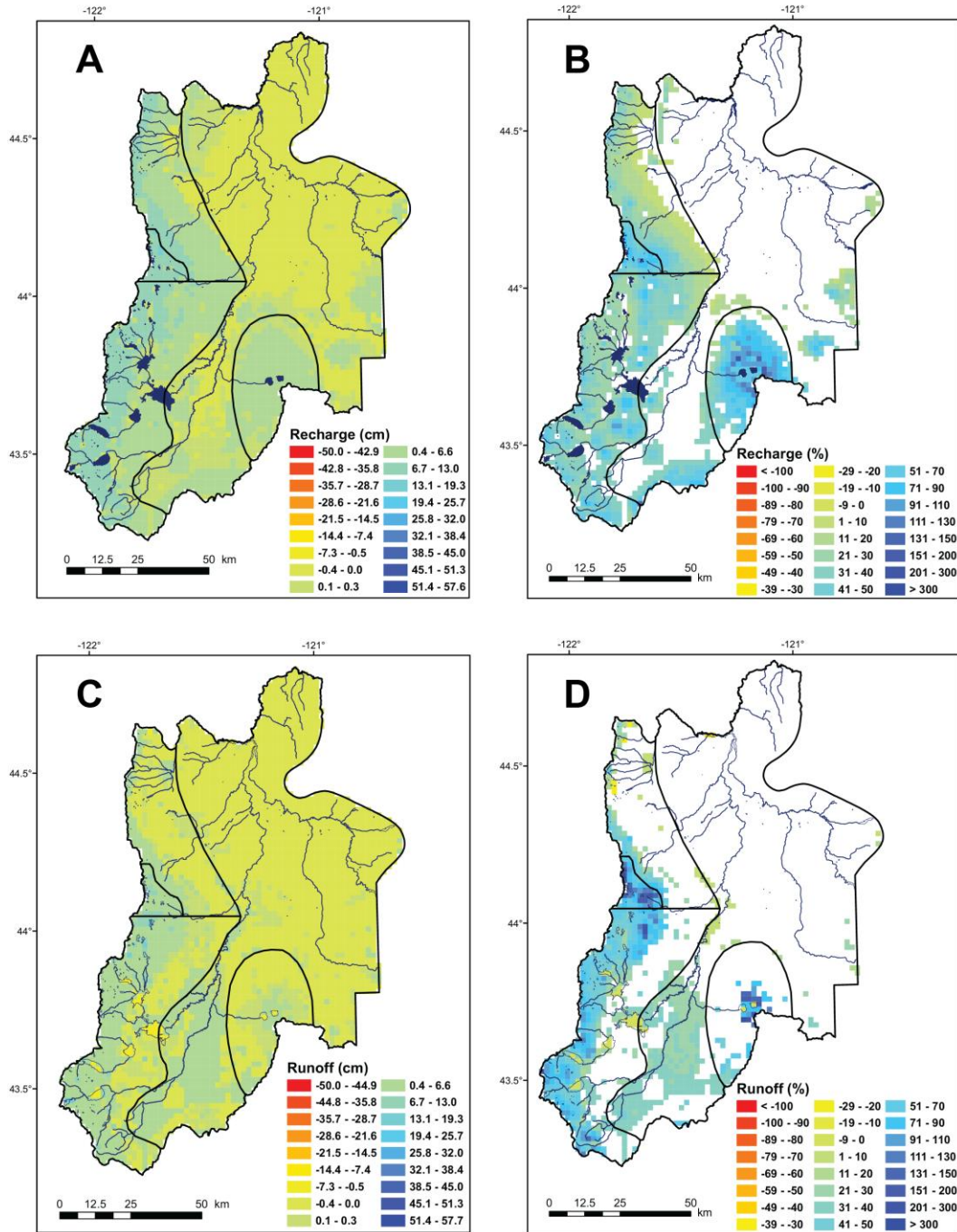
Appendix C.1. Basin-wide calculated recharge calculated by the DPM driven with 1980s historical climate data and 1980s downscaled GCM ensemble hindcast.



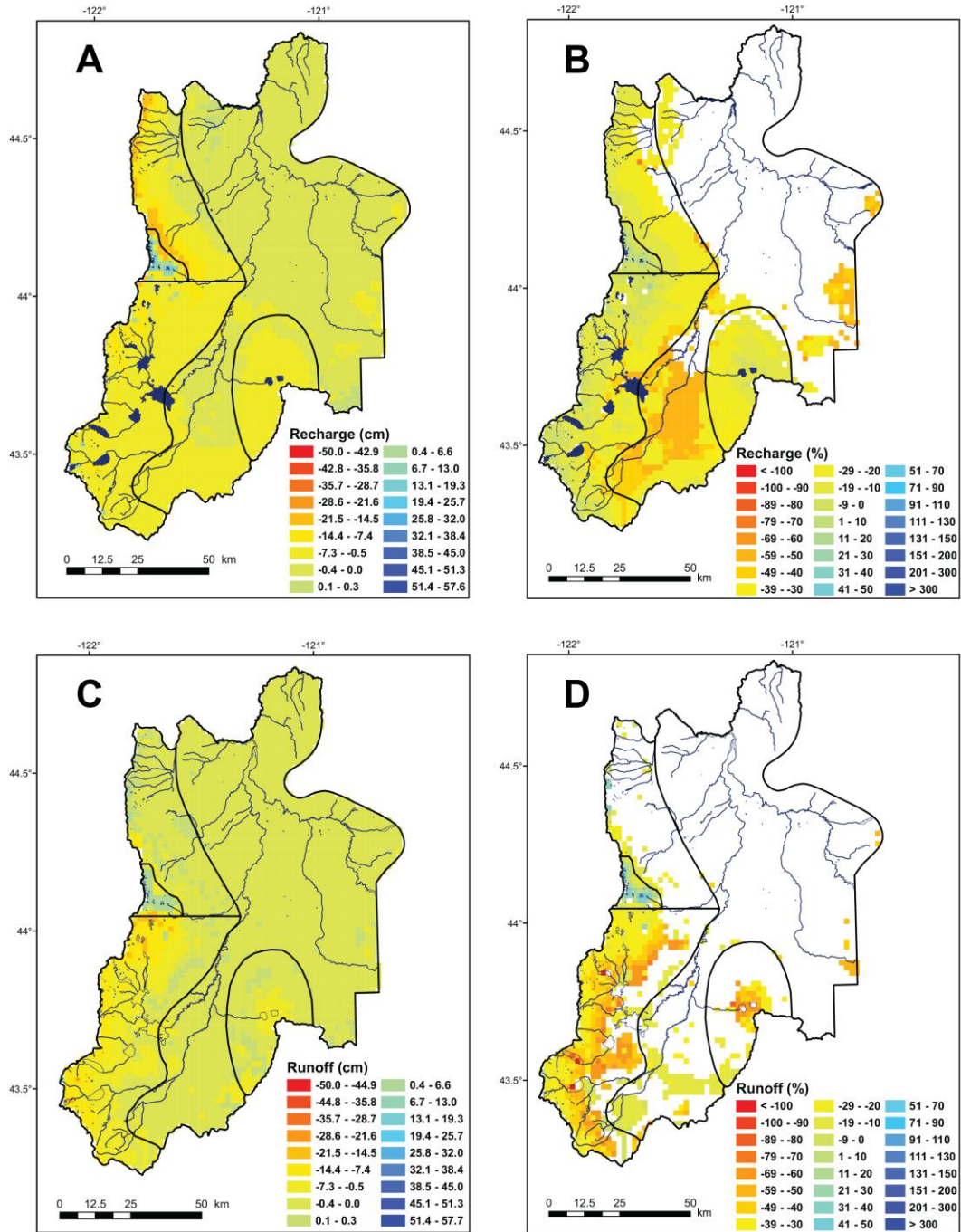
Appendix C.2. Basin-wide averaged runoff calculated by the DPM driven with 1980s historical climate data and 1980s downscaled GCM ensemble hindcast.

APPENDIX D: 2020s Spatial Changes

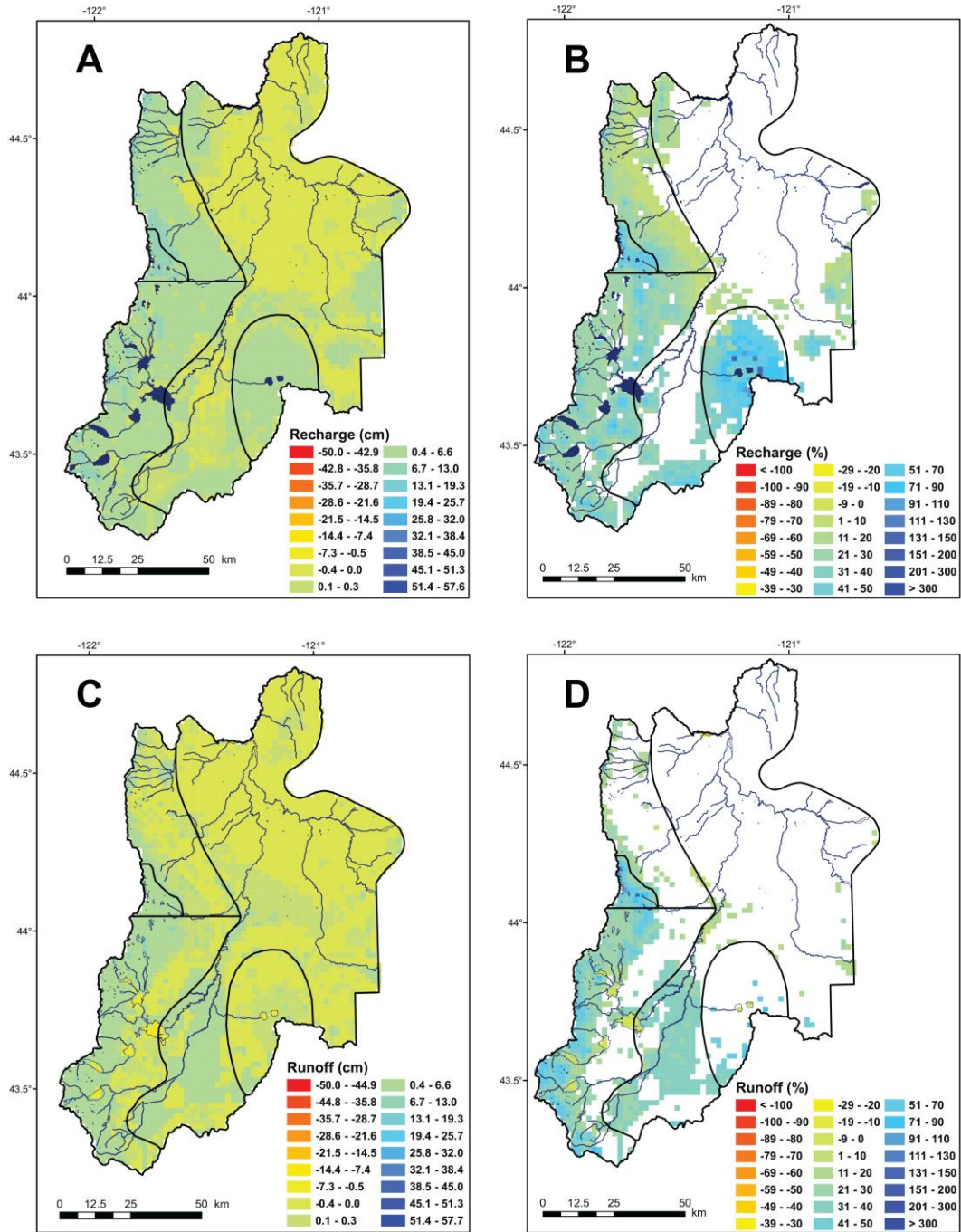
The following figures show the spatial changes from the 1980s base period winter and spring seasons as calculated by the DPM for the 2020s. The SRES A1B ensemble mean spatial changes for winter are shown followed by the corresponding A1B spring changes. B1 winter and spring changes are presented in the same manner. Figures include the boundaries of the delineated regions of interest. Note that recharge does not occur in open water cells in the southern portion of the basin and these cells are shaded in the darkest blue along with streams in the basin.



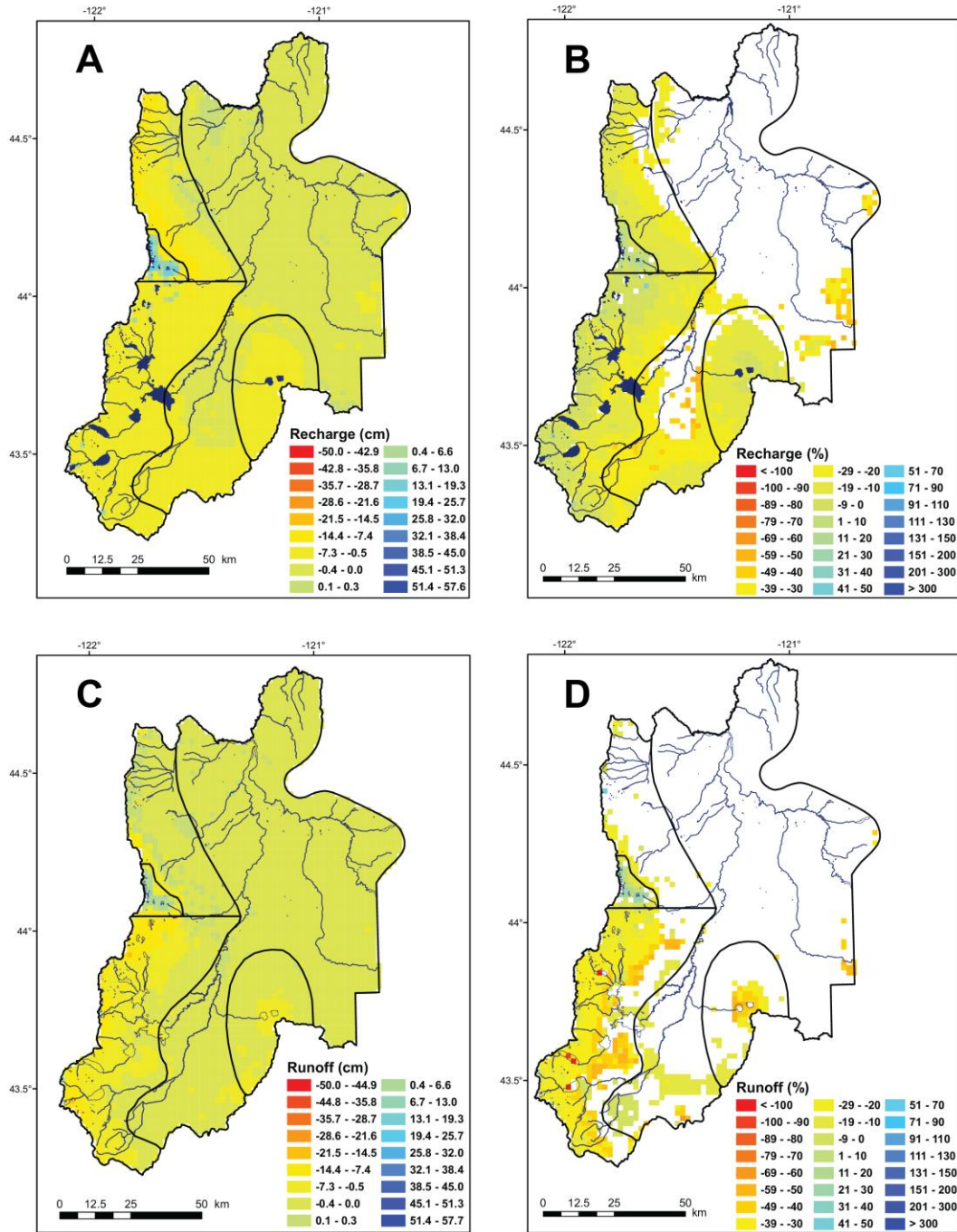
Appendix D.1. (A) Absolute change in winter recharge for the 2020s A1B period. (B) Percent change in winter recharge for the 2020s A1B period. (C) Absolute change in winter runoff for the 2020s A1B period. (D) Percent change in winter runoff for the 2020s A1B period.



Appendix D.2. (A) Absolute change in spring recharge for the 2020s A1B period. (B) Percent changes in spring recharge for the 2020s A1B period. (C) Absolute change in spring runoff for the 2020s A1B period. (D) Percent changes in spring runoff for the 2020s A1B period.



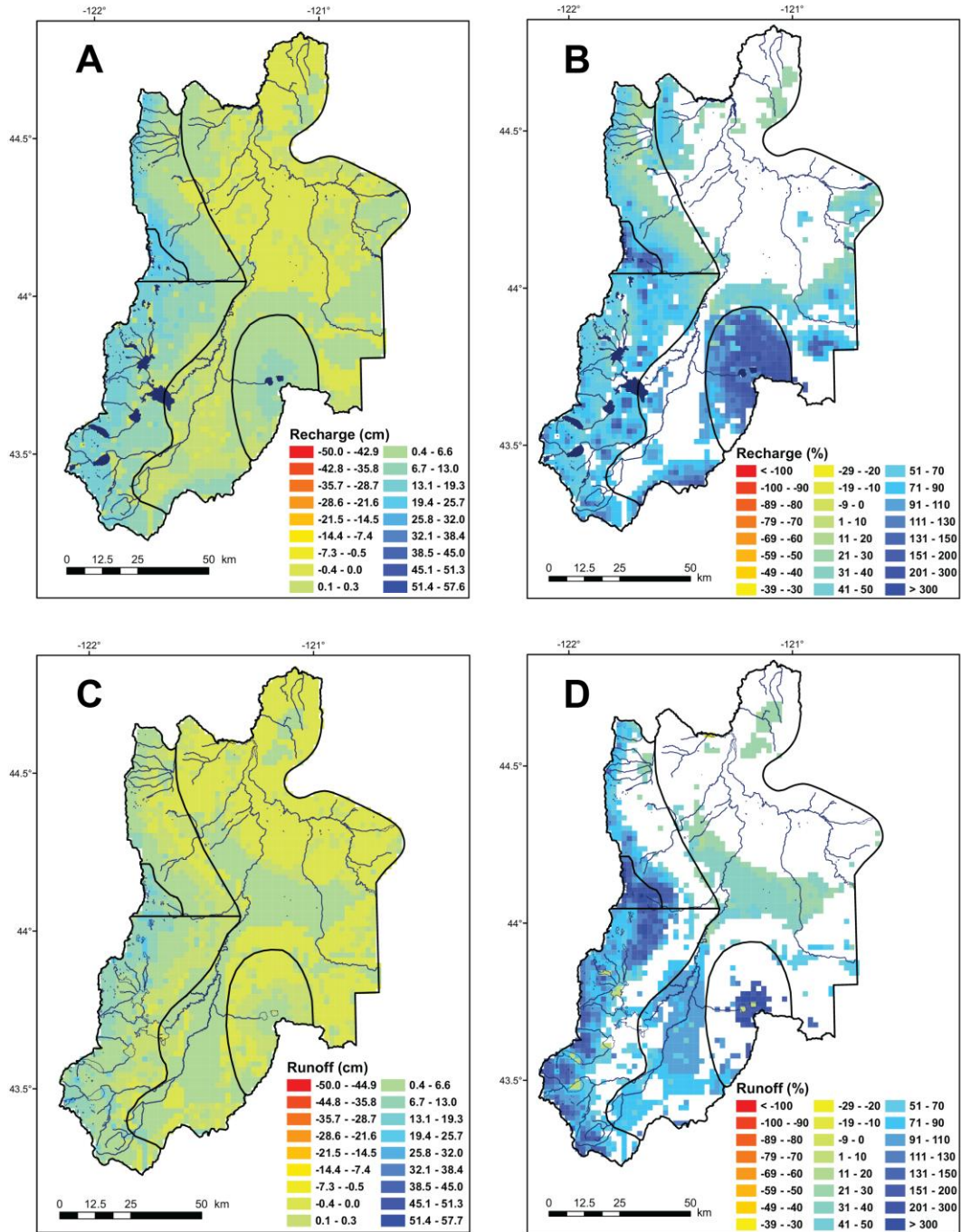
Appendix D.3. (A) Absolute change in winter recharge for the 2020s B1 period. (B) Percent change in winter recharge for the 2020s B1 period. (C) Absolute change in winter runoff for the 2020s B1 period. (D) Percent change in winter runoff for the 2020s B1 period.



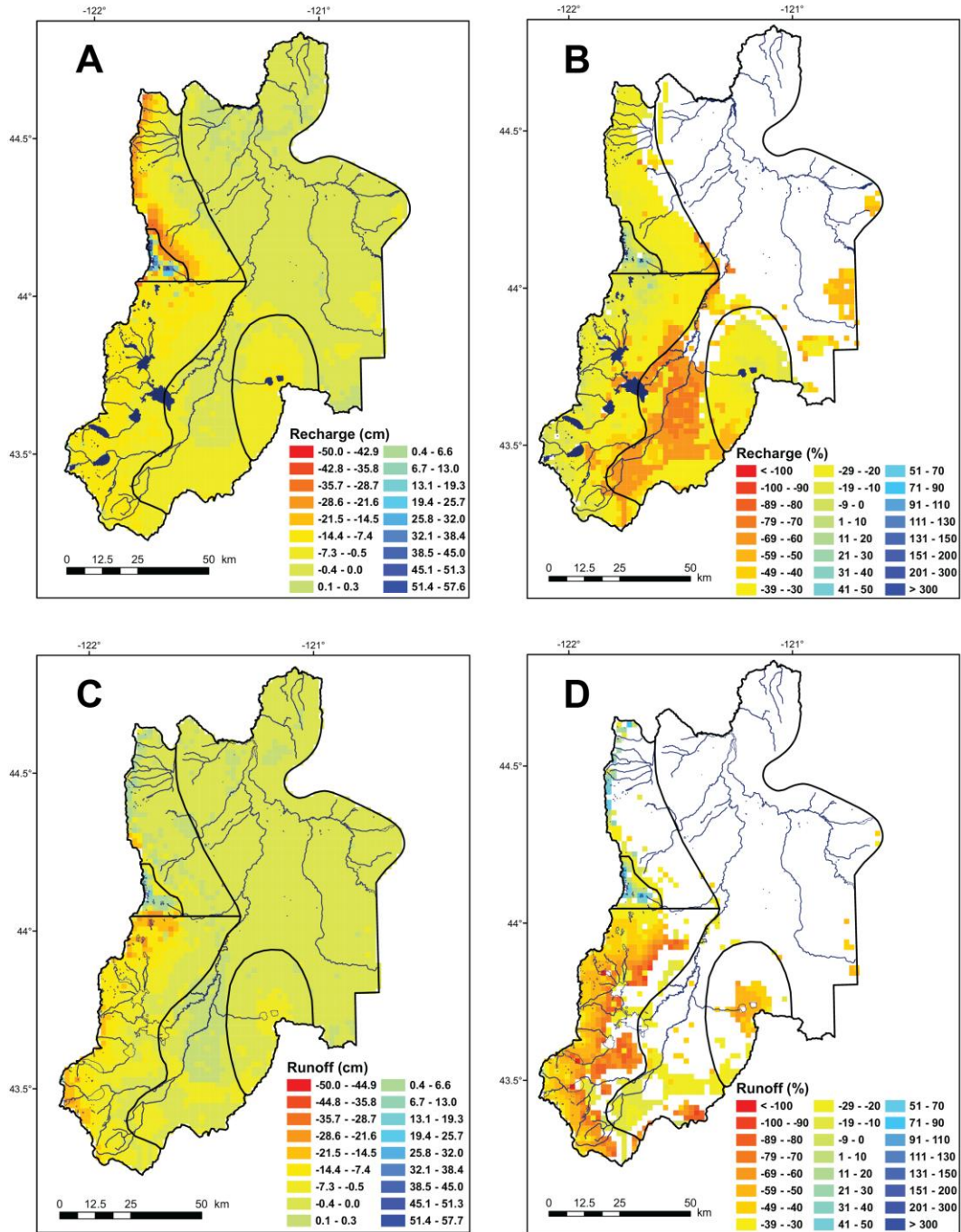
Appendix D.4. (A) Absolute change in spring recharge for the 2020s B1 period. (B) Percent changes in spring recharge for the 2020s B1 period. (C) Absolute change in spring runoff for the 2020s B1 period. (D) Percent changes in spring runoff for the 2020s B1 period.

APPENDIX E: 2050s Spatial Changes

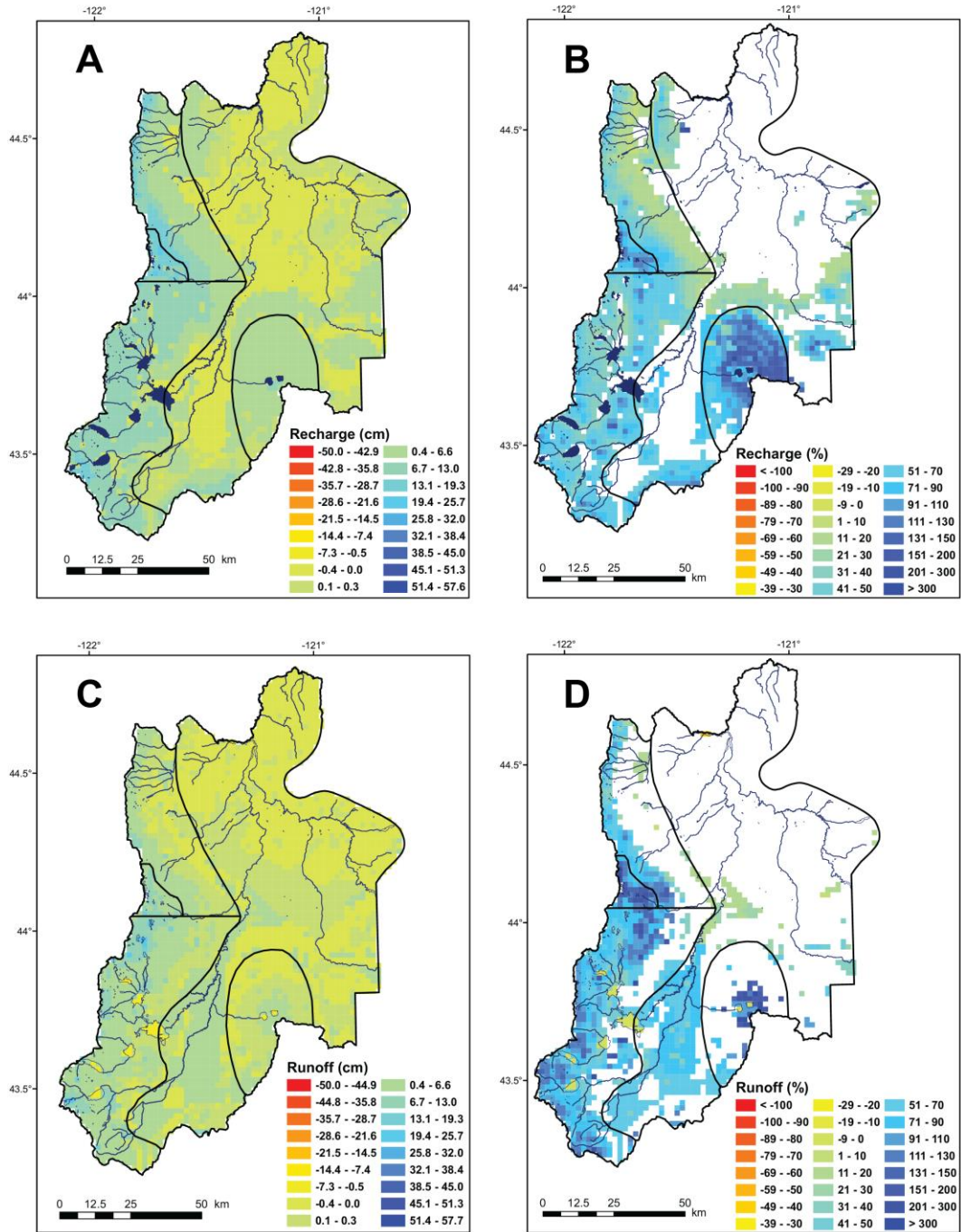
The following figures show the spatial changes from the 1980s base period winter and spring seasons as calculated by the DPM for the 2050s. The SRES A1B ensemble mean spatial changes for winter are shown followed by the corresponding A1B spring changes. B1 winter and spring changes are presented in the same manner. Note that recharge does not occur in open water cells in the southern portion of the basin and these cells are shaded in the darkest blue along with streams in the basin.



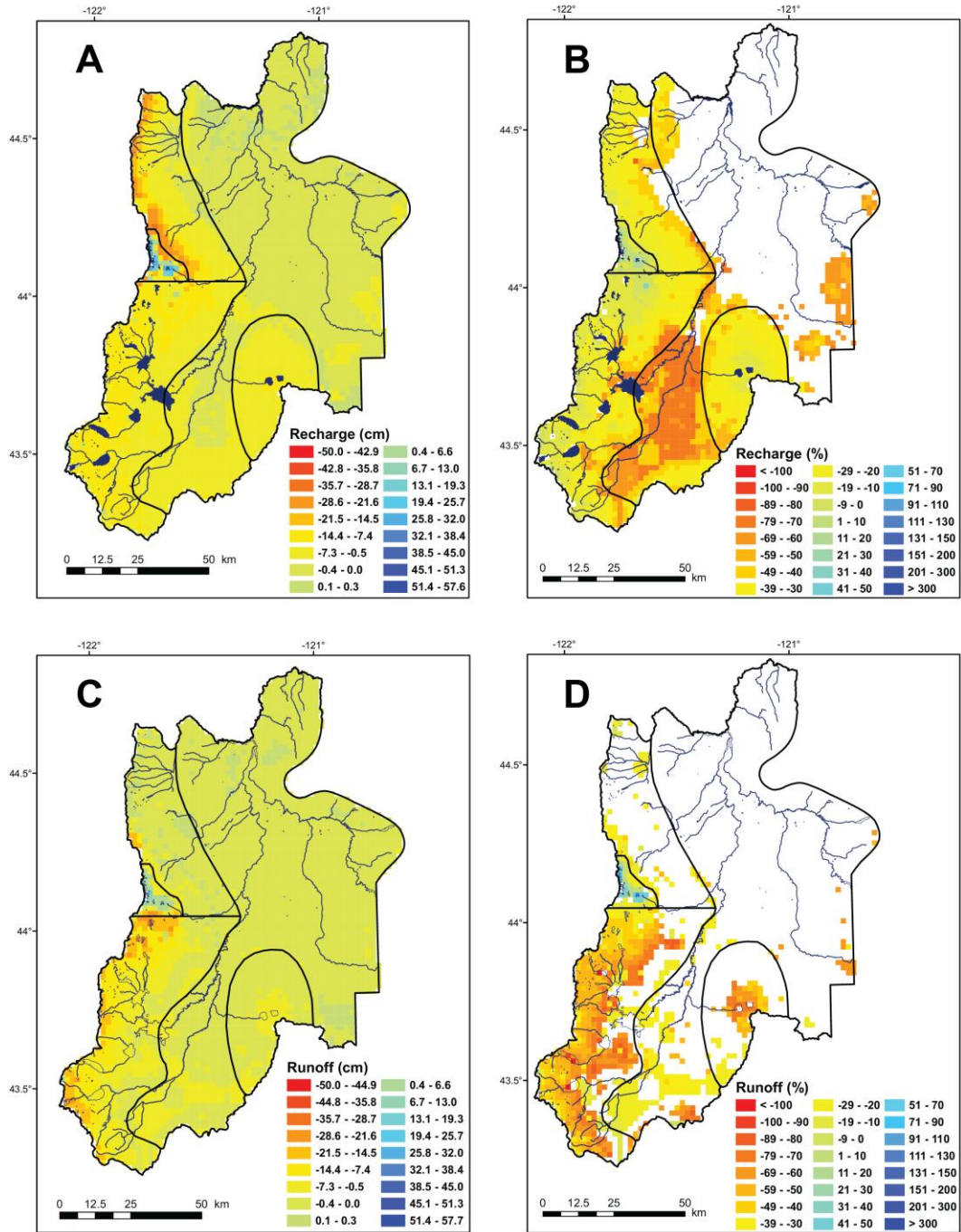
Appendix E.1. (A) Absolute change in winter recharge for the 2050s A1B period. (B) Percent change in winter recharge for the 2050s A1B period. (C) Absolute change in winter runoff for the 2050s A1B period. (D) Percent change in winter runoff for the 2050s A1B period.



Appendix E.2. (A) Absolute change in spring recharge for the 2050s A1B period. (B) Percent changes in spring recharge for the 2050s A1B period. (C) Absolute change in spring runoff for the 2050s A1B period. (D) Percent changes in spring runoff for the 2050s A1B period.



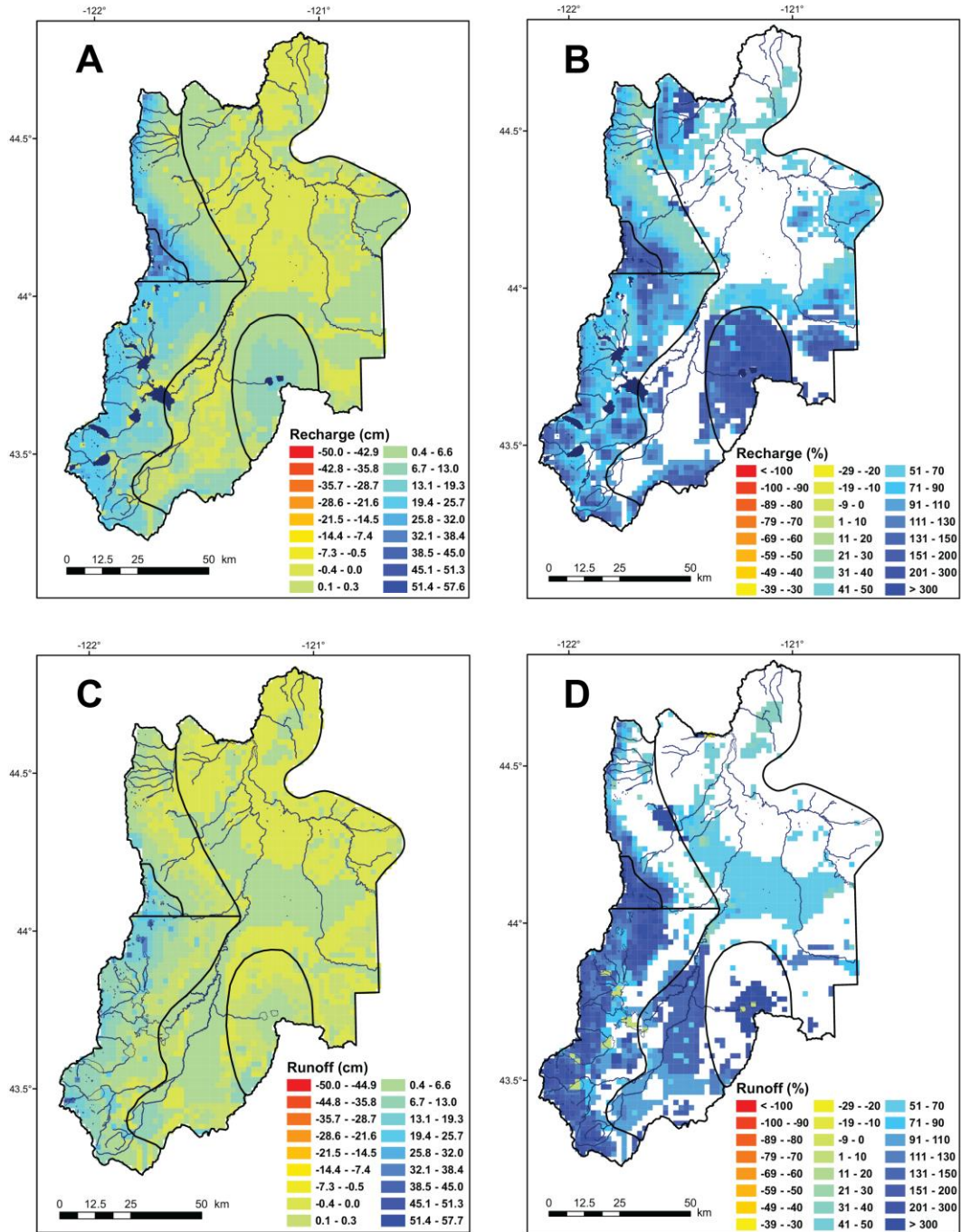
Appendix E.3. (A) Absolute change in winter recharge for the 2050s B1 period. (B) Percent change in winter recharge for the 2050s B1 period. (C) Absolute change in winter runoff for the 2050s B1 period. (D) Percent change in winter runoff for the 2050s B1 period.



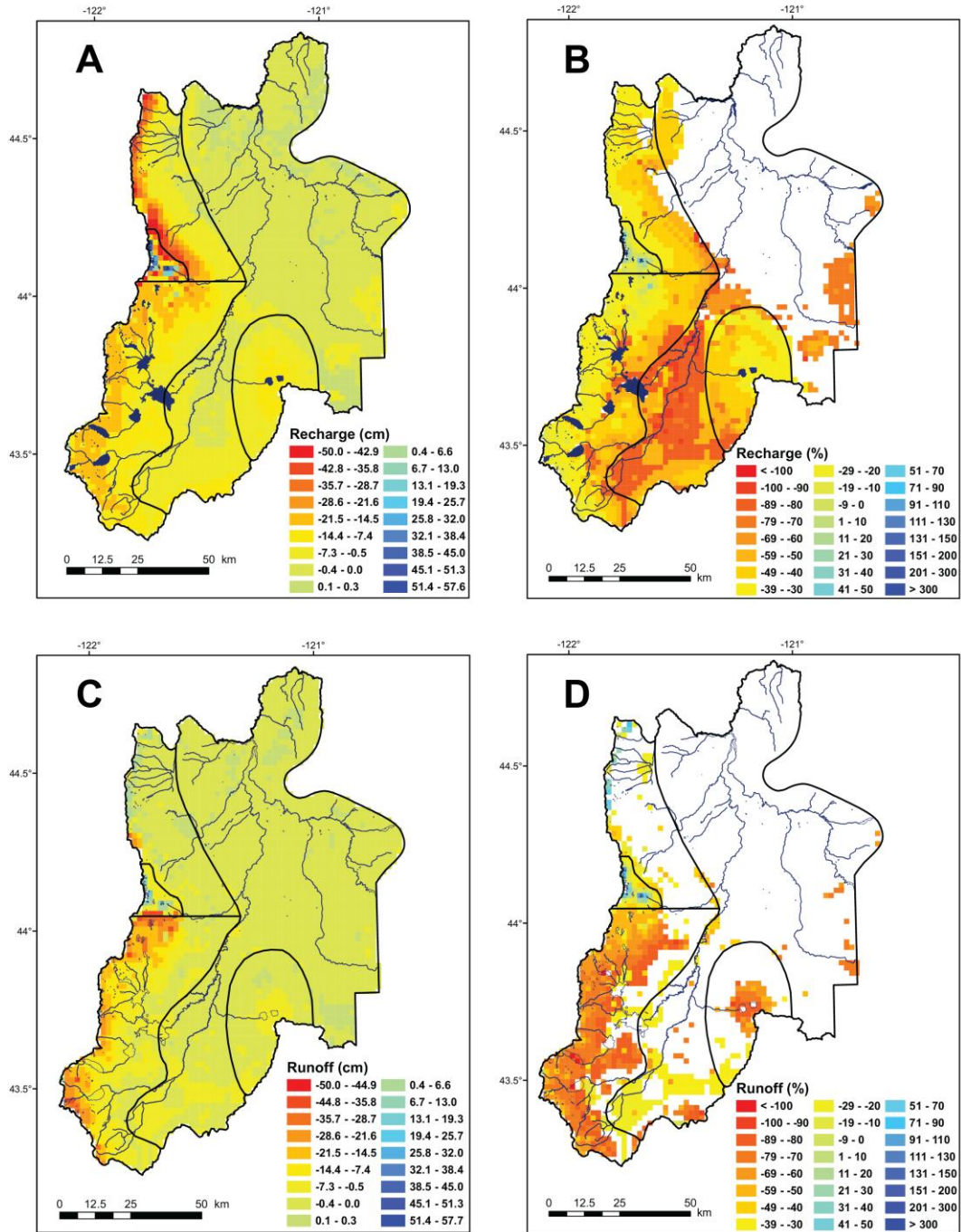
Appendix E.4. (A) Absolute change in spring recharge for the 2050s B1 period. (B) Percent changes in spring recharge for the 2050s B1 period. (C) Absolute change in spring runoff for the 2050s B1 period. (D) Percent changes in spring runoff for the 2050s B1 period

APPENDIX F: 2080s Spatial Changes

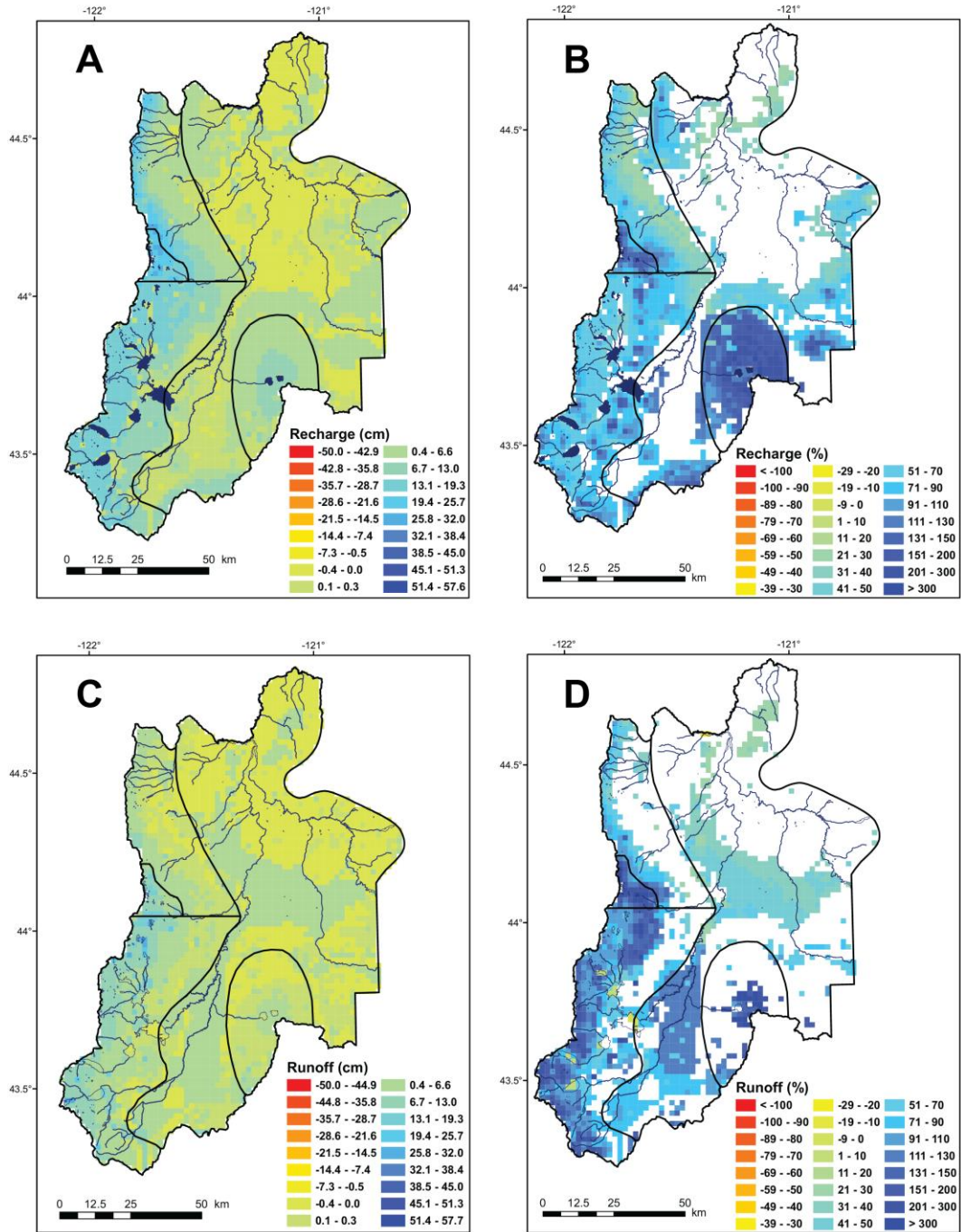
The following figures show the spatial changes from the 1980s base period winter and spring seasons as calculated by the DPM for the 2080s. The SRES A1B ensemble mean spatial changes for winter are shown followed by the corresponding A1B spring changes. B1 winter and spring changes are presented in the same manner. Note that recharge does not occur in open water cells in the southern portion of the basin and these cells are shaded in the darkest blue along with streams in the basin.



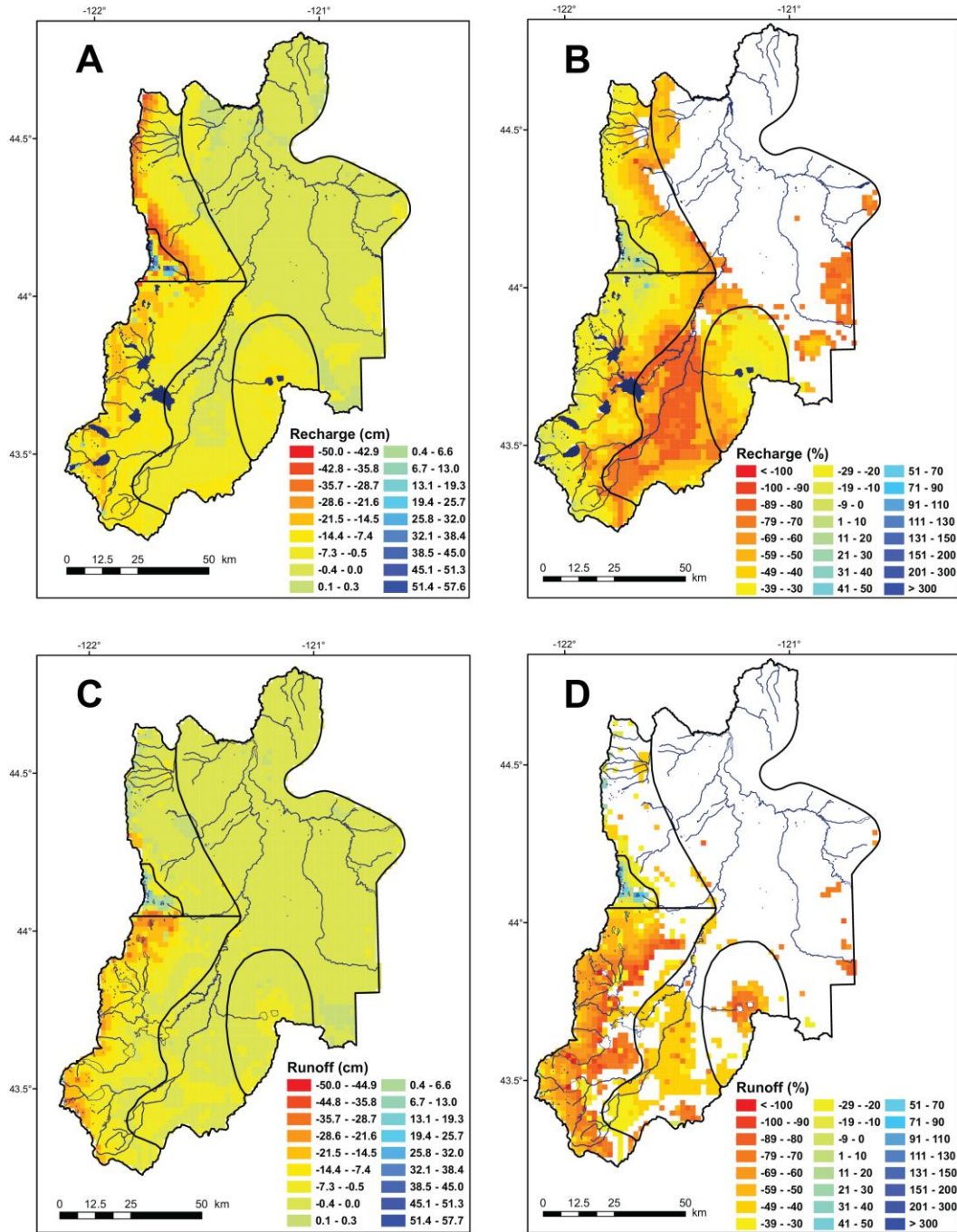
Appendix F.1. (A) Absolute change in winter recharge for the 2080s A1B period. (B) Percent change in winter recharge for the 2080s A1B period. (C) Absolute change in winter runoff for the 2080s A1B period. (D) Percent change in winter runoff for the 2080s A1B period.



Appendix F.2. (A) Absolute change in spring recharge for the 2080s A1B period. (B) Percent changes in spring recharge for the 2080s A1B period. (C) Absolute change in spring runoff for the 2080s A1B period. (D) Percent changes in spring runoff for the 2080s A1B period.



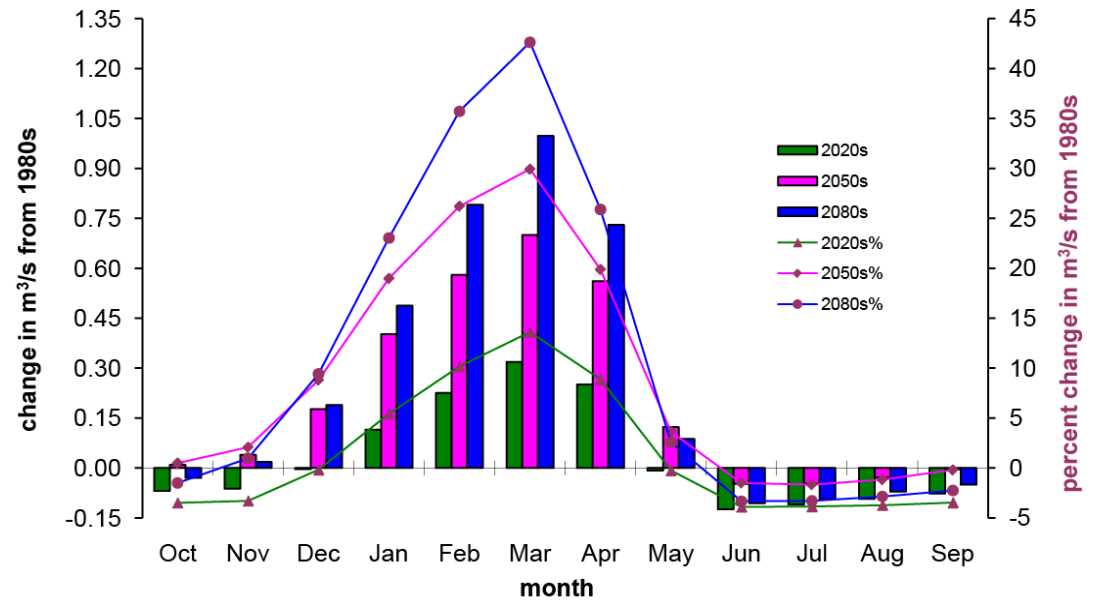
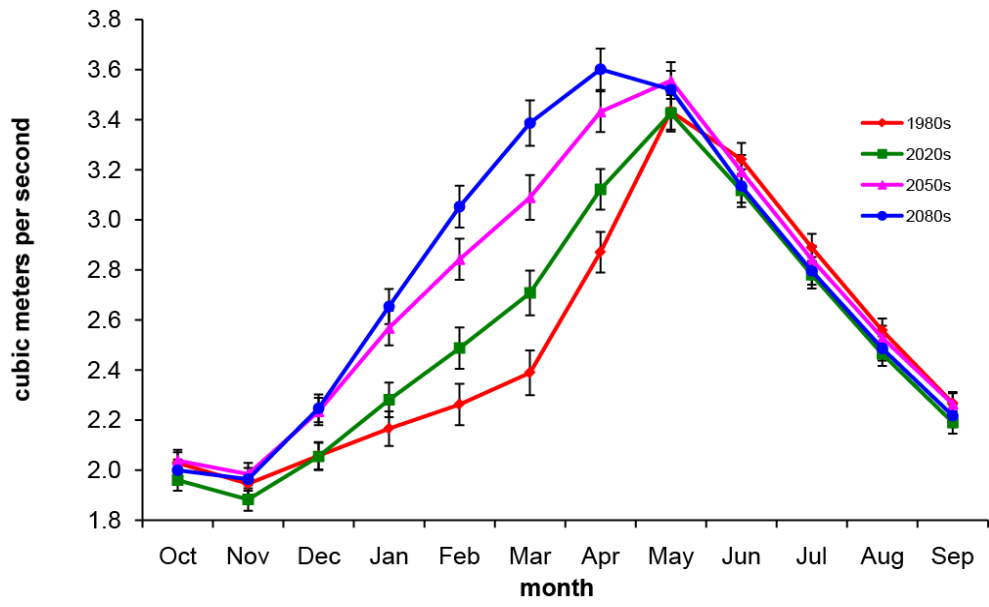
Appendix F.3. (A) Absolute change in winter recharge for the 2080s B1 period. (B) Percent change in winter recharge for the 2080s B1 period. (C) Absolute change in winter runoff for the 2080s B1 period. (D) Percent change in winter runoff for the 2080s B1 period.



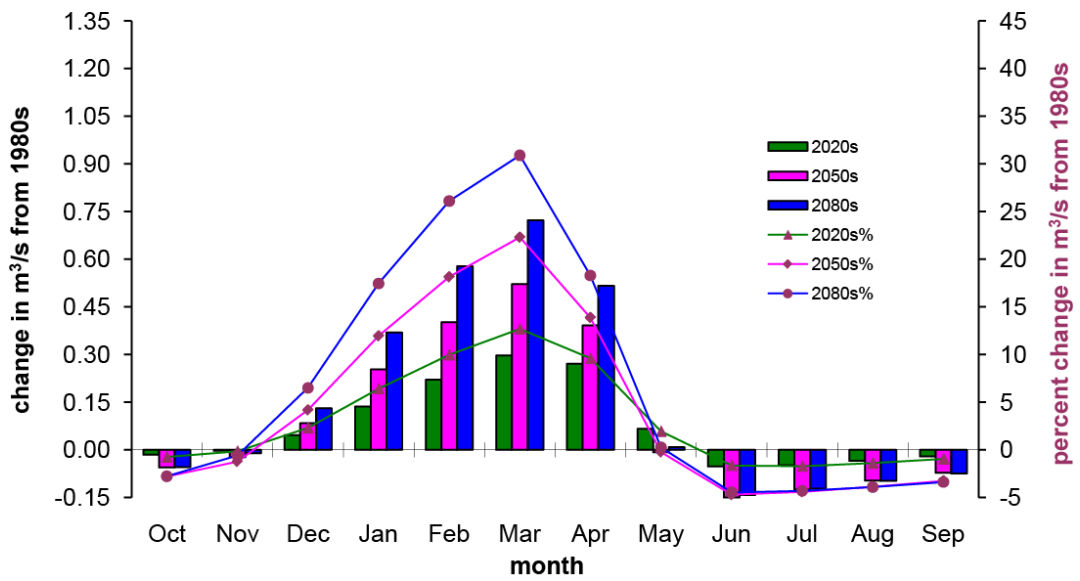
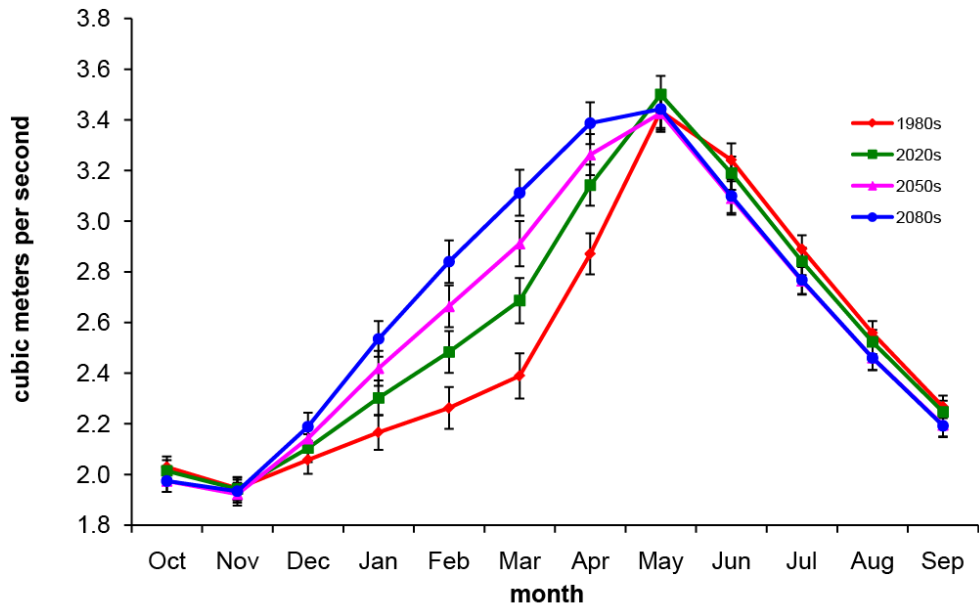
Appendix F.4. (A) Absolute change in spring recharge for the 2080s B1 period. (B) Percent changes in spring recharge for the 2080s B1 period. (C) Absolute change in spring runoff for the 2080s B1 period. (D) Percent changes in spring runoff for the 2080s B1 period.

APPENDIX G: Groundwater Discharge to Select Stream Reaches

The following figures and tables present the results of mean monthly groundwater discharge to select stream reaches in the upper Deschutes Basin. The final rows in tables are mean annual groundwater discharge for climate periods.



Appendix G.1. A1B emission scenario groundwater discharge to Big Marsh Creek.



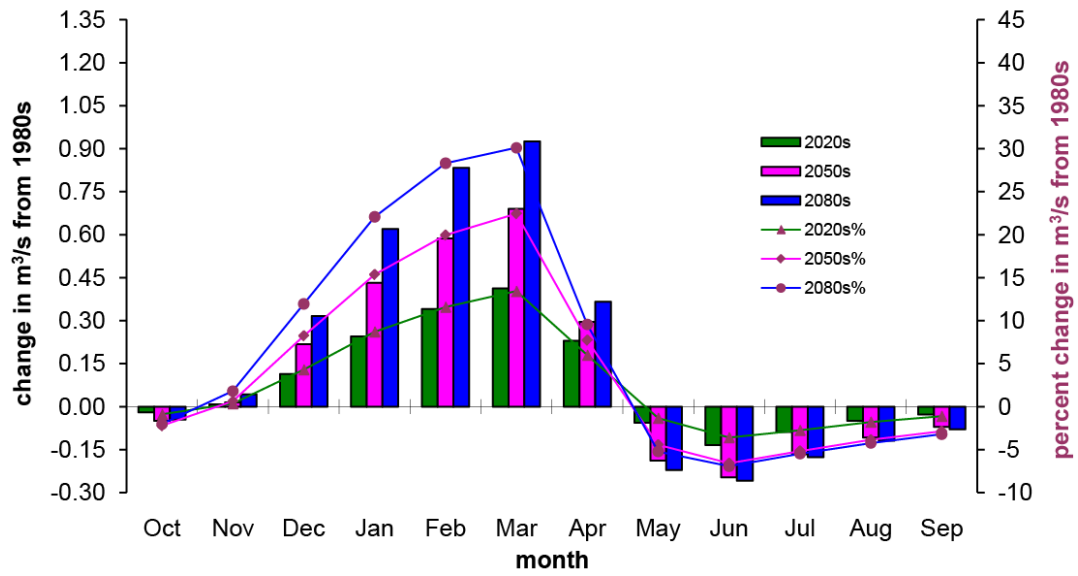
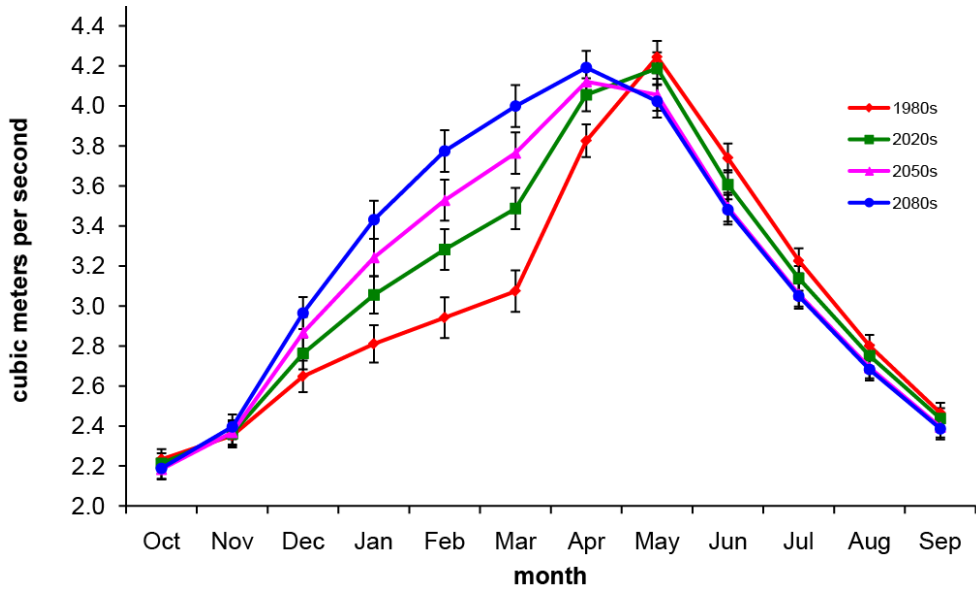
Appendix G.2. B1 emission scenario groundwater discharge to Big Marsh Creek.

Appendix G.3 A1B scenario groundwater discharge.

month	Big Marsh			
	1980s (m ³ /s)	2020s (m ³ /s)	2050s (m ³ /s)	2080s (m ³ /s)
Oct	1.979	1.910	1.989	1.950
Nov	1.895	1.833	1.935	1.914
Dec	2.008	2.005	2.185	2.197
Jan	2.116	2.231	2.518	2.604
Feb	2.213	2.438	2.793	3.003
Mar	2.340	2.658	3.040	3.337
Apr	2.821	3.072	3.382	3.552
May	3.384	3.376	3.507	3.471
Jun	3.192	3.067	3.144	3.086
Jul	2.840	2.731	2.793	2.747
Aug	2.508	2.415	2.479	2.437
Sep	2.217	2.141	2.213	2.168
mean	2.459	2.490	2.665	2.706

Appendix G.4. B1 scenario groundwater discharge.

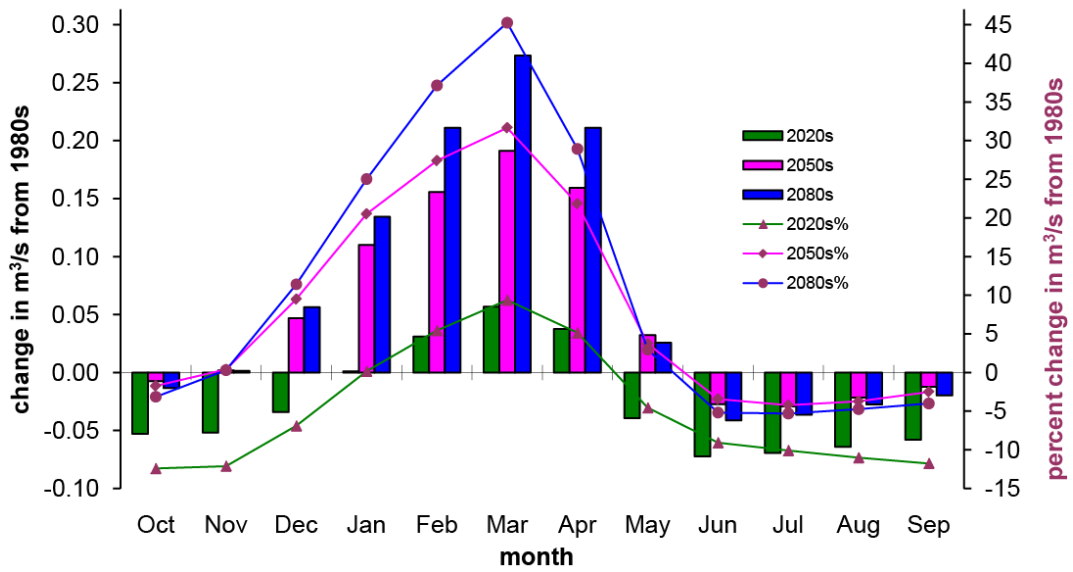
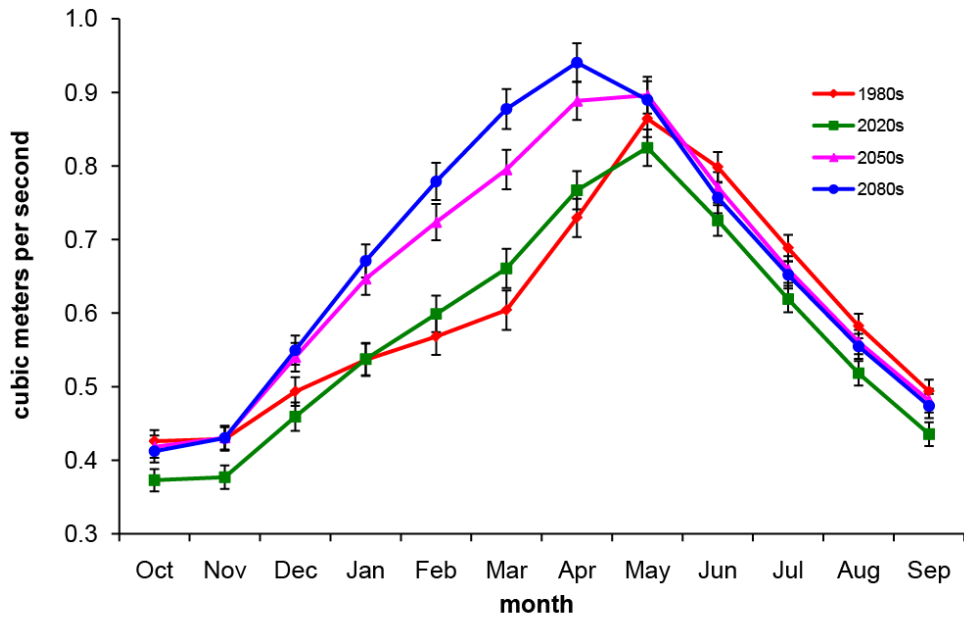
month	Big Marsh			
	1980s (m ³ /s)	2020s (m ³ /s)	2050s (m ³ /s)	2080s (m ³ /s)
Oct	1.979	1.964	1.924	1.925
Nov	1.895	1.893	1.872	1.884
Dec	2.008	2.054	2.092	2.139
Jan	2.116	2.252	2.369	2.486
Feb	2.213	2.434	2.614	2.791
Mar	2.340	2.637	2.862	3.062
Apr	2.821	3.092	3.213	3.338
May	3.384	3.450	3.377	3.393
Jun	3.192	3.140	3.042	3.050
Jul	2.840	2.792	2.715	2.718
Aug	2.508	2.474	2.411	2.410
Sep	2.217	2.197	2.146	2.143
mean	2.459	2.532	2.553	2.612



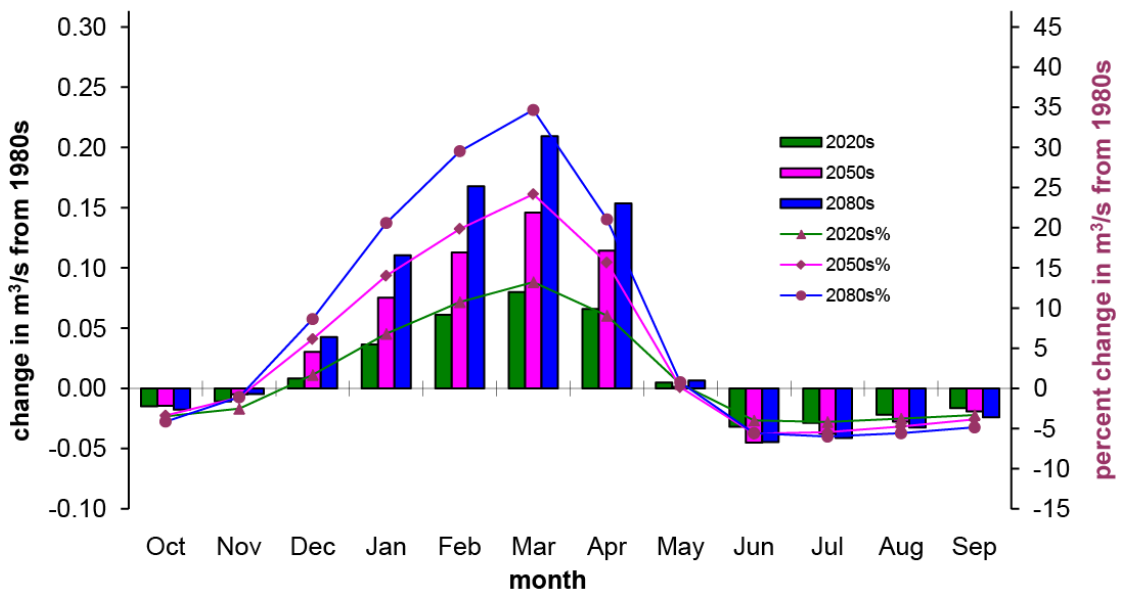
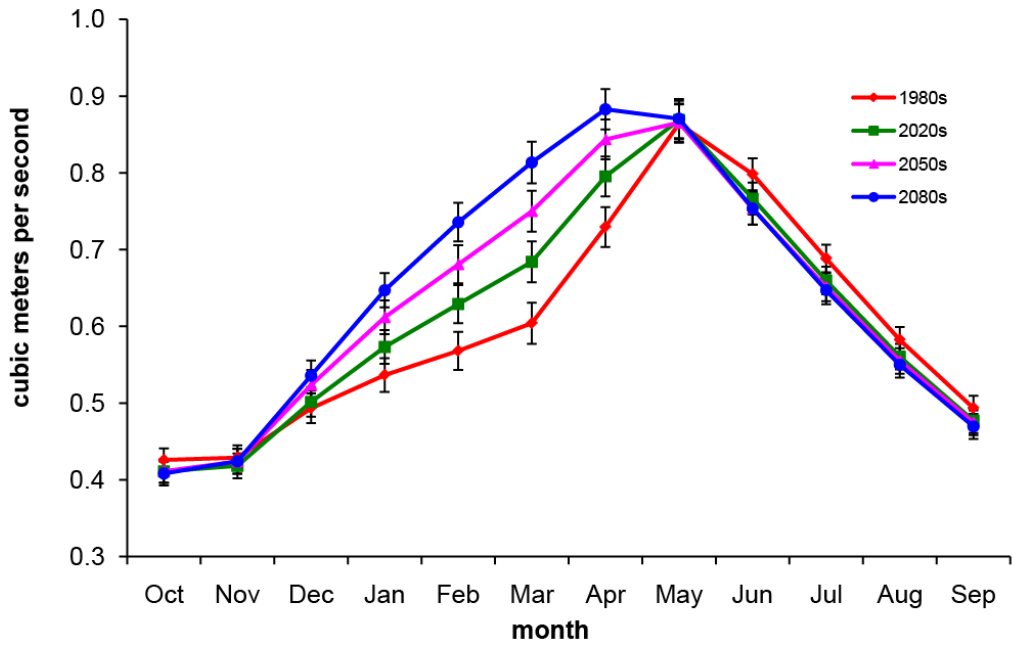
Appendix G.5. B1 emission scenario groundwater discharge to Odell Creek.

Appendix G.6. B1 scenario groundwater discharge.

month	Odell Creek			
	1980s (m ³ /s)	2020s (m ³ /s)	2050s (m ³ /s)	2080s (m ³ /s)
Oct	2.233	2.213	2.184	2.188
Nov	2.353	2.361	2.368	2.395
Dec	2.648	2.762	2.867	2.965
Jan	2.811	3.056	3.243	3.431
Feb	2.942	3.282	3.529	3.774
Mar	3.074	3.487	3.764	3.999
Apr	3.826	4.055	4.121	4.192
May	4.244	4.188	4.056	4.023
Jun	3.740	3.606	3.493	3.481
Jul	3.226	3.138	3.059	3.049
Aug	2.801	2.751	2.693	2.682
Sep	2.464	2.437	2.394	2.386
mean	3.030	3.111	3.148	3.214



Appendix G.7. A1B emission scenario groundwater discharge to Cultus Creek.



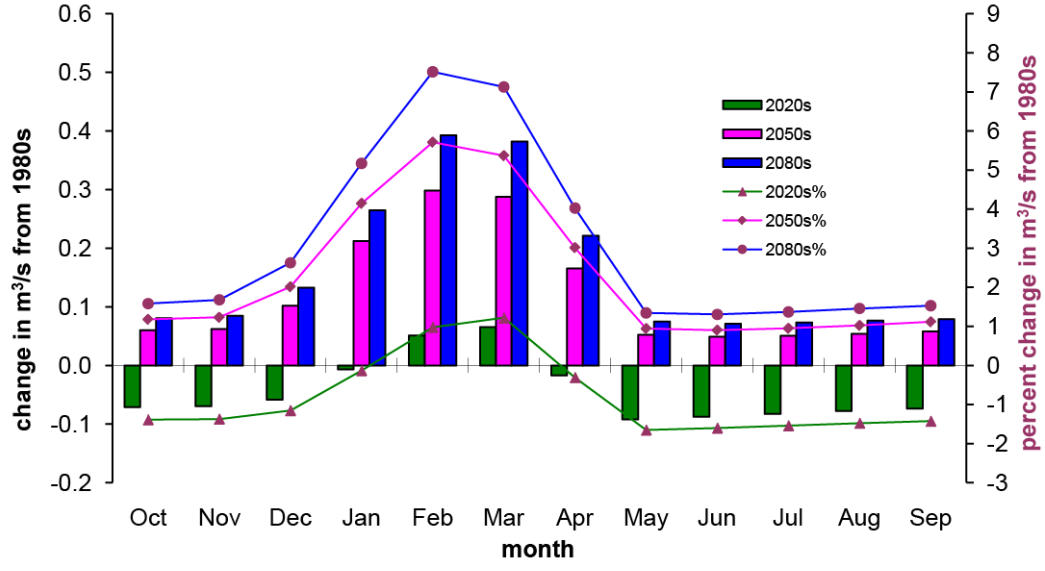
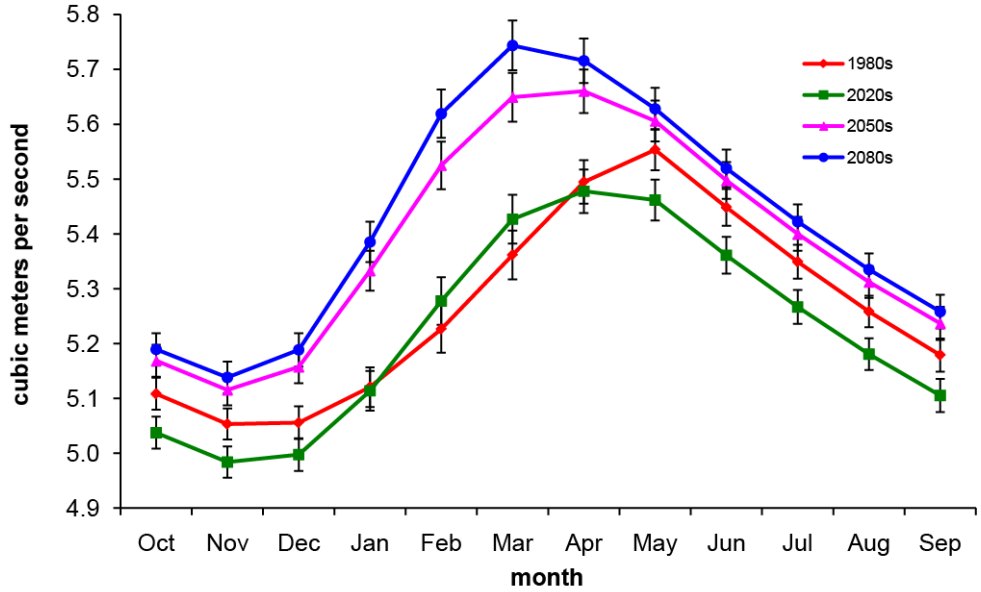
Appendix G.8. B1 emission scenario groundwater discharge to Cultus Creek.

Appendix G.9. A1B scenario groundwater discharge.

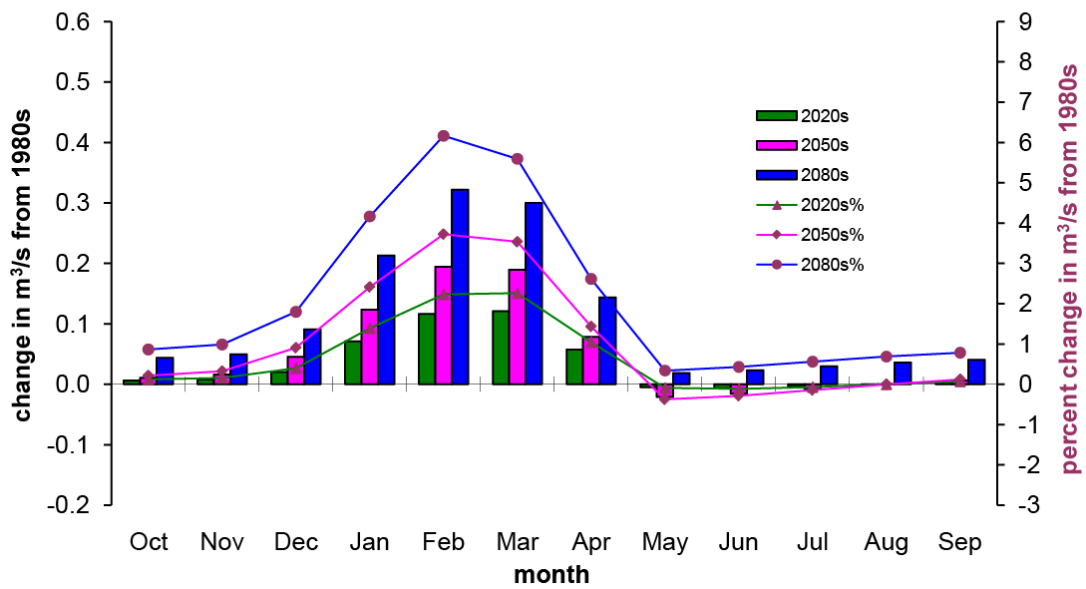
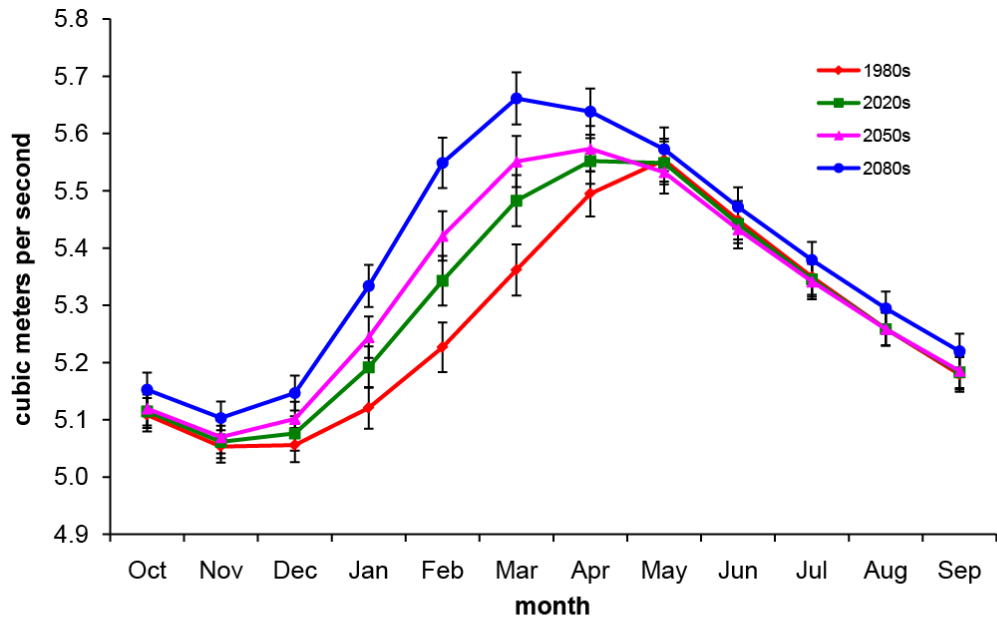
Cultus Creek				
	1980s	2020s	2050s	2080s
month	(m ³ /s)	(m ³ /s)	(m ³ /s)	(m ³ /s)
Oct	0.426	0.373	0.418	0.412
Nov	0.429	0.377	0.431	0.430
Dec	0.493	0.459	0.540	0.550
Jan	0.537	0.538	0.647	0.671
Feb	0.568	0.599	0.724	0.779
Mar	0.604	0.661	0.795	0.878
Apr	0.729	0.767	0.889	0.940
May	0.864	0.825	0.896	0.890
Jun	0.798	0.726	0.771	0.757
Jul	0.688	0.619	0.659	0.652
Aug	0.582	0.518	0.561	0.555
Sep	0.494	0.436	0.481	0.474
mean	0.601	0.575	0.651	0.666

Appendix G.10. B1 scenario groundwater discharge.

Cultus Creek				
	1980s	2020s	2050s	2080s
month	(m ³ /s)	(m ³ /s)	(m ³ /s)	(m ³ /s)
Oct	0.426	0.411	0.411	0.408
Nov	0.429	0.418	0.424	0.424
Dec	0.493	0.502	0.524	0.536
Jan	0.537	0.573	0.612	0.647
Feb	0.568	0.629	0.681	0.736
Mar	0.604	0.684	0.750	0.813
Apr	0.729	0.795	0.844	0.883
May	0.864	0.869	0.865	0.871
Jun	0.798	0.766	0.753	0.754
Jul	0.688	0.660	0.651	0.647
Aug	0.582	0.561	0.555	0.550
Sep	0.494	0.477	0.475	0.470
mean	0.601	0.612	0.629	0.645



Appendix G.11. A1B emission scenario groundwater discharge to Fall River.



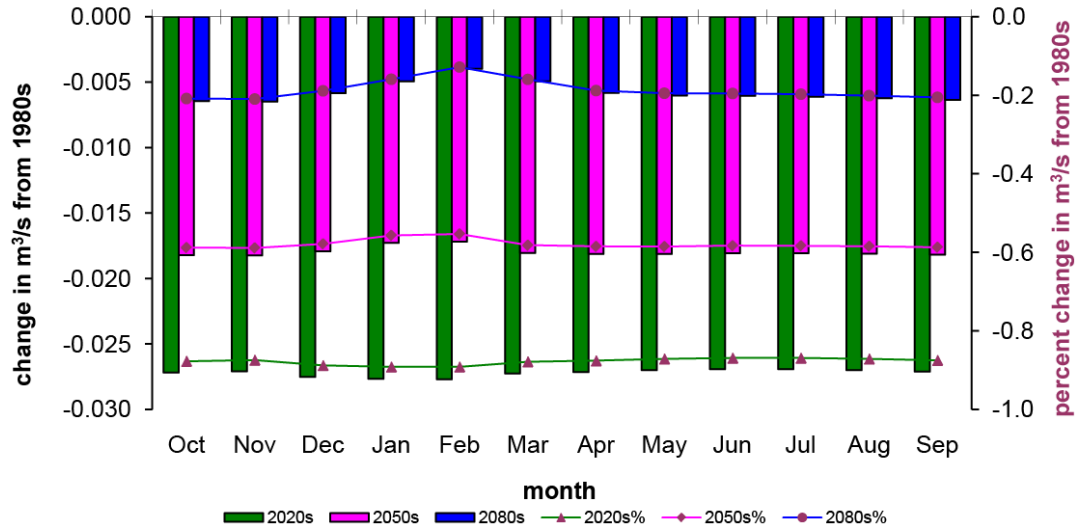
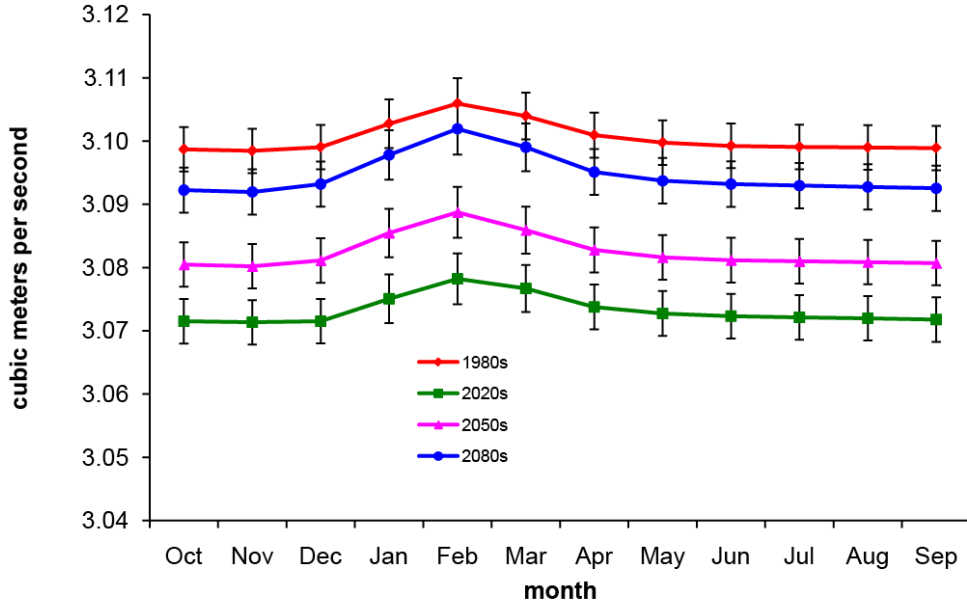
Appendix G.12. B1 emission scenario groundwater discharge to Fall River.

Appendix G.13. Fall River A1B scenario groundwater discharge.

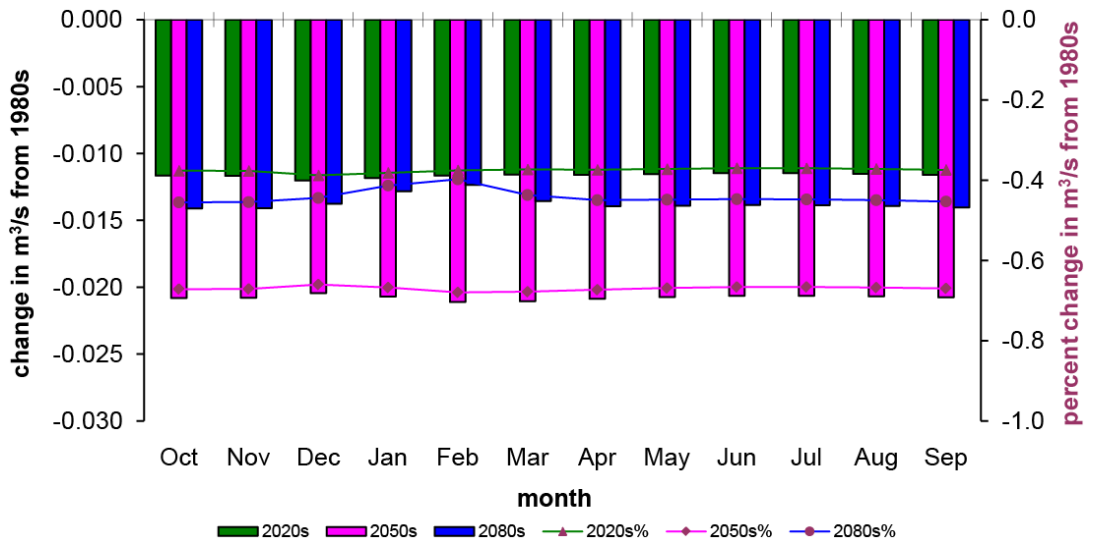
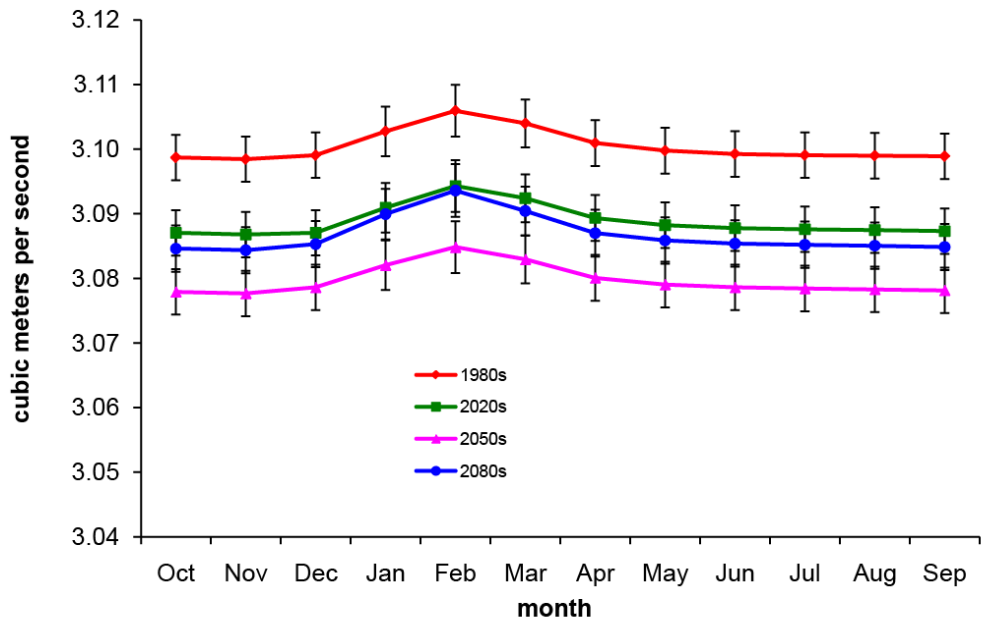
month	Fall River			
	1980s (m ³ /s)	2020s (m ³ /s)	2050s (m ³ /s)	2080s (m ³ /s)
Oct	5.108	5.037	5.169	5.189
Nov	5.053	4.984	5.115	5.138
Dec	5.056	4.997	5.157	5.188
Jan	5.121	5.114	5.333	5.385
Feb	5.226	5.278	5.525	5.619
Mar	5.362	5.427	5.649	5.744
Apr	5.495	5.478	5.660	5.716
May	5.553	5.462	5.606	5.628
Jun	5.448	5.361	5.498	5.520
Jul	5.349	5.267	5.400	5.422
Aug	5.258	5.181	5.312	5.335
Sep	5.179	5.105	5.237	5.258
mean	5.267	5.224	5.388	5.429

Appendix G.14. B1 scenario groundwater discharge.

month	Fall River			
	1980s (m ³ /s)	2020s (m ³ /s)	2050s (m ³ /s)	2080s (m ³ /s)
Oct	5.108	5.115	5.119	5.152
Nov	5.053	5.061	5.069	5.103
Dec	5.056	5.076	5.101	5.146
Jan	5.121	5.192	5.244	5.334
Feb	5.226	5.343	5.421	5.549
Mar	5.362	5.483	5.551	5.661
Apr	5.495	5.552	5.573	5.638
May	5.553	5.548	5.532	5.572
Jun	5.448	5.442	5.433	5.472
Jul	5.349	5.345	5.341	5.379
Aug	5.258	5.258	5.258	5.295
Sep	5.179	5.183	5.185	5.220
mean	5.267	5.300	5.319	5.377



Appendix G.15. A1B emission scenario groundwater inflow to lower Whychus Creek.



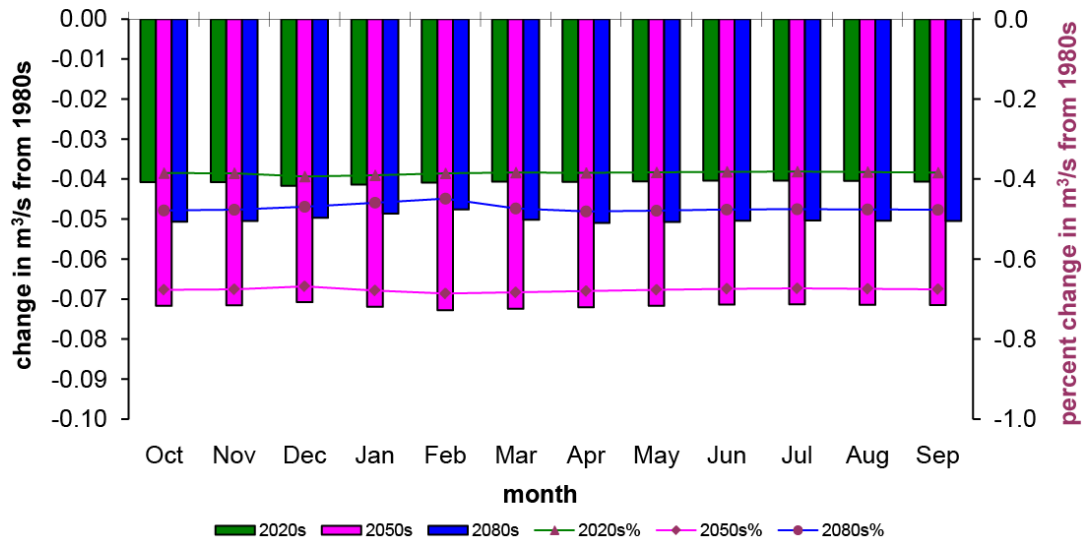
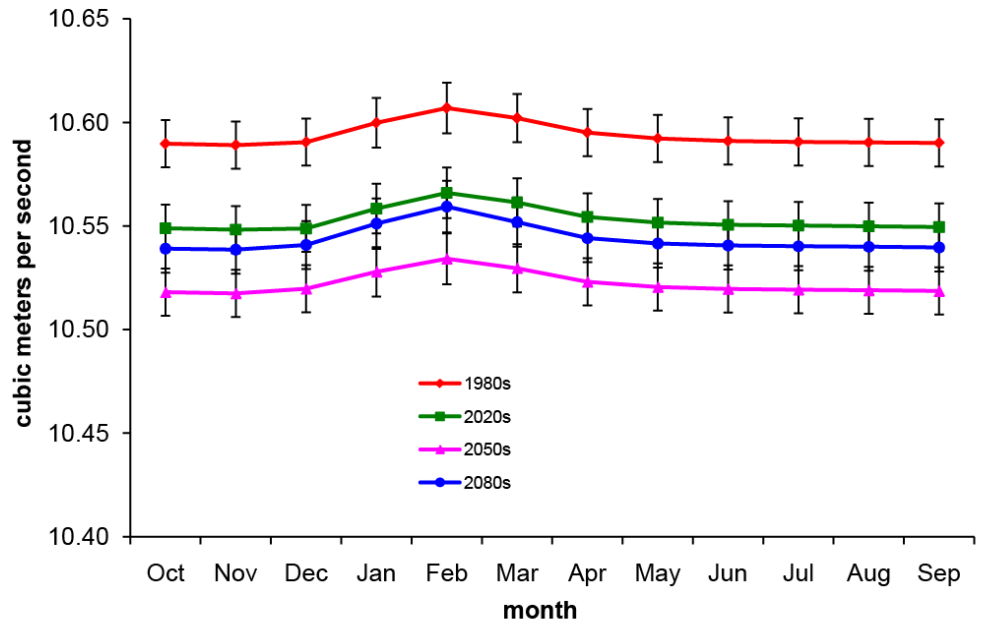
Appendix G.16. B1 emission scenario groundwater inflow to lower Whychus Creek.

Appendix G.17. A1B scenario groundwater discharge.

Inflow Lower Whychus				
month	1980s (m ³ /s)	2020s (m ³ /s)	2050s (m ³ /s)	2080s (m ³ /s)
Oct	3.099	3.072	3.080	3.092
Nov	3.098	3.071	3.080	3.092
Dec	3.099	3.072	3.081	3.093
Jan	3.103	3.075	3.085	3.098
Feb	3.106	3.078	3.089	3.102
Mar	3.104	3.077	3.086	3.099
Apr	3.101	3.074	3.083	3.095
May	3.100	3.073	3.082	3.094
Jun	3.099	3.072	3.081	3.093
Jul	3.099	3.072	3.081	3.093
Aug	3.099	3.072	3.081	3.093
Sep	3.099	3.072	3.081	3.093
mean	3.101	3.073	3.083	3.095

Appendix G.18. B1 scenario groundwater discharge.

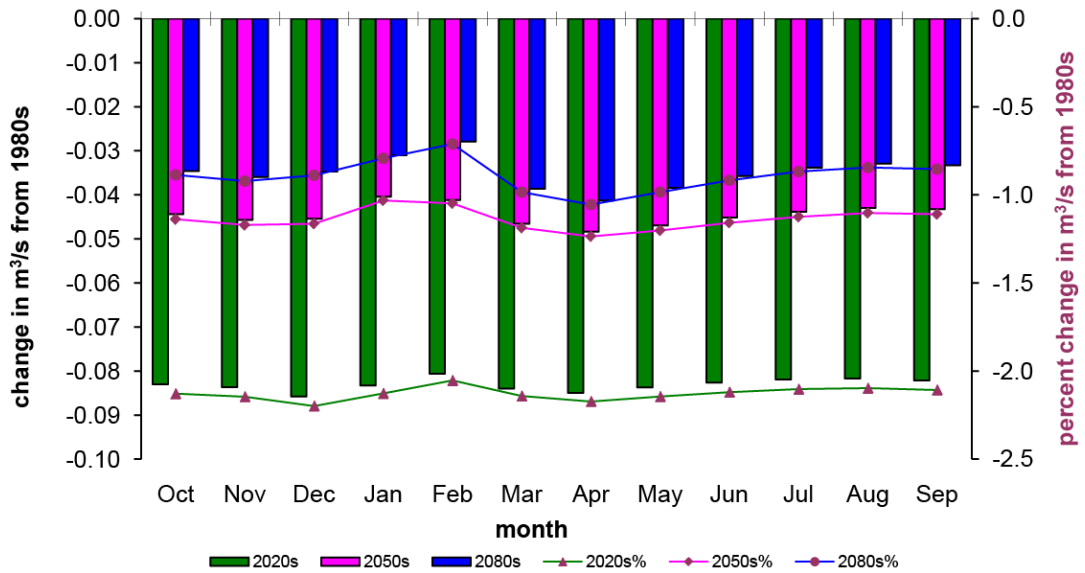
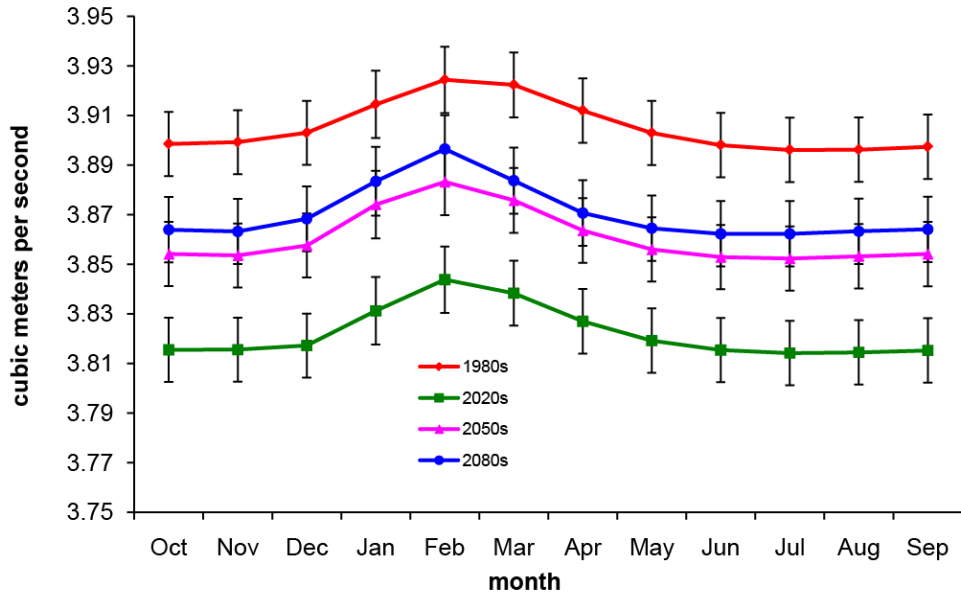
Inflow Lower Whychus				
month	1980s (m ³ /s)	2020s (m ³ /s)	2050s (m ³ /s)	2080s (m ³ /s)
Oct	3.099	3.087	3.078	3.085
Nov	3.098	3.087	3.078	3.084
Dec	3.099	3.087	3.079	3.085
Jan	3.103	3.091	3.082	3.090
Feb	3.106	3.094	3.085	3.094
Mar	3.104	3.092	3.083	3.090
Apr	3.101	3.089	3.080	3.087
May	3.100	3.088	3.079	3.086
Jun	3.099	3.088	3.079	3.085
Jul	3.099	3.088	3.078	3.085
Aug	3.099	3.087	3.078	3.085
Sep	3.099	3.087	3.078	3.085
mean	3.101	3.089	3.080	3.087



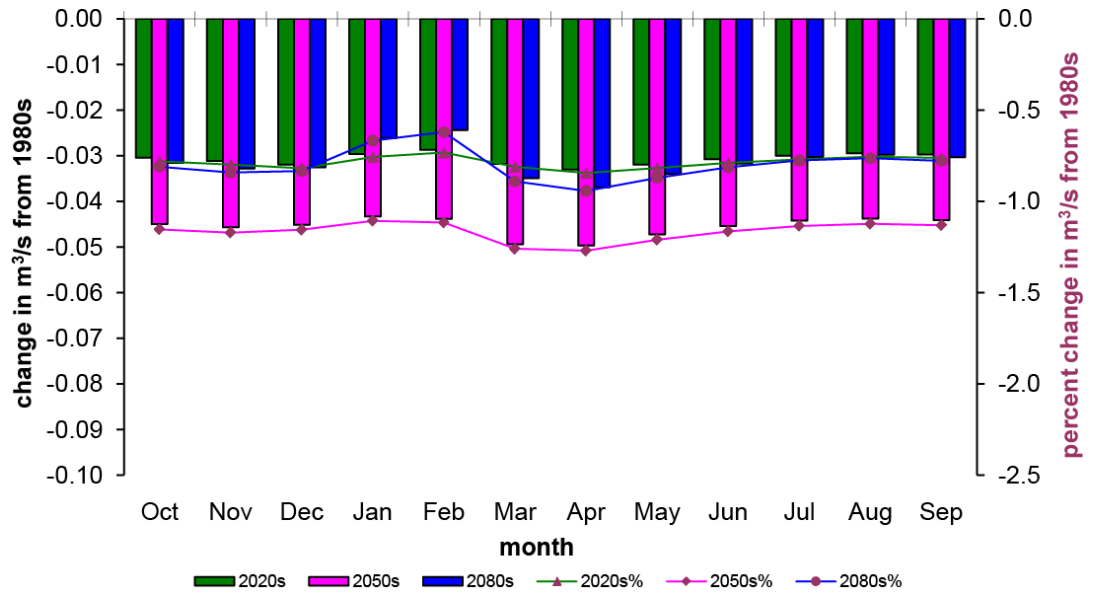
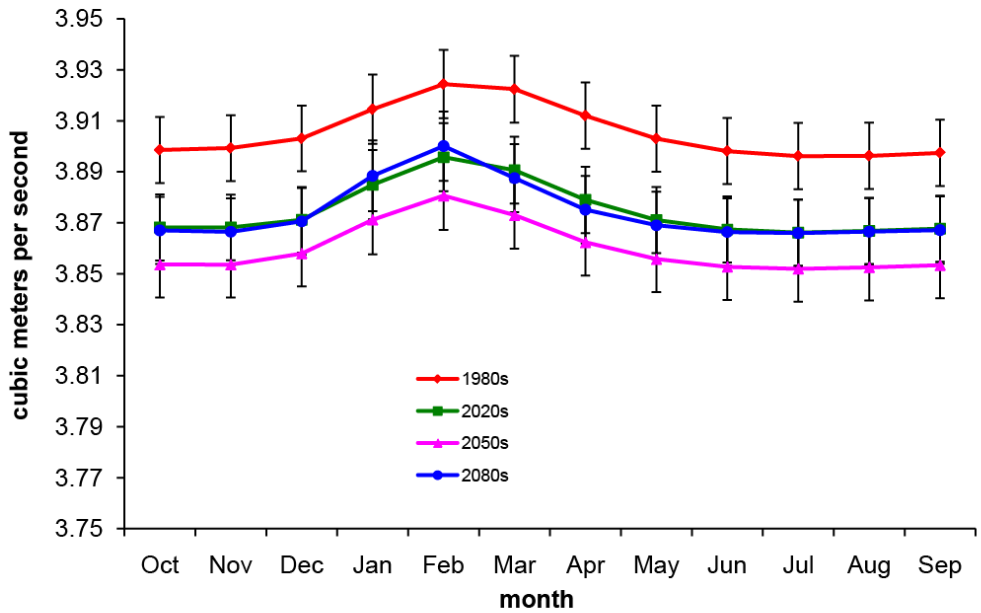
Appendix G.19. B1 emission scenario groundwater inflow to the Deschutes River between Lower Bridge and Culver.

Appendix G.20. B1 scenario groundwater discharge.

Inflow to Deschutes between Lower Bridge and Culver				
	1980s	2020s	2050s	2080s
month	(m ³ /s)	(m ³ /s)	(m ³ /s)	(m ³ /s)
Oct	10.590	10.549	10.518	10.539
Nov	10.589	10.548	10.517	10.539
Dec	10.590	10.549	10.520	10.541
Jan	10.600	10.558	10.528	10.551
Feb	10.607	10.566	10.534	10.559
Mar	10.602	10.561	10.530	10.552
Apr	10.595	10.554	10.523	10.544
May	10.592	10.552	10.521	10.542
Jun	10.591	10.551	10.520	10.541
Jul	10.591	10.550	10.519	10.540
Aug	10.590	10.550	10.519	10.540
Sep	10.590	10.549	10.519	10.540
mean	10.594	10.553	10.522	10.544



Appendix G.21. A1B emission scenario groundwater discharge from Metolius headwaters.



Appendix G.22. B1 emission scenario groundwater discharge from Metolius headwaters.

Appendix G.23. A1B scenario groundwater discharge.

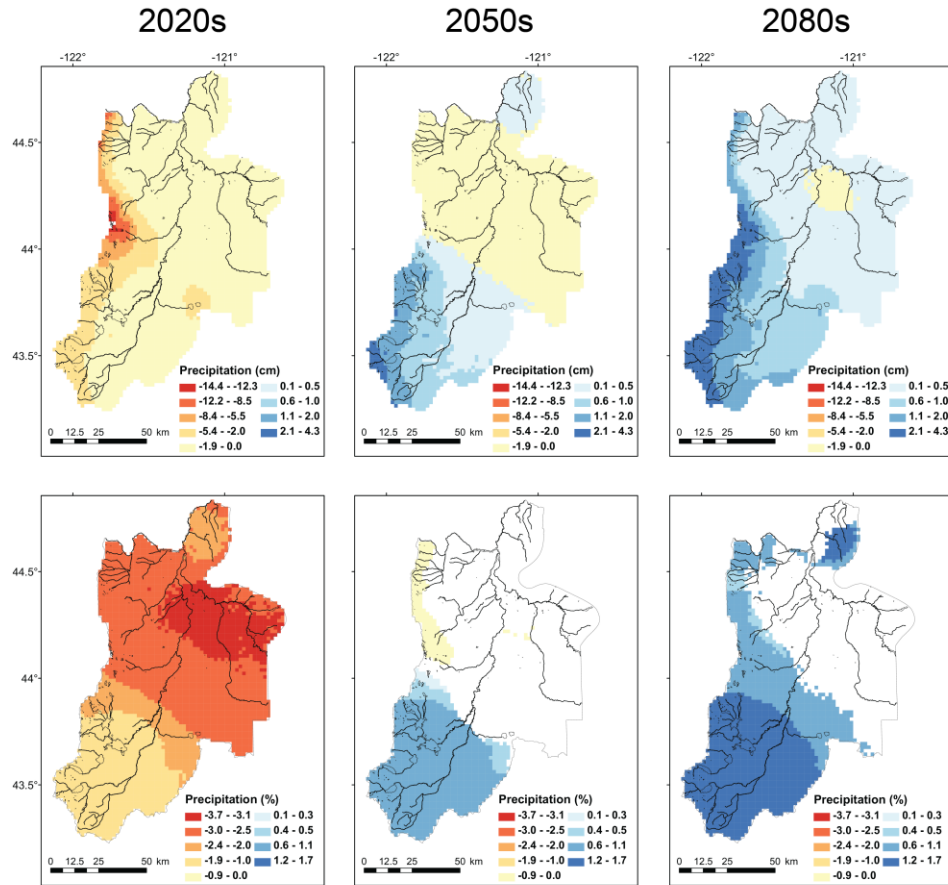
Metolius Headwaters				
month	1980s (m ³ /s)	2020s (m ³ /s)	2050s (m ³ /s)	2080s (m ³ /s)
Oct	3.899	3.816	3.854	3.864
Nov	3.899	3.816	3.854	3.863
Dec	3.903	3.817	3.858	3.868
Jan	3.915	3.831	3.874	3.883
Feb	3.924	3.844	3.883	3.897
Mar	3.922	3.838	3.876	3.884
Apr	3.912	3.827	3.864	3.871
May	3.903	3.819	3.856	3.865
Jun	3.898	3.815	3.853	3.862
Jul	3.896	3.814	3.852	3.862
Aug	3.896	3.815	3.853	3.863
Sep	3.897	3.815	3.854	3.864
mean	3.905	3.822	3.861	3.871

Appendix G.24. B1 scenario groundwater discharge.

Metolius Headwaters				
month	1980s (m ³ /s)	2020s (m ³ /s)	2050s (m ³ /s)	2080s (m ³ /s)
Oct	3.899	3.868	3.854	3.867
Nov	3.899	3.868	3.854	3.866
Dec	3.903	3.871	3.858	3.871
Jan	3.915	3.885	3.871	3.888
Feb	3.924	3.896	3.881	3.900
Mar	3.922	3.891	3.873	3.887
Apr	3.912	3.879	3.862	3.875
May	3.903	3.871	3.856	3.869
Jun	3.898	3.867	3.853	3.866
Jul	3.896	3.866	3.852	3.866
Aug	3.896	3.867	3.852	3.866
Sep	3.897	3.868	3.853	3.867
mean	3.905	3.875	3.860	3.874

APPENDIX H: Mean Annual Precipitation Changes

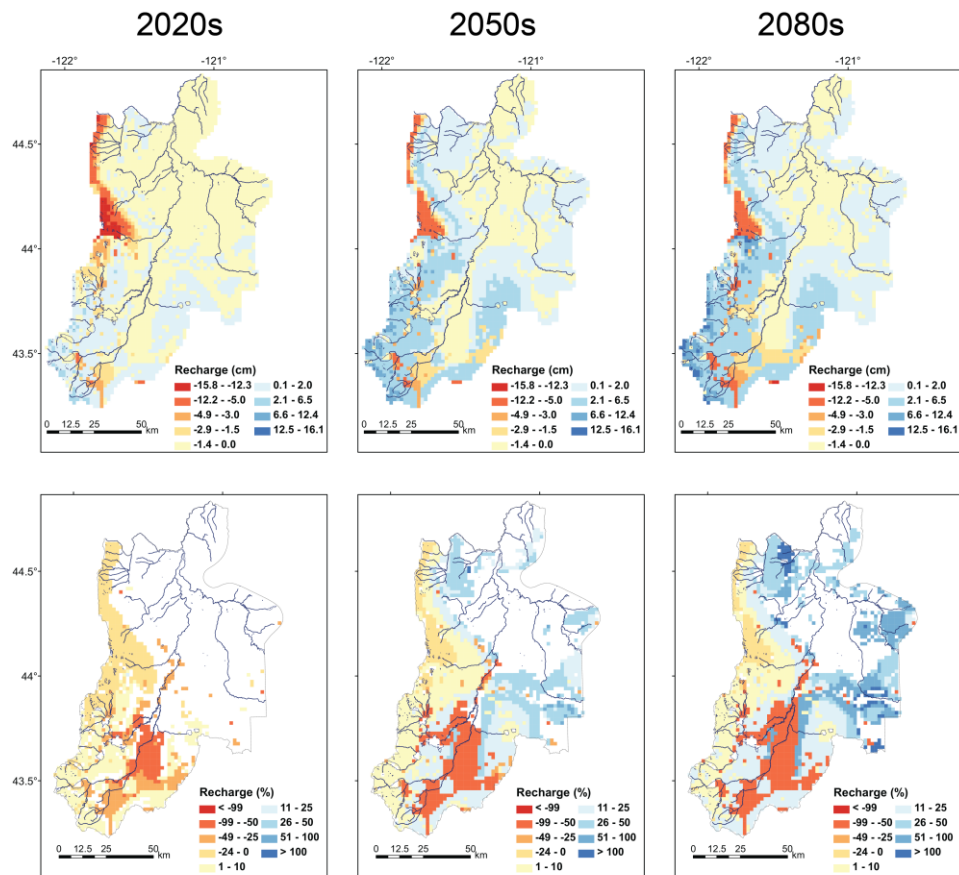
The following figure shows mean annual precipitation changes from the 1980s baseline period. Absolute change (Top) and percent change (Bottom) are presented for the A1B scenario. This spatial distribution is the dominant pattern for both emission scenarios, although magnitudes are generally less for the B1 scenario with the exception of the 2020s period changes. Increases appear in cool colors and decreases appear in warm colors.



Appendix H.1. Changes in mean annual precipitation for the A1B emission scenario.

APPENDIX I: Mean Annual Recharge Changes

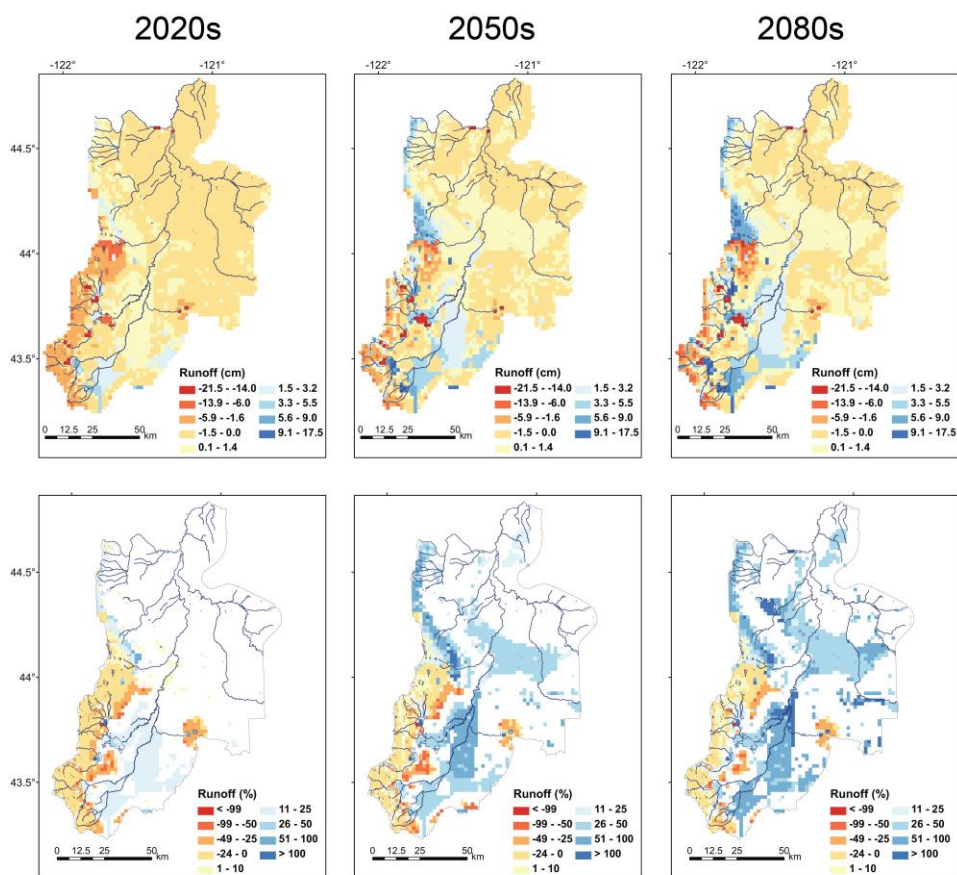
The following figure shows mean annual recharge changes from the 1980s baseline period. Absolute change (Top) and percent change (Bottom) are presented for the A1B scenario. This spatial distribution is the dominant pattern for both emission scenarios, although magnitudes are generally less for the B1. Increases appear in cool colors and decreases appear in warm colors.



Appendix I.1. Changes in mean annual recharge for the A1B emission scenario.

APPENDIX J: Mean Annual Runoff Changes

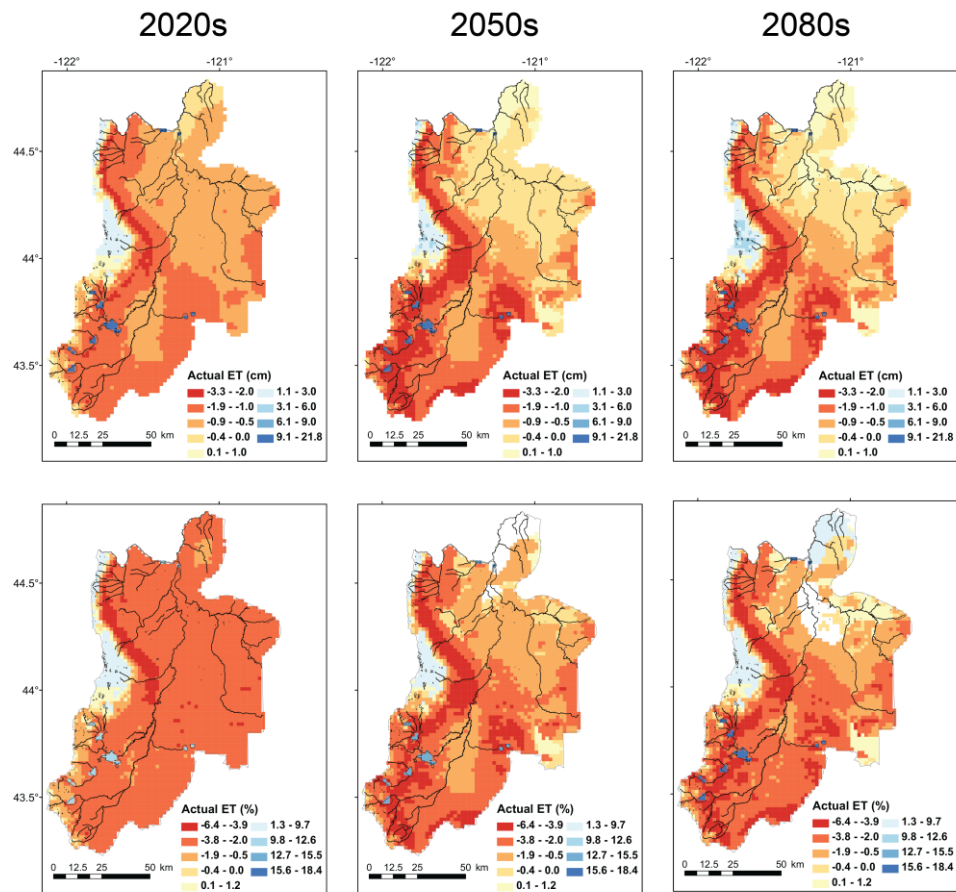
The following figure shows mean annual runoff changes from the 1980s baseline period. Absolute change (Top) and percent change (Bottom) are presented for the A1B scenario. This spatial distribution is the dominant pattern for both emission scenarios, although magnitudes are generally less for the B1. Increases appear in cool colors and decreases appear in warm colors.



Appendix J.1. Changes in mean annual runoff for the A1B emission scenario

APPENDIX K: Mean Annual Actual Evapotranspiration Changes

The following figure shows mean annual actual evapotranspiration changes from the 1980s baseline period. Absolute change (Top) and percent change (Bottom) are presented for the A1B scenario. This spatial distribution is the dominant pattern for both emission scenarios, although magnitudes are generally less for the B1. Increases appear in cool colors and decreases appear in warm colors.



Appendix K.1. Changes in mean annual actual evapotranspiration for the A1B emission scenario.